Ultrasound Data Communications for Ultra-low-power Wake-up in Sensor Nodes

Kshitij Yadav

Submitted in partial fulfillment of the
requirements for the degree of
Doctor of Philosophy
in the Graduate School of Arts and Sciences

COLUMBIA UNIVERSITY

2012

Abstract

Ultrasound Data Communications for Ultra-low-power Wake-up in Sensor Nodes

Kshitij Yadav

In the power-starved wireless sensor node application, the main transceiver has to be duty-cycled to prolong the node battery lifetime. Wake-up is among the lowest power schemes to accomplish this; an always ON low-power receiver called the wake-up receiver is used to turn ON the main receiver when needed. In this thesis, we have demonstrated ultra-low-power wake-up by using through-air wireless ultrasound. We have achieved more than an order of magnitude reduction in wake-up receiver power consumption, compared to conventionally used radio frequencies.

An ultra-low-power ultrasonic wake-up receiver IC was designed in a 65-nm CMOS process and has a power consumption of only 4.4 μW. For the proof-of-concept prototype demonstrated in this work, the digital back-end circuits were been implemented on a commercial FPGA. An ultrasound data network consisting of three receivers and one transmitter was set up in a lecture hall. For a transmit power of 27 μW, less than 10 $\%$ of the wake-up packets, at 1 pkt/s, were missed at each of the three receivers. All the system blocks: receiver IC, ultrasound communication channel and TX-RX transducer pair, were individually characterized in different environments to understand the interaction between

the electrical and mechanical domains. Also presented are techniques for increasing the distance ranges of wireless ultrasound and communication schemes for extending the use of ultrasound to environments where line-of-sight communication is not possible.

Contents

List of Figures

This page intentionally left blank.

List of Tables

This page intentionally left blank.

Acknowledgments

This is the part of the thesis that gives me the opportunity to share the experiences of doing a PhD and thank the people involved in the process. Saying it was an enriching experience will be an understatement; it was an all round experience that taught lessons beyond the technical stuff. I never foresaw, during my starting days, that my approach towards work execution and my way of looking at things will undergo such a change at the end of these five years.

I would like to thank Prof. Kinget; his emphasis on work ethic, discipline, attention-to-detail and time management are inspiring. During the course of my PhD, I found him very receptive and patient with the opposing point of views that I sometimes presented. And above all, his ability to focus on the object of the analysis, while filtering out the unimportant, is a quality that I am still trying to emulate. I will include one of his work-execution related quotes here:

This is true for life also, but for now I will keep it to circuits – sometimes you have to adopt an iterative approach.

I will like to thank Prof. Kymissis for his extremely open, creative and fresh approach to things. Being from a different field than the IC design, he often helped me understand how the same work may be perceived by people from different backgrounds. In today's time, with more and more emphasis on multidisciplinary research and with boundaries between

different areas fast disappearing, I think being able to bridge different areas is an essential skill. I will include one of his approach related quotations:

If you do anything that is worth doing, half of the people are not going to agree with you; but what matters is the other half.

Going forward, as I collaborate on with Prof. Kinget and Prof. Kymissis, I keenly look forward to their feedbacks and, more importantly, to their criticisms.

I will also like to mention my CISL colleagues. In no particular order, they are Chun-wei Hsu, Sharvil Patil, Jayanth Kuppambatti, Baradwaj Vigraham, Jianxun Zhu, Karthik Jayaraman and Chengrui Le. I also learned a great deal from my interaction with my friends outside the lab. Varun Kumar, whom I have known since my days at IIT, has often provided me with very different perspectives, than my own, to both work and non-work related situations; this has added more dimensions to the way I perceive things. Rituraj Misra, another friend from my undergraduate days, with his broad knowledge of topics from history to philosophy, has helped me grow as an individual.

I also had the opportunity to mentor some M.S. students and one B.S. student. In no particular order, they are Zuyang Cao, Jihong Zou, David Blumenfeld, Lida Lu, Yueqian Huang and Frank Fang. Out of all the phases of my PhD, mentoring was the part that taught me the most about myself.

Last, but my no means least, I am grateful to my parents and my sister. During the course of the PhD, my parents seldom asked how much time it will take and have thor-

oughly supported what I plan to do next. They have always been a great source of wisdom, while letting me exercise my choices with complete freedom.

Chapter 1

Introduction

The idea of ubiquitous embedded wireless sensor networks (WSNs) for environmental, industrial and structural monitoring has been envisioned for a long time. Progress has been made with advances in technology, but the realization of small autonomous nodes with long lifetimes remains an open challenge. A ubiquitous sensor network consists of thousands of distributed nodes (Fig. 1.1(a)) which makes battery replacement both difficult and costly. This imposes very stringent constraints on the power budget of the accompanying hardware and a key technological issue in making wireless sensor nodes widespread, has been the realization of node electronics with extremely low power consumption.

Out of the three node functions (sensing, communication and computation), most of the node power is expended in communication. According to some estimates [1], communication circuitry consumes an overwhelming 99.9% of the node power. However, the activity of sensor nodes is low, which is exploited to save power by turning OFF the transceiver for

large percentages of time. The power consumption in the monitoring state then dominates the overall node power. In [2], experiments are performed on sensor networks that are used for environmental monitoring and it is concluded that more than 80% of the radio power is wasted in idle listening (Fig. 1.1(b)).

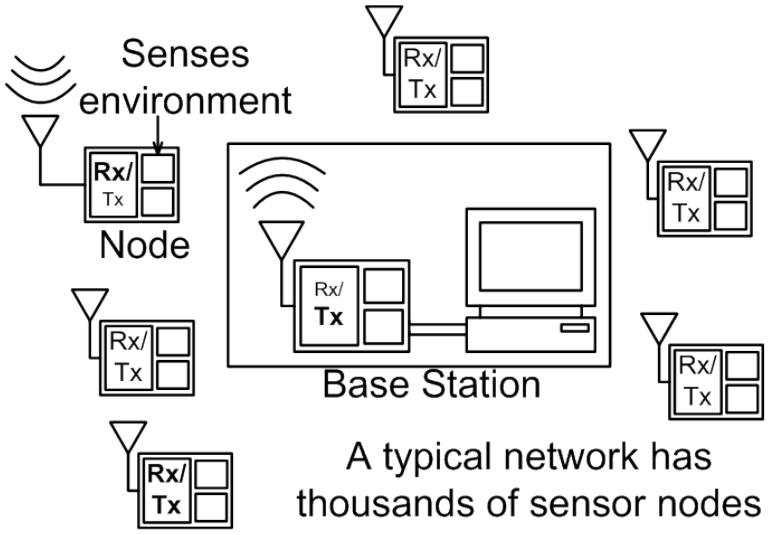

(a)

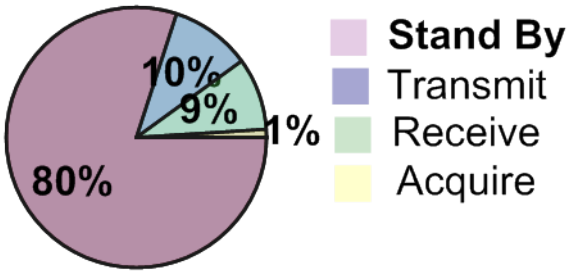

(b)

Figure 1.1: (a) A typical wireless sensor environment has thousands of nodes, making battery replacements costly and difficult. (b) An estimated 80% of the battery drains while the node is in stand-by.

1.1 Receiver Duty-cycling in Wireless Sensor Networks

To reduce the node power consumption during idle listening, different ways to duty-cycle the transceiver have been proposed, which can be put into three broad categories, synchronous, asynchronous and pseudo-synchronous. In the synchronous approach, a global clock is used to schedule events within the network. However, the power consumption in maintaining and distributing a clock at each node is usually large. Thus, sometimes a pseudo-synchronous approach is used, in which the communication can be initiated either by the receiver or the transmitter (Fig. 1.2(a)). When the communication is transmitter (receiver) initiated, the initiating node sends out beacons until the receiver (transmitter) at the destination node wakes up and hears the request. Of late, an asynchronous approach, also called the wake-up approach (Fig. 1.2(b)) is gaining popularity. When the node is monitoring the channel, the receiver is only looking for information that is binary i.e. whether the main receiver should wake up or not. In comparison, the receiver requirements when the main data is being communicated are more complex, requiring higher channel quality and higher speed [3]. These vastly different requirements for the monitoring state and for the communication state can be exploited to increase the node power efficiency by using a separate receiver, called the wake-up receiver, for channel monitoring. The wake-up receiver turns ON the main transceiver when another node in the network wants to communicate. For wake-up receiver power consumption below about $50\mu W$, the wake-up approach has been shown to be more power efficient than the duty-cycled approach [4]. Thus, the wake-

up approach is among the lowest power methodologies for duty-cycling the transceiver in a wireless sensor node. Once the wake-up receiver power consumption is below about 50 μW, the wake-up approach has been shown to be more power efficient than the duty-cycled approach [4].

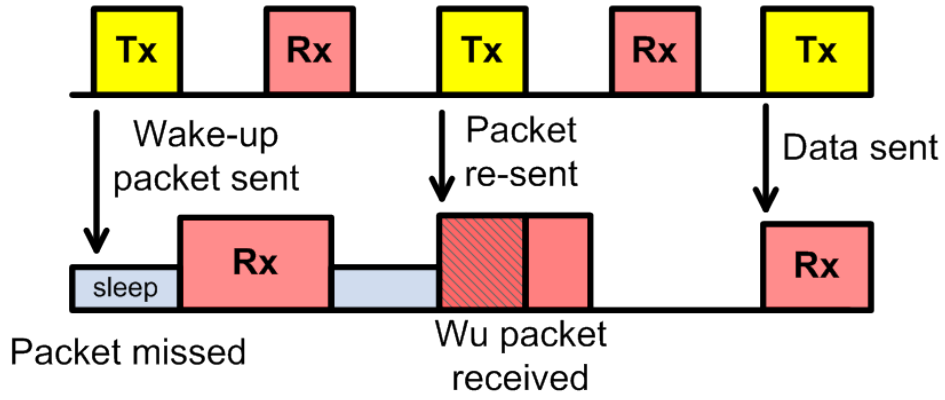

(a)

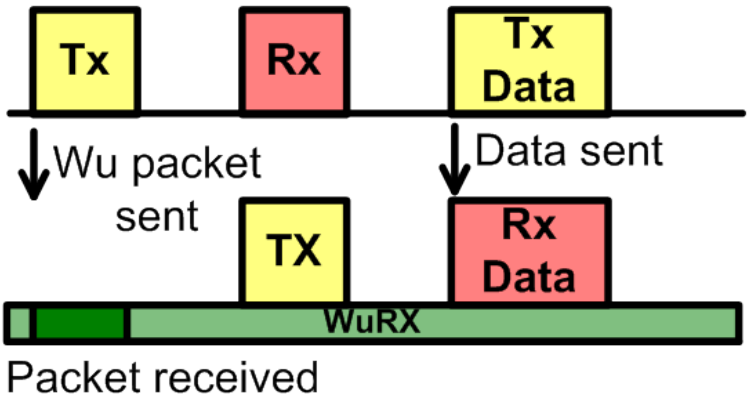

(b)

Figure 1.2: (a) Transmitter initiated fixed-rate duty-cycling, and (b) the wake-up receiver approach.

1.2 Related Prior Work

1.2.1 Low-power Duty-cyling Methodologies

Other than the three broad categories of node duty-cyling methodologies discussed above, several other methodologies have been proposed to cut down on the node power consumption:

In [5], the author proposes a radio triggered wake-up for sensor networks. The wake-up circuitry turns ON the node when it detects RF energy, which is also used to power the wake-up circuit itself. The paper estimates a distance range of 10 feet and it is claimed that that the range can be increased to 30 feet by using some additional circuitry. The methodology is among the lowest power wake-up solutions in the literature. However, the paper only presents calculated values of distance ranges and does not include any field measurements in real environments.

The S-MAC protocol proposed in [6] reduces the power consumption by synchronizing the sleep and the listening times of all the nodes. The data transmission takes place only during the listening times. Further, the listening times are reduced by letting the node sleep when data is being transmitted for some other node. However, the experimental results presented show high duty-cycle ratios of 30-40 %. Some improvements to S-MAC have been proposed in [7], but the duty-cycle ratios still remain high.

In [8], duty-cycle of 0.00125 % could be achieved. Instead of triggering a wake-up event on the detection of a pre-defined packet, the presence of a pulse at analog base-band

is used for wake up. However, this methodology increases the number of false wake-ups i.e. a node may wake up when the communication is actually intended for some other node. This can result in significant energy overhead for some applications.

In [9], the TDMA-W transmitter initiated protocol is presented. Each node is assigned two slots, the transmit slot (s) and the wake-up (w) slot. The nodes can transmit only during their s-slots and receive the wake-up packet during the w-slot. When a node has to be activated, the initiating node sends the wake-up packet during the w-slot of the destination. Once the destination node identifies the source node, it starts listening during the s-slot of the source. Compared to S-MAC, this methodology can increase the battery life by as much as 67 times.

1.2.2 Non-RF carriers for Ultra-low Power Communication

Low-power communications using carriers different from the conventionally-used radio frequencies have been proposed, but the requirements for a wake-up receiver in sensor networks are very different from what is available in these systems. Low frequency RF carrier waves (150 kHz) have been used for low-power wake-up in active RFID and location systems [10]. However, at such low frequencies, low wavelengths of electromagnetic waves mean that the RF antennas need magnetic coils, and become large and heavy, occupying a volume of as much as 50 cm^3 or so. Another drawback of the system is that it works only for distance ranges less than 3 m. Infra-red based communication has the potential to offer

a low-power solution [11], but requires accurate alignment of a narrow beam, which makes it unsuitable for sensor node applications.

1.3 Ultrasonic Wake-up

Since the overall node power becomes limited by the always-ON wake-up receiver, a lot of research is focusing on reducing the wake-up receiver power consumption. Recently, RF-based wake-up receivers with a continuous power consumption of around 50 μW have been presented. In [12], MEMS based high-Q filtering and uncertain-IF architecture are used to cut down on the receiver power. While, [13] uses a double-sampling technique to suppress offset and low frequency noise.

Ultrasound offers a good solution for the wake-up receiver application in sensor networks, primarily for three reasons. First, low carrier frequencies, of a few kHz to MHz, used for ultrasound enable receivers with ultra low power consumption. Second, ultrasonic transducers with form factors of a few centimeters are possible even for frequencies as low as a few tens of kilohertz because of short wavelength of ultrasonic waves (e.g. 8.5 mm @ 40 kHz). Third, ultrasonic transducers are low cost. This is an important factor for sensor network applications, which usually have a large number of distributed nodes. In [14], a low power detector for acoustic surveillance is proposed. But, the sensitivity requirements for the acoustic receiver are much relaxed compared to what is needed for a wake-up receiver. Similarly, [15] uses ultrasound for real time tracking of equipment and personnel.

However, the receiver sensitivity is poor because the front-end has been implemented using an ADC. Based on our review of the existing literature, the ultrasound-based communication systems are not suited for a low power application like the wake-up receiver in sensor networks.

Duty-cycled receivers for the main communication channel can receive a large number of bits in a short time and then turn OFF, thus their primary design target is energy/bit. In contrast, wake-up receivers are 'wireless switches' that turn on the main receiver. Unlike the duty-cycled receivers, the primary design target for wake-up receivers is low power consumption, while the data rate is not a primary concern. In this paper, an ultrasonic wake-up receiver system has been designed and in-field tested. It achieves an order-of- magnitude reduction in power consumption compared to the state-of-the-art wake-up receivers [12], [13].

Here, we envision a two-channel communication scheme (fig. 1.3) where ultrasonic wake-up is used to turn ON a conventional RF channel for data communications. The wake-up receiver can be conceived as an always ON 'wireless switch' which turns on the main channel, thus the figure-of-merit for the wake-up receiver is the continuous power consumption. This is very different from the main receiver which can operate at a high data rate, thus receiving a large number of bits in a short time and then turn OFF. The figure of merit (FOM) for the main receiver is power consumption of the receiver divided by the data rate, commonly expressed as energy/bit.

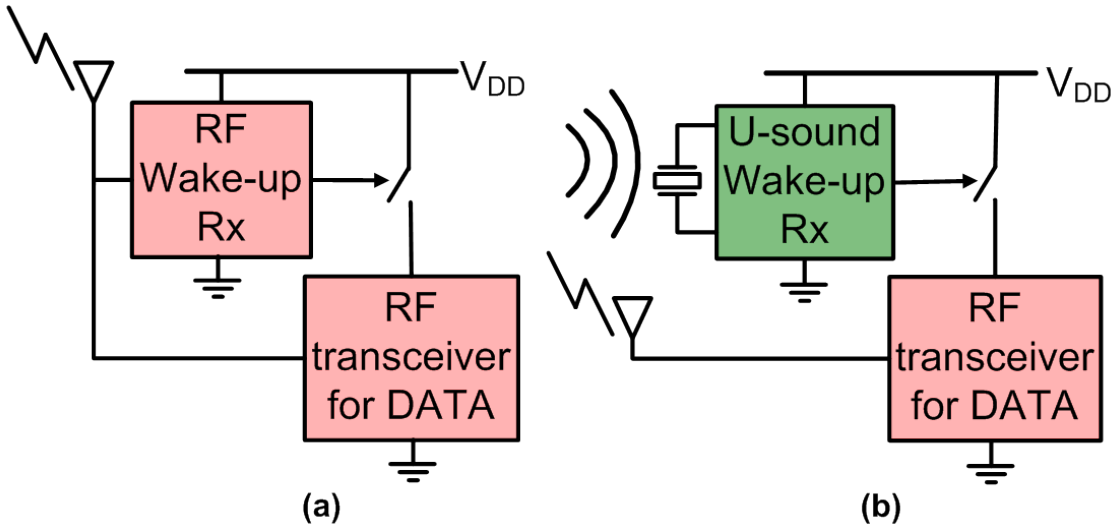

Figure 1.3: (a) RF-based communication for both the main data and the wake-up. (b) Proposed communication scheme that uses ultrasound for wake-up and RF for main data communication.

1.4 Contributions

An ultra-low power wake-up receiver IC was designed, fabricated and field-tested. The main contributions are listed below:

- The design feasibility of a 0.6-V ultra-low power 4.4μW 250 bps wake-up receiver using ultrasound is demonstrated.
- Ultrasonic data link measurements are done in typical environments like lecture hall, car garage etc.
- The feasibility of an ultrasonic wake-up network is demonstrated by designing and field-testing a network of three receivers and one transmitter base station; for the proof-of-concept, the digital circuitry was implemented on a commercial FPGA.
- Design methodologies were proposed for optimally choosing the wake-up packet

length and the wake-up decision threshold to achieve high values of wake-up detections, while keeping false alarms low; measurements were done to substantiate this methodology.

1.5 Thesis Organization

The thesis is organized into seven chapters. This first chapter provides a brief overview of the low-power receiver duty-cycling methodologies and also discusses the existing low-power wake-up receivers. In chapter 2, the existing data communication applications for ultrasound are discussed; also presented are the benefits of using ultrasound for these applications.

Chapter 3 presents the design of the ultrasonic wake-up receiver. The chapter begins with a top-level explanation of the electro-mechanical system; this is followed by the characterization of the mechanical part of the communication system, consisting of the TX-RX transducer pair and the ultrasonic channel. Then, the circuit design of the receiver circuit and its electrical-only characterizations are presented. The chapter concludes with in-field measurements for a through-air ultrasound data link in a lecture hall.

In chapter 4, first the performance parameters for the wake-up receivers are discussed. The design of the communication system, consisting of both the hardware and the VHDL implementation of the digital circuitry, is discussed next. Then, in-field measurements on a wake-up network consisting of three receivers and one transmitter are presented. The

chapter concludes with a summary of the challenges in ultrasound data communication, as observed from the network-level measurements.

Chapter 5 discusses the design of an ultrasonic transmit transducer. First, the electrical equivalent circuit of the transmit and the receiver transducers are derived. Then, the effect of different physical properties of the transducer materials on the transmit transducer performance parameters are discussed. Finally, the designs of 40 kHz and 80 kHz transmit transducers, with improved bandwidth compared to the commercial transducers, are presented.

The appendix presents the verilog model parameters used for full-receiver simulations. Also discussed are the effects of design choices like the front-end gain and the current consumption on the signal-to-noise performance of the receiver.

Chapter 2

Ultrasound in Data Communication Applications

2.1 Existing Applications of Ultrasound

Medical Imaging: Ultrasound is extensively used in diagnostics for medical imaging. A phased array sweeps the ultrasonic beam and the image of the soft tissues, like muscle and internal organs, is constructed based on the intensity and time delay of the echoed ultrasound [16]. Ultrasound is also used for monitoring heartbeat and blood flow from outside the body [17].

Industrial Applications: Ultrasound is also used in many industrial applications, for example, in detecting leakage and in fracture analysis of gas pipes [18], and for detecting cracks in bridges [19].

Underwater Data Communication: Ultrasound waves exhibit much superior propogation than the RF waves; data rates of more than 19.2 kbps have been demonstrated with 30 kHz carrier for acoustic modems [20].

Acoustic Communication: Device-to-device and device-to-human communications have been presented in [21] and [22] with emphasis on using the existing microphones in laptops and mobile devices. Recently, this approach has been commercialized for proximity marketing; product information is transmitted to smartphones or tablets using sounds signals [23].

Through-metal Communication: Data communication through metal walls has many applications. For example, in nuclear power plants for wirelessly transmitting the sensor information through metal walls of gas cylinders, and in submarines for wireless power and data delivery through hulls. Radio waves can not be used for this application because of shielding effect of the metals. Ultrasound has been used for through-metal communication [24] using commercial-off-the-shelf components by coupling ultrasonic waves into the wall.

Ultrasonic presence detector microsystems: Fully integrated ultrasonic presence detectors have been proposed [25], but they rely on MEMS sensors that need expensive fabrication processes. Further, because of the high Q of these sensors they have to be heated to tune their characteristics, which results in a relatively large power consumption of several milliwatts.

2.2 Ultrasound in Wireless Sensor Networks

Within the application area of wireless sensors, ultrasound or acoustic data has been used for location, localization and surveillance. In [26], authors propose a methodology in which the time difference of flight between ultrasound and RF is used by mobile devices to learn about their environment, and then decide whom to advertise their information to. Ultrasound-based positioning systems [27]- [31] use the difference between the flight times of radio waves and ultrasound to determine the distance between two nodes, and the direction of arrival is estimated by the time difference of detection of ultrasound at different elements of the transducer array. Ultrasonic communication is used for equipment and personnel tracking in Electromagnetic Interference (EMI) sensitive environments like hospitals because, unlike radio waves, ultrasound does not interfere with sensitive hospital equipment. Sonitor Technologys tracking system is an example of such a system [15]. In [14], the presence of a 'novel' object in an area is detected by using its acoustic signature. On detection of an object, a wake-up detector turns on the surveillance network to full functionality. We emphasize that the ultrasound wake-up presented in this work is for node to node communication and not for event detection. In addition to these applications, ultrasound data has been proposed for machine-to-machine and device-to-device communication [32], [33]. In [34], acoustic communication has also been proposed for underwater sensor nets in low-power and low distance applications.

2.3 Benefits of Using Ultrasound and Potential Applications

Apart from ultra-low power communication, ultrasound offers several other benefits like:

- **No Electromagnetic Interference Issues.** Unlike radio waves, which can electromagnetically interfere with the EMI-sensitive equipment, ultrasound offers a safe communication medium in tightly EMI-regulated environments like hospitals and nuclear power plants. As explained in section 4.4, many of the commercially available location and tracking systems used in hospitals are ultrasound-based.

- **Low Cost.** For the application of wireless sensor networks, where a large number of sensors may distributed to sense environmental variables, the accompanying hardware must be low cost. The piezoelectric ultrasonic transducers and the CMOS chip used in this research can be manufactured cheaply for mass market applications.

- **Sonar-based Applications.** Ultrasound-based sonar modules [36] are widely available commercially and find applications in robotics and aerial vehicles. A class of Micro-aerial Vehicles (MAV), called ARducopter, are being developed for law enforcement, observation and monitoring applications. These vehicles can benefit from the low-power custom design of the ultrasonic sonar [37] as the weight and the form factor of batteries is often a concern for this application.

- **Application in a Tag Networks.** The final goal is to use the ultrasonic wake-up technique in a bigger system like EnHANTs (Energy-harvesting Active Networked Tags), which is being developed at Columbia University [38]. EnHANTs are powered by light energy harvested in typical indoor environments and can provide infrastructure for novel tracking applications. A key challenge in the implementation of these tags is the realization of low power communication circuitry, a challenge that can potentially be overcome by an ultra-low power wake-up solution.

- **Safe Communication Medium.** Unlike the tightly regulated radio spectrum, there are no legally enforceable limits on the transmission of ultrasound. Ultrasound is in general considered safe for the human body. For this reason, the ultrasound emission limits recommended by various government and non-government organizations are relatively relaxed. For diagnostic ultrasound, the Food and Drug Administration (FDA) recommends ultrasound pressure levels to be below 620 Pa [35]. The Occupational Safety and Health Administration (OSHA) imposes limits for frequencies below 8 kHz [39], but there are no limits on ultrasonic frequencies. A professional organization of industrial hygienists, American Conference of Governmental Industrial Hygienists (ACGIH), recommends pressure levels below 355 Pa for ultrasound [40]. Most of the recommendations discussed above are for applications that are very different from wireless data communication, but they still give an idea of the relative safety of ultrasound. In our field measurements, for a communication distance range

of 18m, pressure at a distance of 1 foot from the transmitter is 10 Pa. Thus, the transmitted pressure levels in this research are more than two orders of magnitude below the recommendations.

Chapter 3

Ultrasonic Wake-up Receiver

3.1 System Level Design

3.1.1 The Electro-Mechanical Communication System

Figure 3.1 shows a block-level diagram of the through-air ultrasound data communication system. We have used on-off Keying (OOK) modulation because it enables the use of simple energy detection receivers; these receivers are an attractive choice for a power constrained application [12] like wake-up because they don't need a frequency synthesizer for the LO generation and can thus be realized with ultra-low power consumption. At the transmitter, an OOK electrical signal is generated by mixing the data bits with a 40.6-kHz sine-wave carrier. The electrical signal excites the transmit transducer, which produces modulated ultrasonic pressure waves. These pressure waves travel through air and suffer

path losses before reaching the receiver, where they are converted into an electrical signal by the receive transducer. The wake-up receiver IC is designed for ultra-low power consumption, and extracts the transmitted bits from the received electrical signal such that the required bit error rates (BER) are achieved for the targeted communication distances.

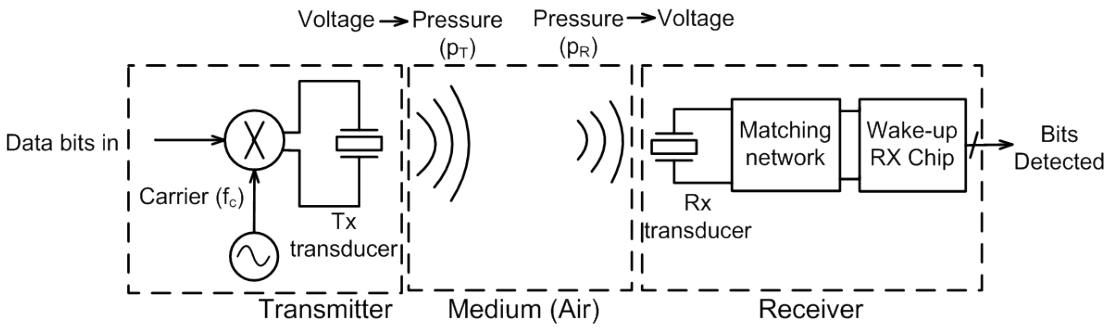

Figure 3.1: Block diagram of the ultrasound data communication system.

3.1.2 Ultrasonic Characterization

3.1.3 Receive and Transmit Ultrasonic Transducers

The envisioned application environment for this work consists of an ultrasonic transmitter in the base station and an ultrasonic receiver in each network node; the base station may be powered from an electrical outlet, while the nodes are battery powered. Thus, the transmit and the receive transducers have different sets of requirements. The base station transmit transducer must have a high transmit efficiency, while the form factor is not a primary criterion. On the other hand, the receive transducers are being used at the network nodes and

must have a small form-factor for them to work unobtrusively within the physical environment. The ultrasonic transducers used in this work are made of piezoelectric materials that have the property of converting electrical energy into mechanical energy and vice-versa.

At the transmitter, a highly efficient metal-piezoelectric unimorph [41] is used. The unimorph is cylindrical in shape, and has a diameter of 2.5 cm and a height of 1.2 cm. This class of transducers exploits the difference between the piezoelectric constants of Aluminum and PZT (Lead Zirconate Titanate) to enhance the efficiency of ultrasound transmission. These transducers are directional; however, several transducers can be easily combined to achieve omnidirectional transmission.

The receive transducer [42] consists of a piezoelectric film (Fig. 3.2(a)), Polyvinylidene Fluoride (PVDF), wrapped around a hollow plastic cylinder that has a diameter of 1.5 cm and a height of 2.6 cm. To match the output impedance of this transducer with the receiver input, we study the input admittance of the transducer, Y_{IN}. It consists of a capacitive part because of piezoelectric film capacitance (B_c), a resistive part because of dielectric loss (G_{loss}), and a series LCR circuit to model the electrical equivalent of the transducer's mechanical resonance (Fig. 3.2(b)) [43]. The real and the imaginary parts of the measured admittance are shown in Fig. 3.2(c) and Fig. 3.2(d). While the real part is dominated by the dielectric loss, some contribution from the transducer action (G_t) is also observed ($=\frac{R_1}{{R_1}^2+(\omega L_1-\frac{1}{\omega C_1})^2}$); a peaking is observed in G_t at the mechanical resonance frequency of the transducer at 40 kHz. The imaginary part is dominated by B_c, but also has

a contribution from the transducer action, $B_t = \frac{-(\omega L_1 - \frac{1}{\omega C_1})}{{R_1}^2 + (\omega L_1 - \frac{1}{\omega C_1})^2}$. The inset in Fig. 3.2(d) shows B_t which has a zero-crossing at the mechanical resonance frequency. As can be seen from the discussion above, the input admittance of the transducer is dominated by the film capacitance and the dielectric loss; the contributions from the transducer action dwarf in comparison. Thus, while choosing the first-stage amplifier topology, we use the transducer model shown in Fig. 3.3(a). The electrical signal induced because of piezoelectricity is modeled as a current source in parallel with the transducer input admittance.

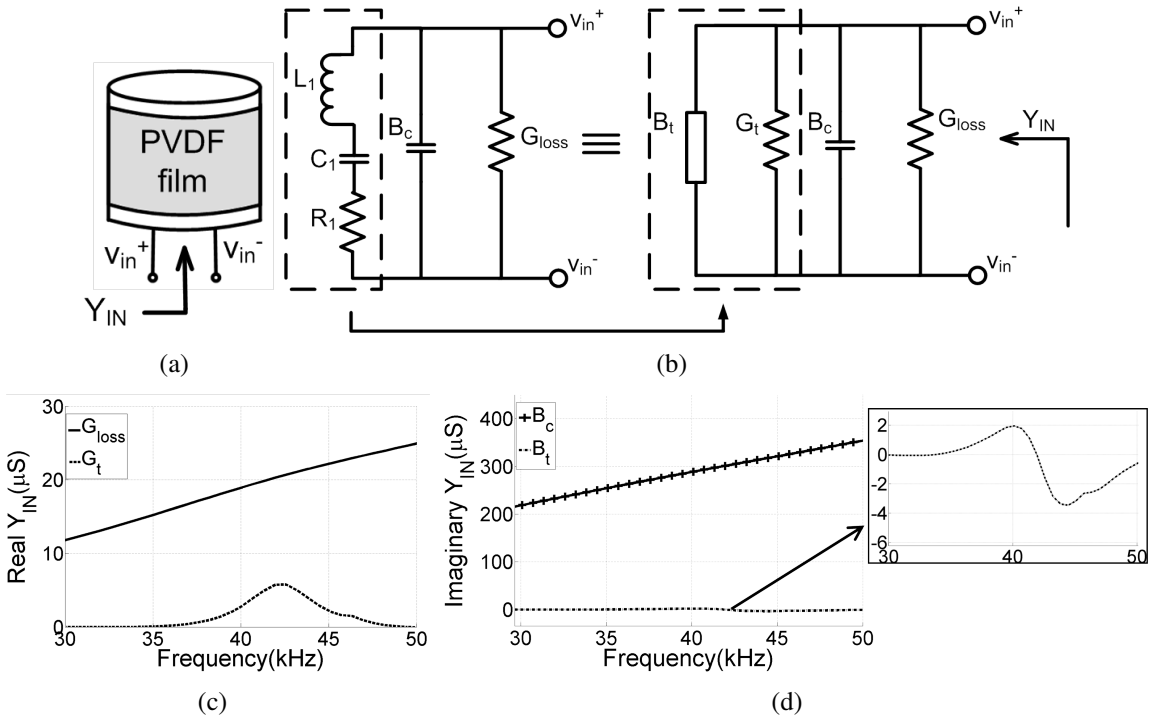

Figure 3.2: (a) Structure of the piezoelectric receive transducer, (b) the equivalent circuit, (c) the measured real admittance, and (d) the measured imaginary admittance.

3.1.4 First-stage Amplifier and the Receive Transducer

The first-stage amplifier determines the noise performance of the receiver. With the given receive transducer, several first-stage topologies were considered for best possible noise performance. Two prominent ones are the TIA (Trans-Impedance Amplifier) and the common-source amplifier with a matching circuit. A TIA is often used with transducers whose output signal is a current [44]. The input impedance of the TIA ($1/g_m$ in Fig. 3.3(a)) must be much lower than the transducer output impedance (1/(ωC_{FILM})); otherwise the AC current signal from the transducer is lost in C_{FILM}, resulting in a poor signal-to-noise ratio at the output. This imposes a limit on the minimum value of the transistor transconductance and hence a limit on the minimum current consumption of the circuit. For the receive transducer used in this research, assuming a g_m/I of 30, we would need $I_{TIA} >> 10$ μA, which is too high for the power-consumption levels targeted in this research. In comparison, a common-source amplifier with a matching circuit (Fig. 3.3(b)) meets the performance requirements with lower current consumption because of the passive voltage amplification of the received signal by the LC tank, which was used to match the transducer's output admittance. Therefore, in this work, we have used this circuit to realize the first stage of the receiver; the surface-mounted tank (L_m=10 mH, C_m=0.41 nF) resonates with the transducer film capacitance (C_{FILM}=1.14 nF) at 40 kHz. The matching network-transducer combination has an electrical quality factor (Q) of 14 and a parallel resonant impedance ($R_p||R_{LC}$) of 36.3 kΩ.

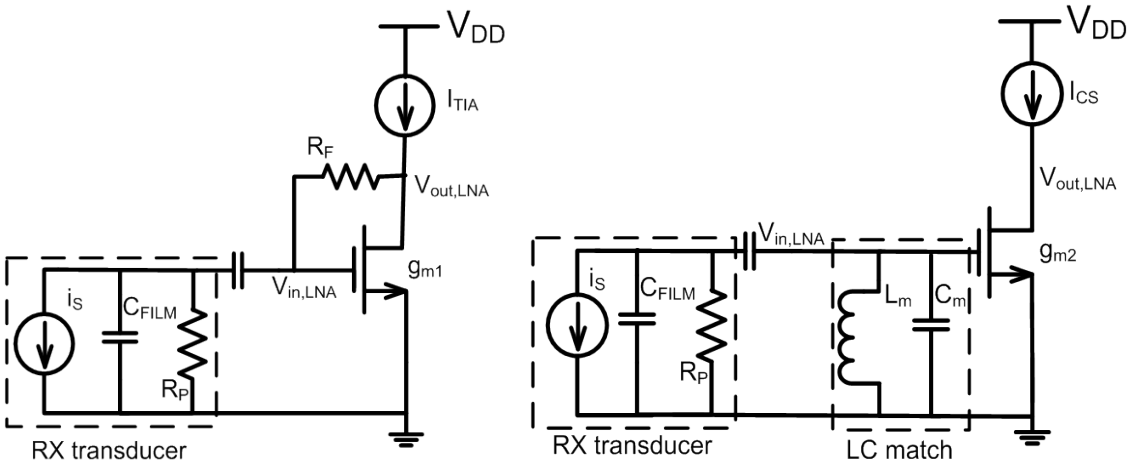

Figure 3.3: Candidate topologies for the low noise amplifier: (a) a transimpedance amplifier, and (b) a common-source amplifier with LC matching circuit.

3.1.5 Link Budget

In this section, the transmission characteristics of the TX-RX transducer pair are combined with the pressure vs. distance measurements done in a lecture hall, to derive the sensitivity requirements of the ultrasonic receiver IC; the specifications have been derived for a communication distance range of 8 m, the length of a typical lecture hall. The bandwidth and the insertion loss of the TX-RX transducer pair are measured by sweeping the electrical excitation to the TX across frequency and then observing the open-circuit voltage across the RX transducer (Fig. 3.4). The bandwidth of the transducer pair, 300 Hz, is determined by the high Q ($>$100) of the transmit transducer which limits the communication data rate; in comparison, the bandwidth of the receiver electronics is much wider at 2 kHz. The insertion loss of the pair at the resonance frequency of 40.6 kHz is -61dB for a TX-RX dis-

tance of 1 foot. A relatively low value of the insertion loss is because of the inherently low electro-mechanical conversion efficiency (k_5^2 = Energy converted per input energy) of the piezoelectric materials – for PZT (transmit transducer), k_5^2 is 0.15, while for the PVDF (receive transducer), k_5^2 is 0.025 [43].

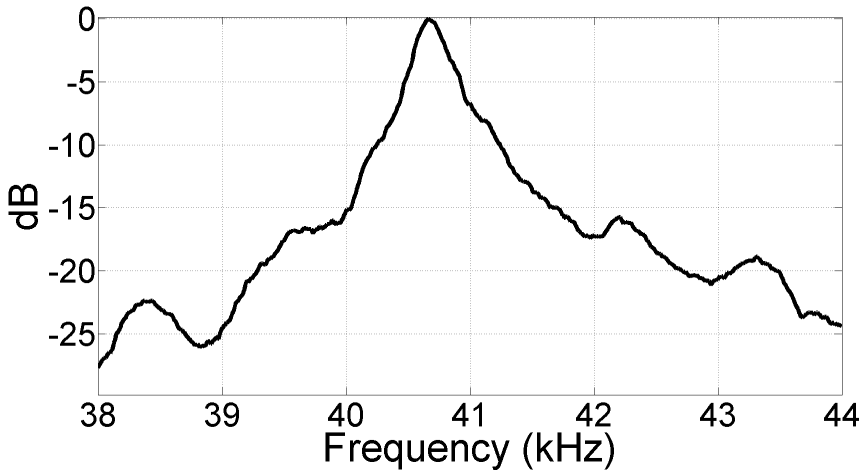

Figure 3.4: Measured transmission characteristics vs. frequency of the TX-RX ultrasound transducer pair.

Pressure vs. distance measurements (Fig. 3.5) were done in a lecture hall in the presence of typical interferers and reverberations by using a reference acoustic pressure measurement system [45]. The pressure is observed to be inversely proportional to distance – Pressure $\propto$ 1/Distance^n – with an exponent n of around 1.1. The measured value of n is greater than 1 because of reverberations and multi-path.

Insertion loss at the targeted communication distance range of 8 m is calculated by

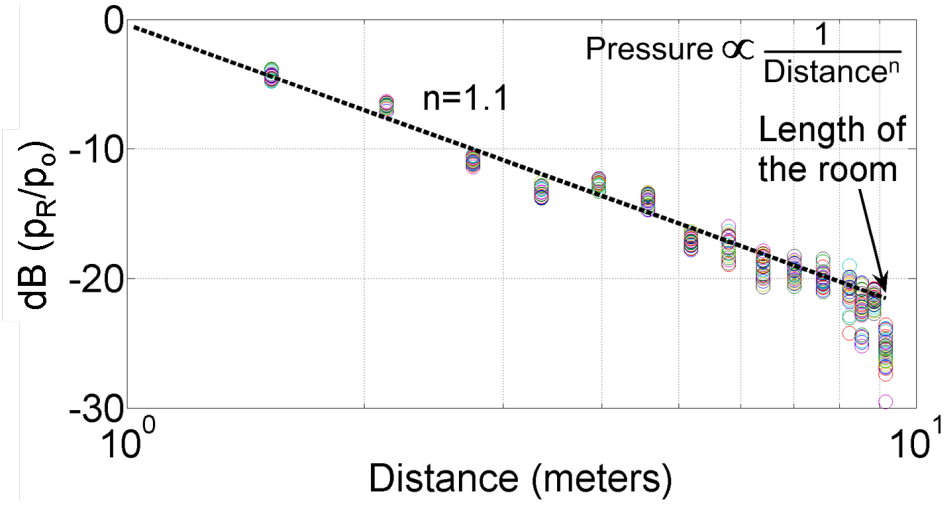

Figure 3.5: Received pressure (p_R) (normalized for a TX-RX distance of 1 m) vs. TX-RX distance inside a lecture hall, measured using a reference acoustic pressure measurement system [45].

using the formula:

$$IL(d) = IL(1\ foot) - n\ 20log_{10}\left(\frac{d}{1\ foot}\right) \tag{3.1}$$

where $IL(d)$ is the insertion loss for a TX-RX distance, d. Using an exponent n of 1.1, as derived from the pressure vs. distance measurements (Fig. 3.5), the insertion loss is calculated to be -92.2 dB at 8 m.

In this work, we are targeting an order-of-magnitude reduction in both the transmit power and the receiver power consumption. RF-based wake-up receivers [12], [13] use a transmit power of around 1 mW; here, we have used a much lower transmit power of 16 μW. For the transmit transducer used in this research, this corresponds to an excitation of 70.7 mV_{rms}; for this excitation, the open-circuit voltage at the receive transducer at a distance of

8 m is 1.73 μV_{rms}. Since we are using an LC tank at the receiver, the voltage at the input of the receiver IC ($v_{in,LNA}$) will be passively amplified, by a factor of $R_p||R_{LC}/(1/\omega C_{FILM})$, to 18.3 μV_{rms}. Thus, we target a receiver voltage sensitivity (S_{in}) of around 18 μV_{rms}.

The voltage noise squared density at the input of the receiver because of matching network-transducer combination is $4kT(R_p||R_{LC})$. Thus, the signal-to-noise ratio (SNR_{in}) at the receiver input, for the 2-kHz bandwidth (BW_t) of the combination and for an input voltage around the sensitivity level, is given by $\frac{S_{in}^2}{(4kTR_p||R_{LC})BW_t}$, which is around 24.5 dB. For the OOK-based energy-detection receiver used in this research, a SNR_{out} of around 10 dB is needed to achieve a BER of better than 10^{-3}. Thus, the noise figure specification (NF_{RX}) for the receiver is 14.5 dB (=$SNR_{in} - SNR_{out}$). Even though the noise performance of the OOK-based energy detection receivers is poorer as compared to their coherent counterparts, a NF of 14.5 dB is achievable while maintaining an ultra-low power dissipation.

3.2 Ultrasonic Wake-up Receiver IC Design

The ultra-low power OOK-based energy-detection receiver (Fig. 3.6) in this work uses self-mixing for signal downconversion. To achieve good dynamic range and to realize a receiver with a sensitivity level of a few tens of μV, the LNA is followed by a cascade of amplifiers. The downconversion is realized by using a Gilbert-cell based self mixer. The down-converted baseband signal is then amplified, using op-amp based resistive-feedback

amplifiers, to fully utilize the dynamic range of the 5-bit successive approximation register (SAR) analog-to-digital converter (ADC).

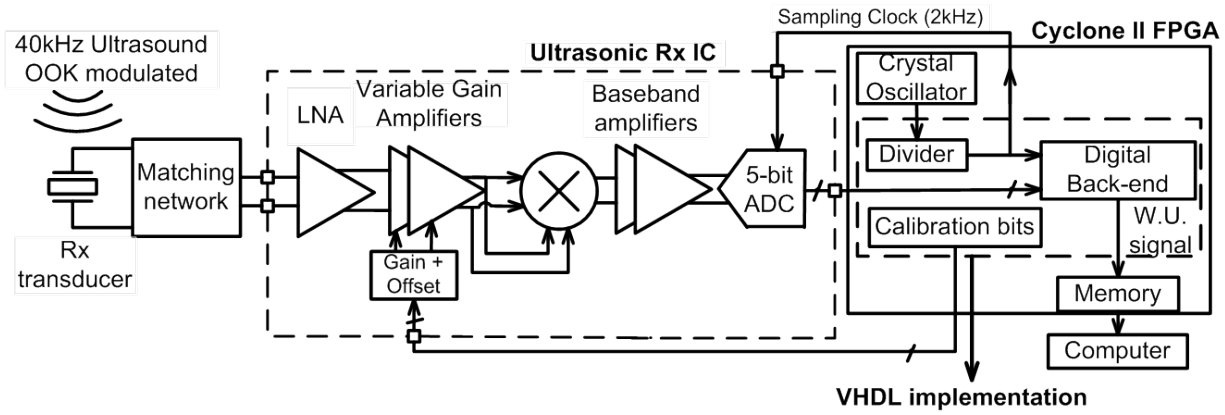

Figure 3.6: Block diagram of the ultrasound wake-up receiver.

3.2.1 Low Noise Amplifier Design

The first stage is realized by using a simple differential amplifier (Fig. 3.7). Instead of an active PMOS load, a resistive load has been used. Despite a lower voltage gain, the resistive load offers better receiver noise performance. Thanks to the lower noise of the resistors. In cascaded amplifiers, the noise of the first stage contributes directly to a degradation of the signal-to-noise ratio. To keep its noise contribution sufficiently low, the first stage is designed to consume as much as 40 percent of the overall analog receiver power; the tail current, I_{LNA}, is 2.7 μA. The ultrasound carrier frequencies of 40 kHz are very low compared to the intrinsic device speeds in 65-nm CMOS and devices can be operated deeply into weak inversion to achieve maximum current efficiency (g_m/I=31) to keep the thermal

noise low. However, careful attention must be paid to keep the flicker noise low; for this reason, large NMOS devices are used in the carrier-band amplifiers. The first-stage differential NMOS devices (M_{16a}, M_{16b}) were sized 80 μm/0.12 μm, thus keeping the flicker noise corner (f_c) to 6 kHz, well below the carrier frequency of 40 kHz. Load resistors (R_{L1}, R_{L2}) of 260 kΩ have been used; a higher value will give more gain, but the maximum usable resistance value is limited by the tight voltage headroom in this low-voltage (0.6 V) design. The stage has a voltage gain ($v_{in,CB}/v_{in,LNA}$) of 14.7 dB and has a noise figure ($SNR_{in,LNA} - SNR_{in,CB}$) of 6.15 dB.

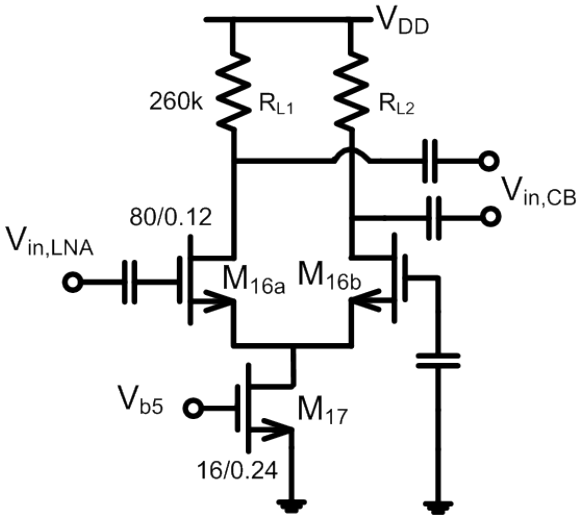

Figure 3.7: Low noise amplifier circuit. Device sizes (W/L) are in the units of μm/μm and devices in symmetrical paths have the same sizes. DC biasing is not shown.

3.2.2 Carrier-band Amplifiers

The gain in the carrier-band ($A_v = v_{in,mix}/v_{in,LNA}$) must be sufficiently high to suppress the noise contribution from the baseband amplifiers. To analyze the effect of front-end gain

on the receiver noise figure (NF_{RX}), [1] a verilogA model of the receiver was developed, taking into account the noise contribution of each stage, both the thermal noise and the flicker noise. A cascade of four amplifiers succeeds the first-stage LNA; the first and the last stage amplifiers are fixed-gain, while the other two amplifiers are gain-tunable. For A_v less than about 40 dB, the receiver output noise is dominated by the flicker noise of the baseband-amplifiers, and varies as 20 dB/decade (Fig. 3.8) because of the squaring action of the self-mixer. However, for larger values of A_v ($>$ 48 dB), the noise contributions from the LNA and the second-stage amplifier dominate the receiver output noise; any increase in the front-end gain beyond this point does not improves the receiver performance appreciably. Keeping some margin, the receiver presented in this work has been designed for a maximum front-end gain of 55 dB.

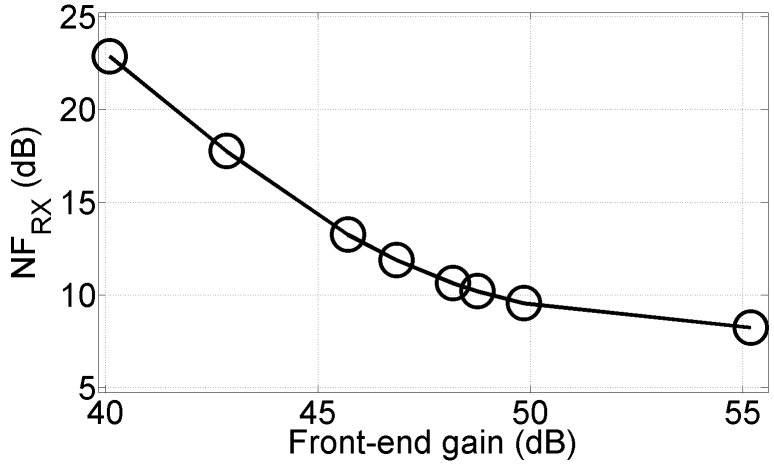

Figure 3.8: Receiver noise figure ($SNR_{in,LNA} - SNR_{in,ADC}$) with front-end gain ($v_{in,mix}/v_{in,LNA}$).

[1] A mathematical model has been used to speed up the simulation times. Results from the model were verified to match closely with the transistor-level simulations.

For the fixed gain stages, we have used NMOS differential amplifiers with PMOS loads; the amplifiers are accompanied by CMFB circuits (Fig. 3.9). The input device pairs (M_{6A}, M_{6B}) were sized at 200 μm/0.12 μm and operate in weak inversion with a g_m/I of 32. Current levels have been kept low at a few 100 nA, resulting in a high small-signal output resistance, $r_o = V_A/I$. For a typical early voltage of around 1 V, r_o is around 10 MΩ for a 0.12-μm device. These high output resistances in combination with the capacitive input impedance (around 300fF, dominated by miller capacitance due to C_{gd}) of the next stage would, however, result in poles around 50 kHz, which is too close to the ultrasonic carrier frequencies. Therefore, differential amplifiers with NMOS diode-connected loads have to be used as buffers to connect the amplifier outputs to the input of the next stage. The first and the last PMOS-load stages have gains of 16.5 dB and 11.2 dB.

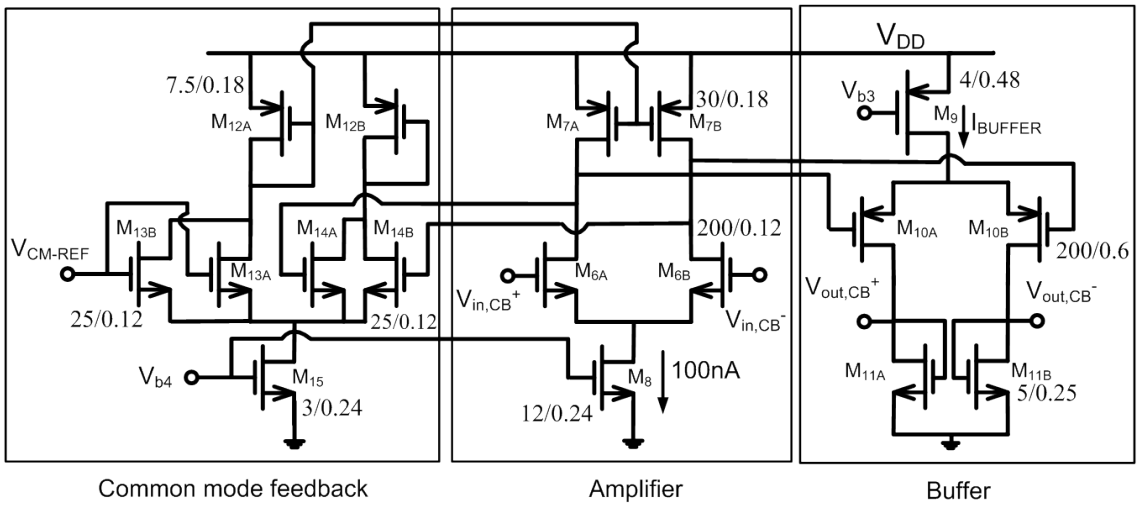

Figure 3.9: Carrier-band amplifier circuit. Device sizes (W/L) are in the units of μm/μm and devices in symmetrical paths have the same sizes. DC biasing is not shown.

The two VGAs are identical and are made using NMOS differential amplifiers with

diode-connected PMOS loads (Fig. 3.10). Connected in parallel with the diode-connected PMOS load are the PMOS-based switched-current sources ($I_{VGA,1}$,$I_{VGA,2}$), which are used to control the current through the PMOS load and thereby tune the amplifier gains (g_{mn}/g_{mp}). The tail currents ($I_{VGA,tail}$) for the two VGAs are 139 nA and 147 nA. For both the VGAs, $I_{VGA,1}$ and $I_{VGA,2}$ are 25 nA and 33 nA, giving gain tunability (using g[0:1] and g[2:3]) from 0 dB to 14.4 dB and 0 dB to 10.2 dB. Operation in weak inversion ensures a high g_m/I of 31. The simulated overall noise figure ($SNR_{in,CB} - SNR_{in,mix}$) of the carrier-band is 2.5 dB.

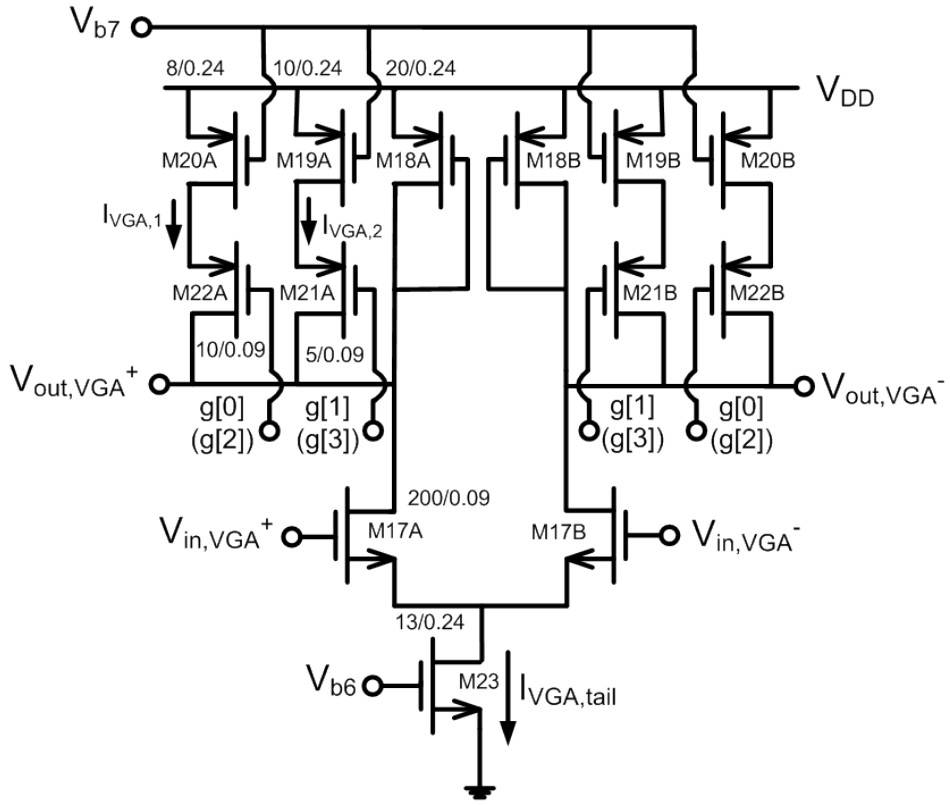

Figure 3.10: Variable-gain amplifier circuit. Bits g[0:1] (g(2:3)) are used to control the first (second) VGA. Device sizes (W/L) at in the units of μm/μm and devices in symmetrical paths have the same sizes. DC biasing is not shown.

3.2.3 Base-band Amplifiers, Self-mixer and 5-bit SAR ADC

The envelope of the carrier-band signal is demodulated by using a Gilbert-cell based self-mixer (Fig. 3.11) that outputs a current signal into a transimpedance amplifier, which is realized with resistive feedback around an OTA. In this work, all of the transistors are operating in weak inversion; the current through these transistors is given by $I = I_s exp\left(\frac{V_{GS}}{nkT/q}\right)$. The differential output current ($i_{out,BB1^+} - i_{out,BB1^-}$) of the mixer is

$$i_{out,BB} = I_{BIAS,mix}\frac{\left(exp\left(\frac{v_{in,mix}}{2nkT/q}\right) - exp\left(\frac{-v_{in,mix}}{2nkT/q}\right)\right)^2}{exp\left(\frac{v_{in,mix}}{2nkT/q}\right) + exp\left(\frac{-v_{in,mix}}{2nkT/q}\right)} \tag{3.2}$$

where $I_{BIAS,mix}$ is the tail current as shown in figure, $v_{in,mix}$ is the input signal and n is the sub-threshold slope factor. For smaller input signals ($v_{in,mix} << 2\sqrt{3}nkT/q \approx 120$ mV @ 300 K) [2], the expression reduces to:

$$i_{out,BB} = 2I_{BIAS,mix}\left(\frac{v_{in,mix}}{2nkT/q}\right)^2 = a_2 v_{in,mix}^2 \tag{3.3}$$

Thus, the squared conversion gain, a_2, is proportional to the bias current. In this work, we have used $I_{BIAS,mix}$=29 nA, giving a simulated a_2 of 12 μA/V^2. A higher mixer conversion gain could be achieved by using a larger mixer bias current; instead we achieve a high receiver gain by designing the 40 kHz front-end for high gain. This technique is more efficient because unlike RF-based receivers, where front-end gain comes at the cost

[2] For an input voltage at the targeted sensitivity level, $v_{in,mix} = 29mV_{p-p}$; thus, the simplifying assumption.

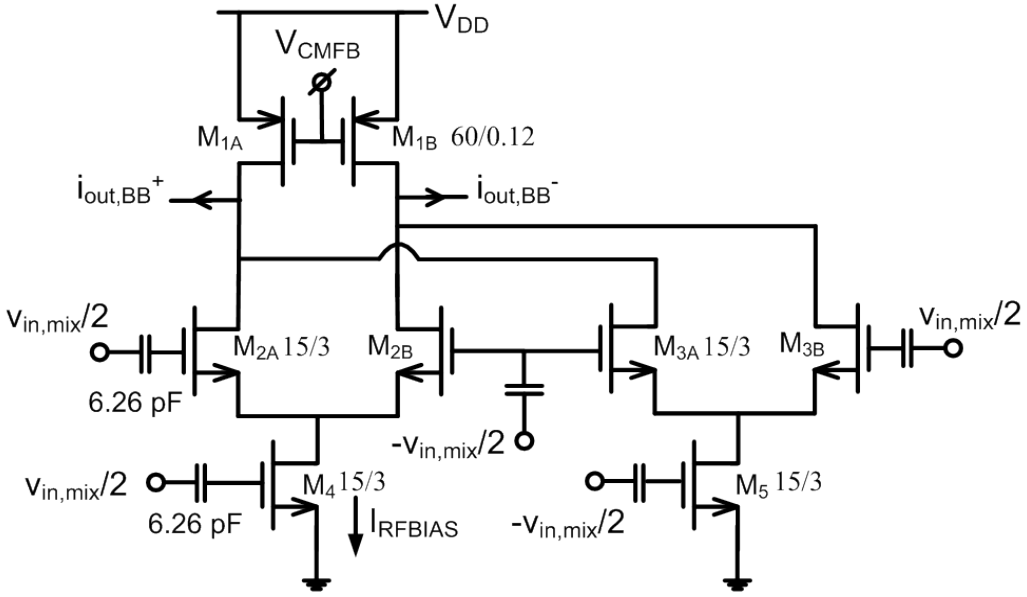

Figure 3.11: Gilbert-cell based self-mixer. Device sizes (W/L) are in the units of μm/μm and devices in symmetrical paths have the same sizes. DC biasing is not shown.

of power-hungry gigahertz amplifiers, any additional gain in the ultrasonic front-end can be realized with a power consumption of just a few tens of nanoamperes.

The output of the baseband must be within the dynamic range of the ADC and therefore has to be amplified further. For an input signal ($v_{in,LNA}$) at the targeted receiver sensitivity, the output of the TIA ($V_{in,BB1}$) is 1.2 mV_{p-p} (Fig. 3.12). This is well below the 19 mV resolution of the 0.6-V 5-bit ADC, which succeeds the baseband amplifiers. Thus, we amplify the signal by 30 dB using a cascade of two OTA-based resistive-feedback amplifiers. The OTAs are fully-differential two-stage amplifiers, consisting of a differential amplifier with PMOS load and a CMFB circuit, followed by a common-source amplifier stage. The OTAs have to work at low frequencies of a few kilohertz; thus, to keep the 1/f flicker noise low, NMOS devices at OTA inputs are sized large, $50\mu m/\ 0.24\mu m$. The power consump-

tion of the base-band amplifiers is limited by the current that the OTAs have to drive into the resistive loads to achieve the required voltage swing. To keep this current below a few hundred nanoamperes, while achieving an output voltage swing of a few tens of mVs, resistors in the order of MΩs have been used. These large resistors are realized by using poly resistors having a density of 5.5 kΩ/μm^2. Using even larger resistors would decrease the power consumption of the OTAs, however this comes at the cost of a substantial increase in area.

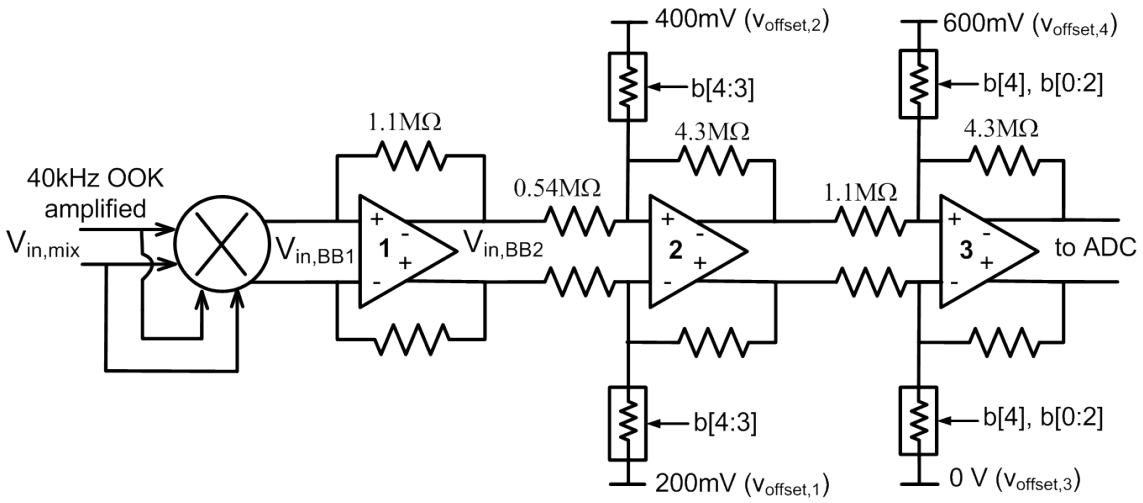

Figure 3.12: Op-amp based resistive feedback amplifers in the base-band.

A DC-offset cancellation mechanism has been implemented to cancel the offsets due to self-mixing and device mismatch. Switched resistors, of the order of a several M Ωs, have been used to inject differential currents into the feedback resistors. Poly resistances of a total value of 100 MΩ and occupying a total area of 500 μm x 100 μm have been

used. Though the resistor area could have been reduced by using MOSFET resistances, poly resistors have been used to keep the flicker noise low.

The analog receiver output ($v_{in,ADC}$) is converted into a 5-bit digital word using a fully-differential SAR ADC. The anti-aliasing filter is implemented by using a first-order RC filter in the last-stage baseband amplifier. A capacitive DAC, as opposed to a resistive DAC, has been used so that the same circuit can be used both as a DAC and as a sampling circuit; another benefit of using capacitive DACs is that they do not suffer from any static power consumption. A sampling rate of 2 kS/s was used for over-sampling the data by eight times; the ADC power consumption at this sampling rate was measured to be 400 nW.

3.2.4 Digital Back-end

As explained in detail later in section 4.2.3, digital clock recovery and dc-offset calibration were implemented on a cyclone II FPGA using Verilog Hardware Description Language (VHDL). Based on the number of combinational functions and logic registers occupied on the FPGA, the power consumption of the digital back-end circuit is estimated to be 15 nW; this is very small compared to the power consumption of the analog front-end IC, which we have built and have shown to be able to function with a power consumption of 4.4μW.

3.3 Experimental Results

The chip photograph is shown in Fig. 3.13. The receiver was fabricated in a 65-nm CMOS process and occupies a silicon area of 1.24 mm^2.

3.3.1 Electrical-only Measurements

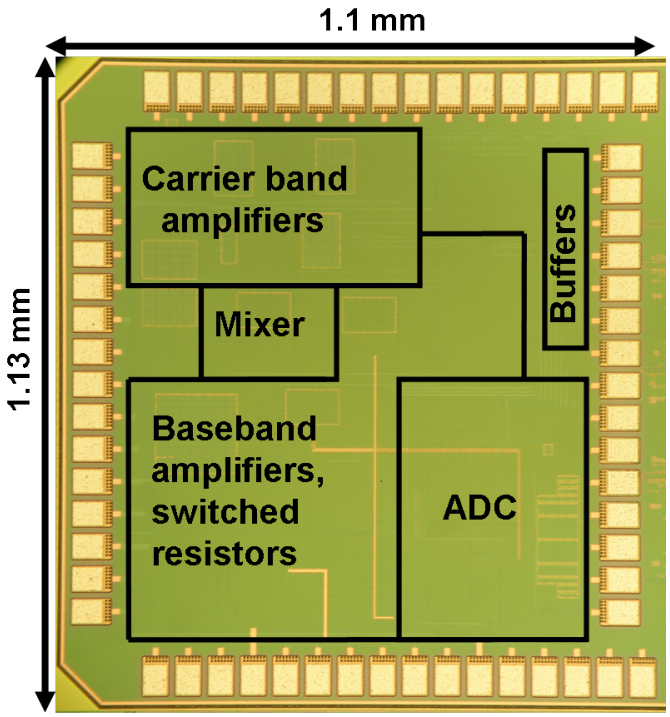

Figure 3.13: Receiver die photo in 65nm CMOS.

Figure 3.14 shows the testbench used for electrical-only BER characterization of the wake-up receiver IC. To mimic the current signal (i_s') as will be generated by the transducer during field measurements, a 10 MΩ resistor was used in series with an OOK voltage signal obtained by mixing pseudo-random bits from the FPGA and a 40.6 kHz sine-wave carrier.

A shielded transducer was used in parallel with the matching circuit to obtain impedance levels similar to those in the field measurements. The 250 Hz data clock and the 14 kHz ADC sampling clock were generated using waveform generators and were synchronized using an external loop, though a digital clock recovery loop was later implemented on the FPGA and then tested to estimate the power consumption of the digital back-end in a system implementation.

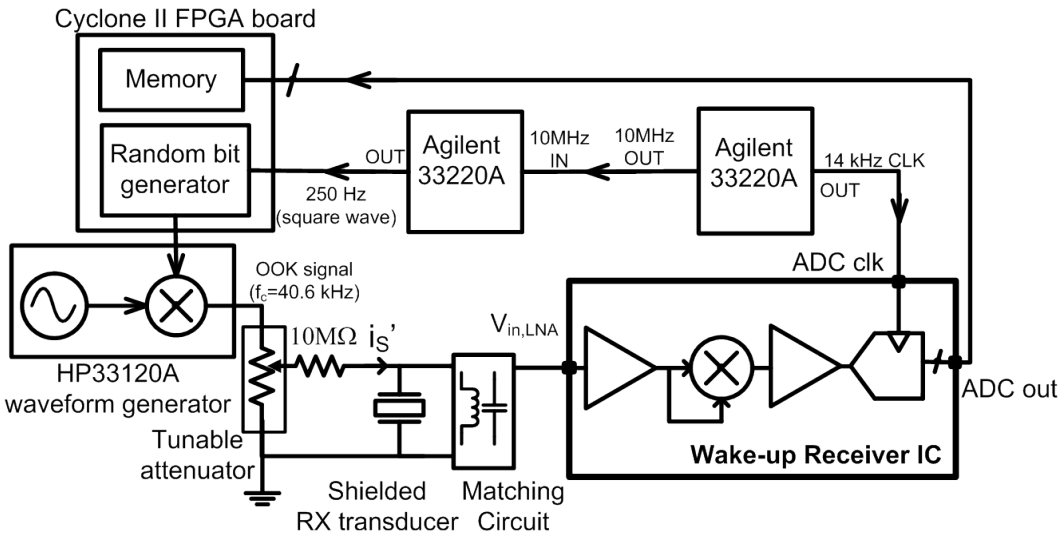

Figure 3.14: Testbench for the electrical-only BER measurements.

To measure the gain of the analog receiver across frequency, an OOK-modulated current signal was applied at the receiver input ($i'_S = 2.25$ nA$_{rms}$) and the baseband output ($v_{in,ADC}$) was measured as the carrier frequency was swept. The measurements were done for different gain settings of the first and the second stage VGAs using bits g[0:1] and g[2:3]. The maximum measured gain (for gain setting 0000) is 56 dB at 40.6 kHz (Fig. 3.15). Since the two VGA stages are identical, similar gains are measured for settings 0001

and 0100, and for 0010 and 1000. The measured receiver bandwidth is 2.6 kHz and is limited by the bandwidth of the matching circuit.[3]

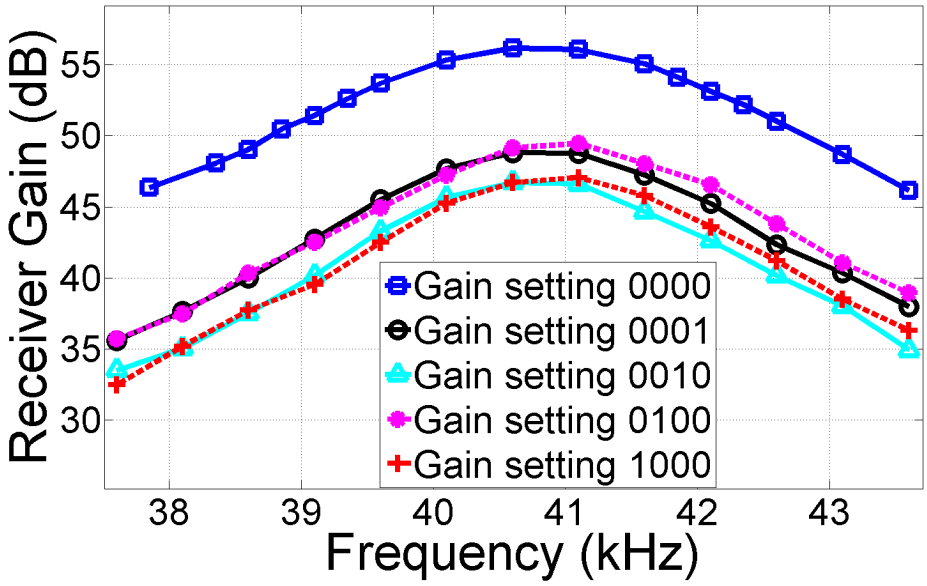

Figure 3.15: Measured receiver gain vs. frequency for different gain settings.

To measure the BER characteristics, the amplitude of the OOK signal at the LNA input ($v_{in,LNA}$) was changed by tuning the attenuator and the corresponding BER values were measured; Fig. 3.16 shows the measured BER curve. At a data rate of 250 bps, the receiver sensitivity (BER=10^{-3}) is 19 μV_{rms} for a receiver power consumption of 4.4 μW. Thus, the targeted receiver sensitivity, as derived in section 3.1.5, was achieved. For higher data rates, filtering from the input matching network resulted in degradation in sensitivity. Table 3.1 summarizes the electrical-only performance of the receiver.

[3]The first version of the system was designed with a transmit transducer [42] which has a bandwidth of 2 kHz. However, because of the lossy dielectric of that transducer, it had to be replaced by the high efficiency transducer [41]. This change came at the expense of substantial reduction in the communication data rates. Hence, a relatively large receiver bandwidth for a data rate of 250 bps.

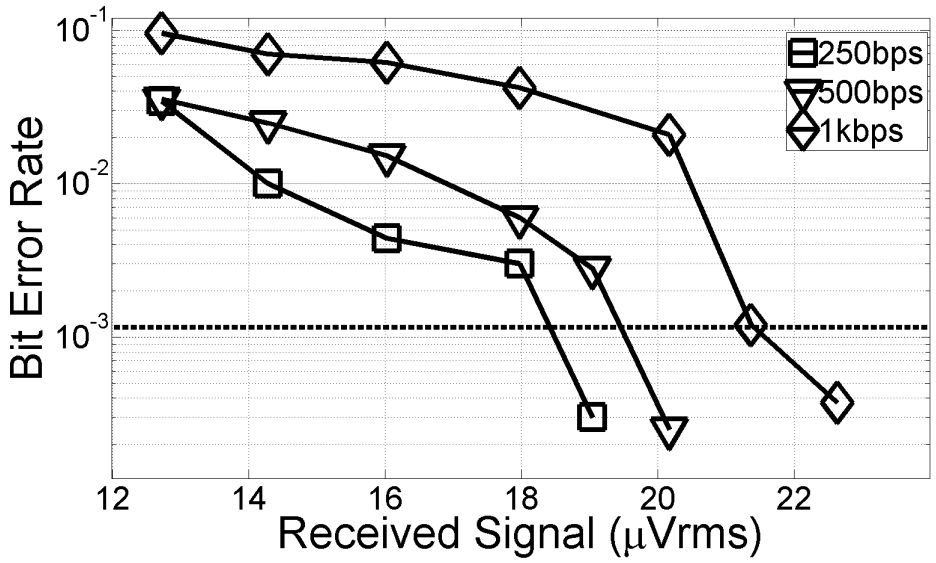

Figure 3.16: BER plots for an electrical input signal.

3.3.2 In-field Measurements for the Ultrasound Data Link

The communication distance range was estimated by combining the electrical-only RX chip BER measurements (Fig. 3.16), the pressure-distance in-field measurements (Fig. 3.5) and the TX-RX pair transmission characteristics (Fig. 3.4). Figure 3.19 shows the estimated distance ranges.

To measure the receiver performance in a real environment, a through-air wireless ultrasound communication system was set up in a lecture hall. The ultrasonic transmitter was constructed with the commercial ultrasonic transmit transducer [41], a cyclone II FPGA to generate transmit data bits, a sine-wave generator, and a discrete mixer. The random bits at a rate of 250 bps are mixed with the 40.6-kHz carrier wave to generate an OOK voltage signal, that excites the transmit transducer.

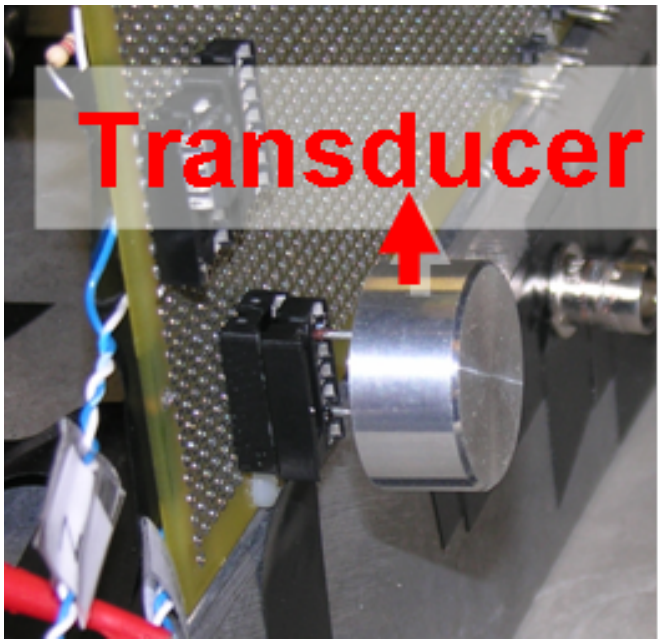

(a)

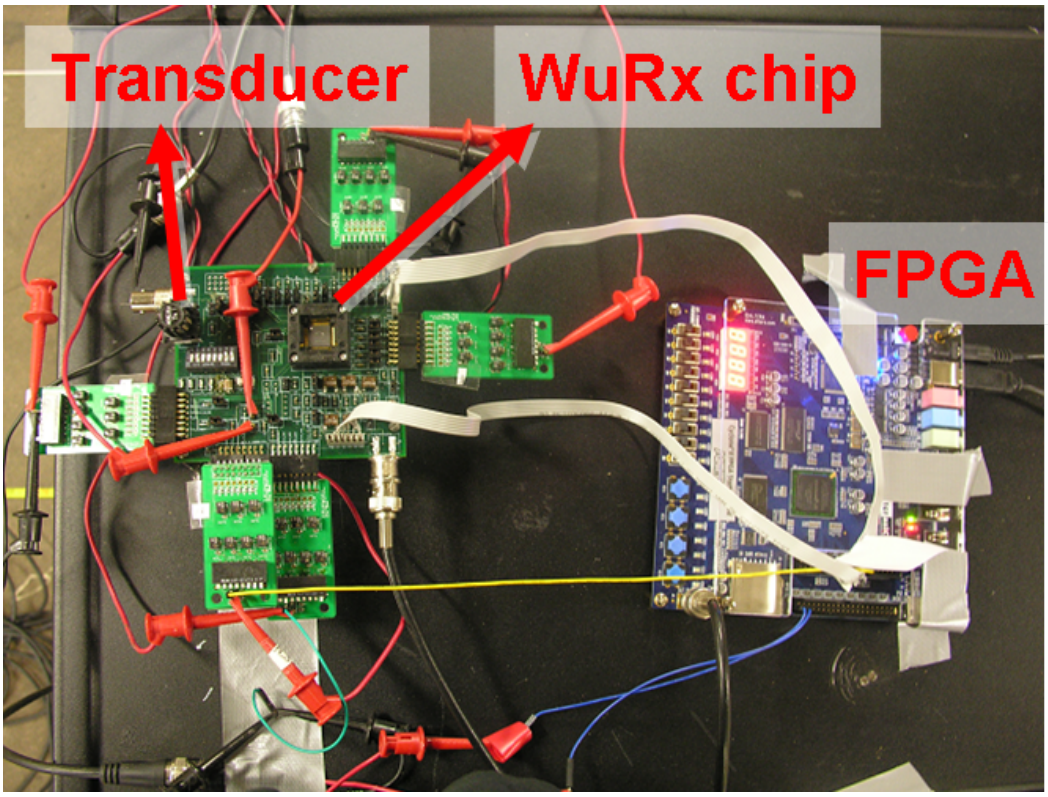

(b)

Figure 3.17: (a) Ultrasonic transmitter for field measurements. (b) Receiver setup consisting of the ultrasonic receiver IC and the FPGA for digital back-end.

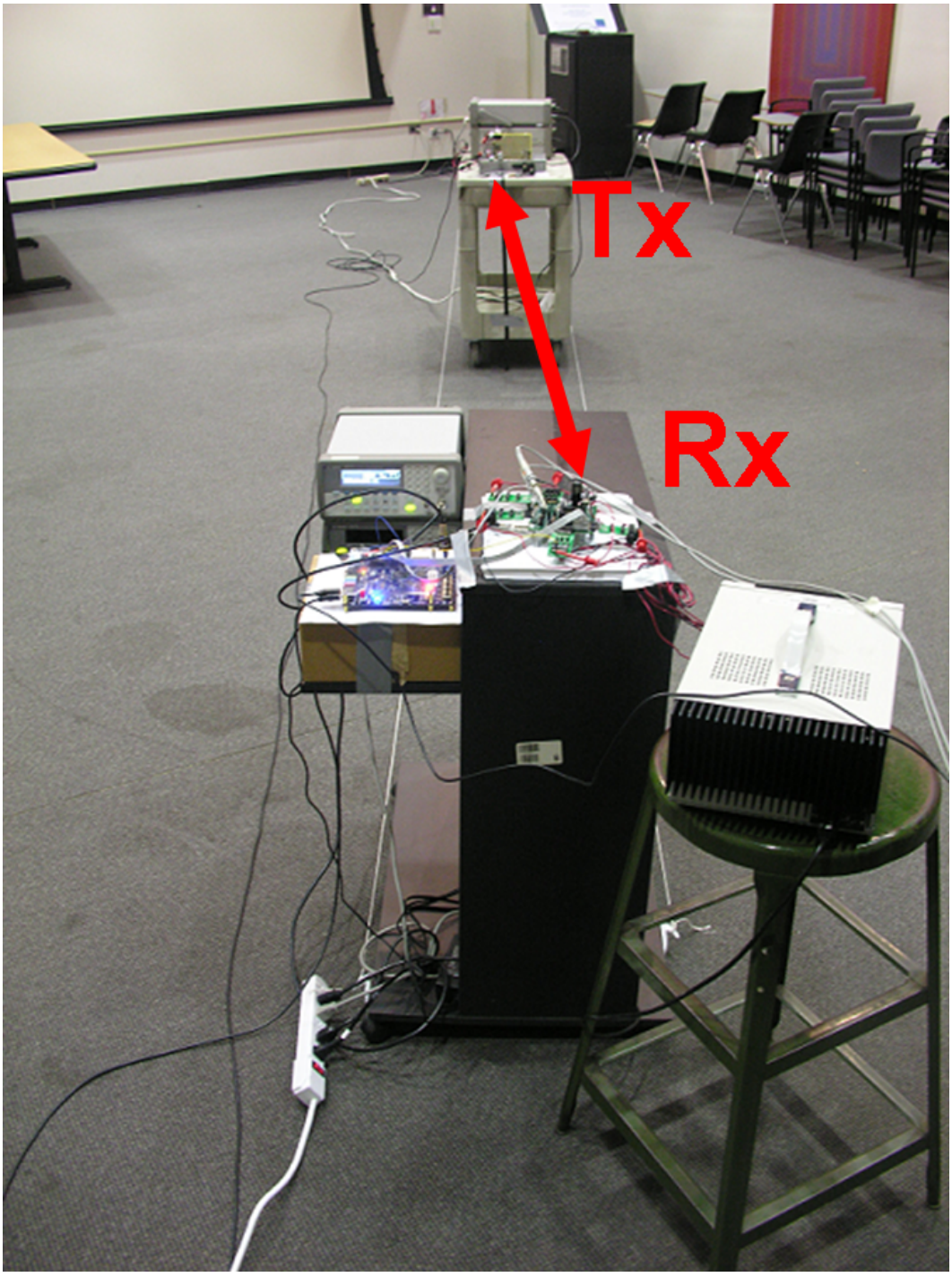

Figure 3.18: Ultrasound communication system, for field measurements, setup in the Interschool Lab at Columbia University.

Table 3.1: Receiver Performance Summary

Ultrasonic Carrier Frequency	40.6 kHz
Modulation	OOK
Supply Voltage	0.6 V
IC Technology	CMOS65nm
Chip area (including bondpads)	1.24 mm^2
Package	QFP64
Power Consumption	
Low Noise Amplifier	1.62 μW
Carrier-band VGA and filter	0.72 μW
Squarer and baseband amplifiers	1 μW
Biasing	0.66 μW
5-bit ADC 2 kS/s	400 nW
Total Receiver	4.4 μW
BER@250bps over 8.6m in free-space (lecture hall) with -18-dBm power into the TX transducer	$<10^{-3}$

For a fixed value of transmit power, the transmitter-receiver distance is changed and the BER values are measured. A BER lower than 10^{-3} could be achieved for a TX-RX distance of 8.6 m, with a transmit power of 16 μW (-18 dBm) and a data rate of 250 bps (Fig. 3.19). The communication distance range matches well with the estimated values. The nature of the measured and the estimated curves are different because the method of esitmating the distance range does not take into account the finite bandwidth of the transducer pair, however it provides a simple and an intuitive approach. The in-field BER was limited by the circuit noise, though some effect of reverberations has also been observed when the receiver was placed near the edges of the room.

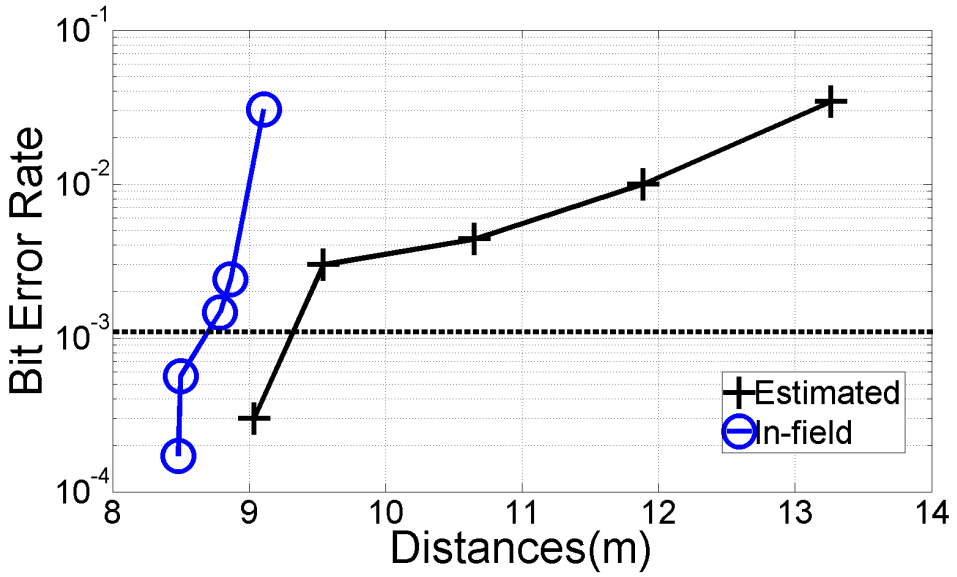

Figure 3.19: The estimated communication distance range obtained by combining the electrical and mechanical characterization curves, and the BER vs. distance curve for a 250 bps random data signal measured in free space in a lecture hall.

3.4 Summary

The chapter presented a 4.4 μW ultrasonic wake-up receiver IC designed in a 65-nm CMOS process. Unlike the duty-cycled main receiver for which the figure-of-merit is energy/bit, the wake-up receiver is always on and the key design criterion is continuous power consumption. Ultrasound enables ultra-low power wake-up by facilitating much lower circuit speeds; the short wavelength of ultrasonic waves enables millimeter-scale transducers even for frequencies as low as a few tens of kilohertz. The 40 kHz ultrasound wake-up receiver IC demonstrated in this research has been electrically characterized and then tested in field. It achieves the communication distance ranges targeted by WSN applications while achieving more than ten-fold reduction in power consumption over the state-of-the-art receivers

(Table 3.2). Additionally, the power being put into the transmitter transducer is approximately 18 dB lower than the typical values used in RF links.

Table 3.2: Performance Comparison

	Carrier	**Transmit Signal Power**	**RX Power Consumption**	**Communication Distance**
[11]	Infra-red (38 kHz)	110 mW	286 μW	10 m[4]
[12]	RF (2 GHz)	1 mW	52 μW	13 m [3]
[13]	RF (2.4 GHz)	1 mW	51 μW	10.5 m [3]
This Work	Ultrasound (40 kHz)	16 μW	4.4 μW	8.6 m[4]

[3] Distances estimated by using a power-distance exponent of 3 as discussed in [46].
[4] These are distances measured in-field.

Chapter 4

Ultrasonic Data Network

4.1 Wake-up Receivers: Performance Parameters and Design Choices

4.1.1 Performance Parameters

On the detection of a wake-up packet, the wake-up receiver turns ON the main receiver to establish a communication link with the transmitting node (or the base station). Noise or interference can result in bit errors at the receiver, because of which the transmitted wake-up packets may not be detected or false wake-ups may occur when none of the nodes actually wants to wake up the receiving node. The performance parameters for the wake-up receivers are as follows:

Probability of Missed Detection (P_{MD}). This is the probability that the wake-up receiver

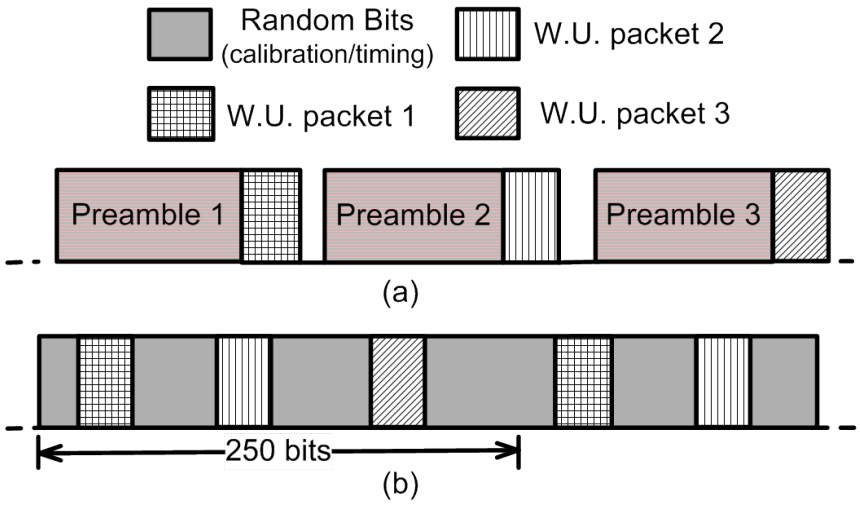

Figure 4.1: (a) Conventionally-used wake-up packet transmission scheme. Each wake-up request is accompanied by a preamble. (b) In this work, thanks to the ultra-low-power operation, bits can be continuously transmitted and receivers can be continuously calibrated, eliminating the need of a separate preamble with each wake-up request.

will not be able to detect a wake-up packet sent by a transmitting node. In case of a missed detection, the transmitter has to re-send the packet, thus increasing the system power consumption. Sometimes, the complementary probability is used, i.e. probability of detection ($P_{detection}$). $P_{MD} = 1 - P_{detection}$.

Number of False Alarms per Intended Wake-up (P_{FA}). A false alarm occurs when the wake-up receiver turns ON the main receiver without any of the nodes intending to communicate with the receiving node. Power is wasted at the receiving node in both the transmission of an acknowledgement and in needless waking up of the main receiver.

4.1.2 Design Choices: Packet Transmission Scheme

In the conventionally-used wake-up packet transmission scheme, the transmitted wake-up packet consists of a preamble and a wake-up pattern (4.1 (a)). The preamble is used by the receiver to adjust its calibration bits and also for synchronization. While the wake-up pattern is used by the receiving node to decide whether it should turn ON the main receiver, it is node-specific and its length depends on the number of nodes in the network. The length of a typical wake-up packet is around 200 bits [47], while that of a wake-up pattern is around 20 bits (explained in detail in section 4.1.3). Thus, in the conventional wake-up packet transmission scheme, the length of the wake-up packet is dominated by the preamble.

In this work, we have used a scheme in which the ultrasonic wake-up transmitter continuously sends out data bits. A wake-up packet is transmitted when a node has to be woken up, and random bits are transmitted when node wake-up is not intended; using these random bits, the always-ON wake-up receiver adjusts its calibration bits continuously (Fig. 4.1 (b)). This way, each time a node has to be woken up, only a wake-up pattern has to be sent. Thus, the latency in the wake-up now depends on the wake-up pattern length only and not on the length of the entire packet. This can result in a very significant decrease in latency, given that the length of the preamble can be as much as ten times that of the wake-up pattern. This packet transmission scheme is especially well suited to wake-up, since the wake-up receiver is always ON and thus its calibration bits can be continuously tuned.

However, it should be noted that this scheme is specific to the proof-of-concept wake-up network implemented here i.e. in a scenario in which there is only one transmitter base station. For an application with node-to-node wake-up, continuous bit transmission by all the transmitting nodes can result in a large number packet collision and for such a case, the conventional packet transmission scheme shown in Fig. 4.1(a) will be better suited.

The probability of false wake-up (P_{FA}) can be reduced further by using bits orthogonal to the wake-up packets for calibration. However, in the implemented design, system performance is limited by P_{MD} (as can be seen from the results in section 4.3) and P_{FA} is not a major concern. Another consideration with this scheme is higher average transmitter power consumption because of continuous transmission. The power consumption of the ultrasonic transmitter used in this research is very low (less than 30 μW) however and thus does not pose any challenges.

Figure 4.1 shows an example data bit structure that was used for continuous bit transmission in field measurements; out of 250 bits sent out by the transmitter in one second, 60 bits are for wake-up (20-bit wake-up packets for the three receivers), while the rest of them are pseudo-random.

4.1.3 Design Choices: Wake-up Decision Threshold and Packet Length

A wake-up event occurs when a pre-defined decision function exceeds a pre-defined threshold value. For the purpose of demonstrating an ultrasonic wake-up, we use an algorithm

for packet detection which consists of matching the received bits with a wake-up pattern unique to each node. Upon the reception of a new bit, the wake-up pattern (length N), stored on each node, is compared with the N-bit combination of the newly received bit and N-1 previous bits. A wake-up event occurs when the number of matching bits goes above a pre-defined threshold. Choosing an appropriate value of decision threshold entails a trade-off between P_{FA} and P_{MD}. A higher-value decision threshold means that more bits must be received correctly for a wake-up event to occur. Thus, a higher decision threshold results in higher P_{MD} and lower P_{FA}, while a lower decision threshold results in lower P_{MD} and higher P_{FA}. We now derive mathematical expressions for both P_{FA} and P_{MD} for the packet transmission scheme shown in Fig. 4.1 (b).

A decision threshold of x for an N bit wake-up pattern means that the wake-up event occurs if, out of N consecutive received bits, more than x received bits match with the wake-up pattern bits. Expression (4.1) gives P_{MD} in terms of the Bit Error Rate (BER), which is the number of bit errors divided by the total number of bits received.

$$P_{MD} = \sum_{i=0}^{x} \binom{N}{i} (1 - BER)^i BER^{N-i} \tag{4.1}$$

$\binom{N}{i}$ is the number of combinations in which i bits, out of a total of N consecutive received bits, can be correctly received. The probability that a combination has i correctly received bits (and that the rest of the $N - i$ bits are erroneous) is given by $(1 -$

$BER)^i BER^{N-i}$. P_{MD} is the sum of all probabilities for which less than $x+1$ bits are received correctly.

A false alarm can occur for either of two reasons: a) some of the calibration/timing bits (Fig. 4.1 (b)) happen to be the same as the wake-up pattern of a node; thus, the transmitted bits meet the wake-up criterion without the transmitter intending to wake up the main channel and without any bit errors at the receiver. b) a wake-up event is caused by the bit errors at the receiver.

In order to gain an intuitive design insight, we make some assumptions. We assume that the P_{FA} is dominated by (a). We further assume that the transmitted bits are random and that the wake-up packets are separated by a large number of bits. In this scenario, P_{FA} is given by (4.2):

$$P_{FA} = \sum_{i=x+1}^{x} \binom{N}{i} (\frac{1}{2})^i (\frac{1}{2})^{N-i} \frac{B.R.}{P.R.} \tag{4.2}$$

where B.R. and P.R. are Bit Rate and Packet Rate respectively. $\binom{N}{i}$ is the number of combinations in which i received bits, out of N consecutive received bits, match with the wake-up pattern bits. $(\frac{1}{2})^i (\frac{1}{2})^{N-i}$ is the probability that i bits, out of a total of N bits, match with the bits of the wake-up pattern. P_{FA} is the sum of the probabilities (for which more than x bits match with the N-bit wake-up pattern) normalized over the wake-up packet rate. As we will see in section 4.3, the P_{FA} values calculated with the above assumptions are much higher than those obtained from the actual measurements. Thus, the design choices made on the basis of the above expressions are quite conservative.

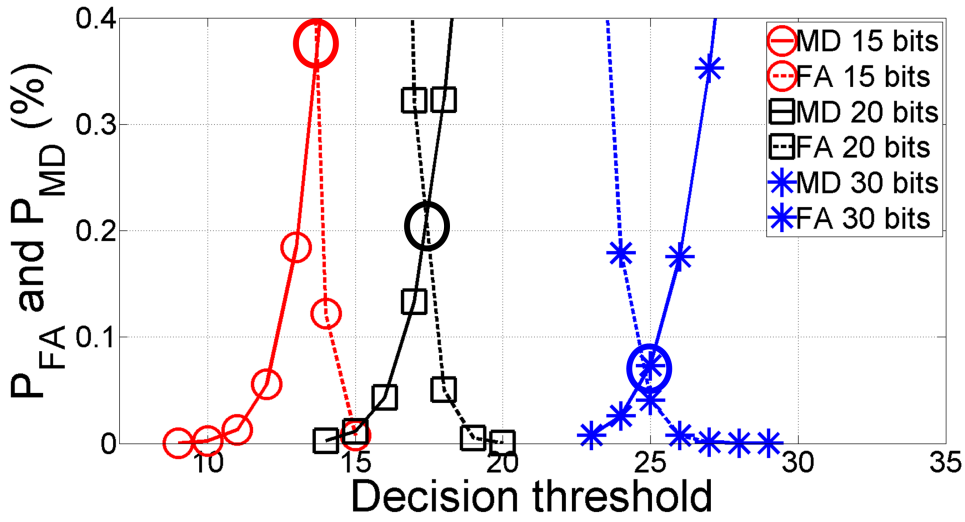

(a)

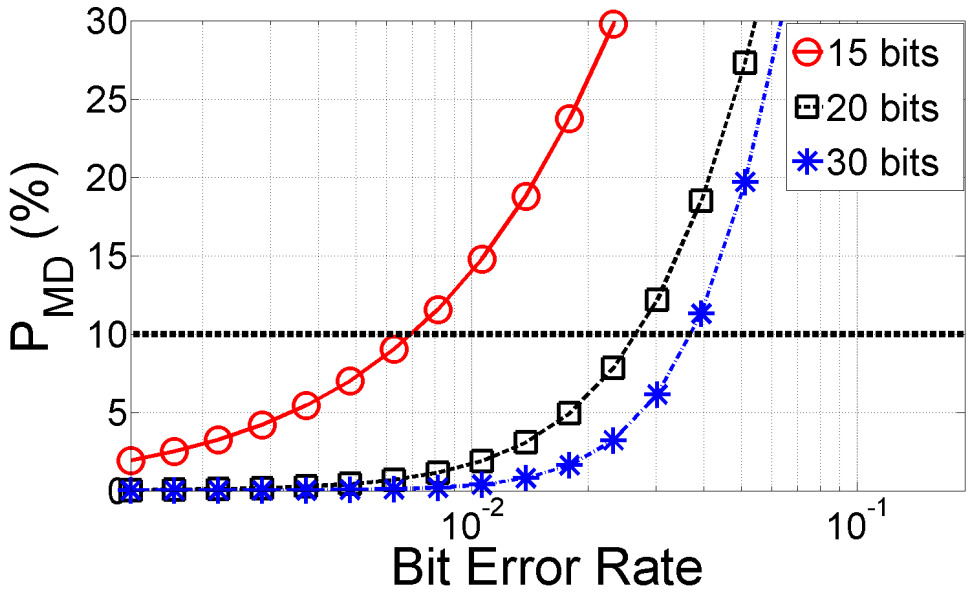

(b)

Figure 4.2: (a) Simulated curves for P_{FA} and P_{MD} (Packet rate=1 pkt/s, Bit Rate=250 bps and BER=0.1) for varying wake-up packet lengths plotted against decision threshold. The optimal values of decision threshold, for each of the packet lengths, are encircled. (b) Simulated P_{MD} vs. BER for different wake-up packet lengths and with optimally chosen decision thresholds.

Each of the plots in Fig. 4.2(a) is a MATLAB simulation showing how P_{MD} and P_{FA} change with decision threshold (for wake-up patterns of length 15, 20 and 30 bits) for a fixed value of bit error rate (BER=0.1). As shown by the solid lines, the probability of missing a packet (P_{MD}) increases with the decision threshold because more bits have to be received correctly for a wake-up event to occur. The dotted lines show that the number of false alarms (P_{FA}) decreases with every increase in the detection threshold.

The net energy wasted because of missed detections and false alarms can be minimized by an optimal design choice of the decision threshold (x). As an example, we minimize the energy for the case where the wastage for a false alarm and for a missed detection is the same. Hence, we minimize the function P_{FA}+ P_{MD} so as to lower the system power wasted because of wake-up errors. In Fig. 4.2(a), the depth of the valley formed by the intersection of P_{FA} and P_{MD} curves increases with the length of the wake-up packet. Thus, for a given value of BER, longer packet lengths enable a lower $P_{FA} + P_{MD}$ optimum. For other possible scenarios, a different function can be minimized, but the general approach presented here can still be used.

For a given packet length, lower BER values enable a lower $P_{FA} + P_{MD}$ optimum. Thus, for a system with poor BER numbers, the wake-up performance parameters can be improved by increasing the packet length. In order to achieve values of P_{MD} and P_{FA} that are both below 0.1, packet length must be greater than 30 bits for a BER value of 0.05, 20 bits for a BER of 0.025 and 15 bits for a BER of 0.005 (Fig. 4.2(b)).

4.2 Ultrasound Communication System Design

In this section, we describe the hardware and the supporting software used in the implementation of the ultrasonic communication system. We also characterize the constituent system blocks, the stand-alone receiver, the ultrasonic transducer pair, and the ultrasonic communication channel.

The main design goals for the receiver are: high input sensitivity for good communication distance range and ultra-low-power consumption to enable nodes with long battery life. While for the transmitter, it is desirable to have high transmit efficiency, so that the system can be realized with low power levels and with excitation voltage levels of a few volts, as supported by modern circuit technologies.

4.2.1 Ultrasonic Transducers

For the proof of concept, we implement an ultrasonic network that consists of of one base station and three network nodes. As explained in section 3.1.3, we have used metal-piezoelectric unimorphs [41] at the transmitter; a combination of three transducers was used for omni-directional transmission (Fig. 4.4). At the receiver, the omni-directional PVDF (Polyvinylidene Fluoride) film [42] has been used.

The characterization results for the transducers have been already been presented in section 3.1.3.

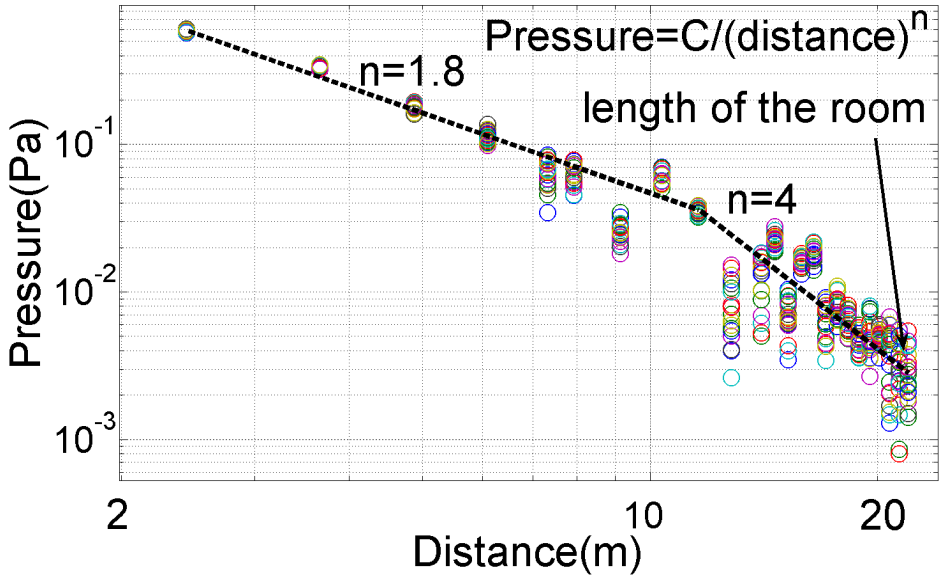

Figure 4.3: Characterization of ultrasound waves through in-field pressure measurements in a car parking garage (TX excitation of 10 $\mathbf{V_{p\text{-}p}}$).

4.2.2 Communication Channel Characterization

To characterize the ultrasound channel, we measured ultrasound pressure vs. distance using commercially available pressure-calibration equipment [45]. Figure 4.3 shows the measurements taken in a car garage. Pressure was observed to have an inverse dependence on distance – $\text{Pressure} \propto 1/(\text{Distance})^n$ – with the exponent n increasing with the TX-RX distance. A sharp degradation in the amplitude of pressure waves is observed for distances greater than 10 m; n is 1.8 for a distance of 5 m, and increases to 4 for a distance of 15 m. These results match closely with those presented in [48]. As a result of this sharp fall in pressure levels, very high TX excitation levels are needed to achieve communication distance ranges of more than 10 m (explained in detail later in section 4.3.1).

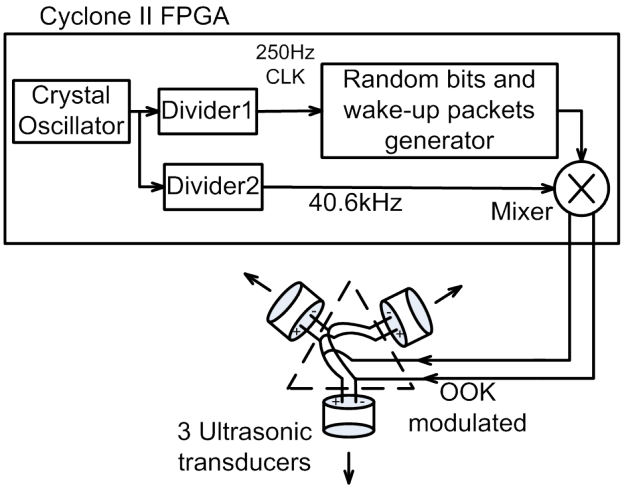

Figure 4.4: Diagram of the transmitter setup. Three ultrasonic transmit transducers were used to achieve omnidirectional transmission.

4.2.3 Receiver Hardware

The wake-up receiver IC, discussed in Chapter 3, was used for field measurements. The digital output of this receiver IC goes into the FPGA, where clock recovery and wake-up pattern detection are implemented. For this proof-of-concept prototype, we have used a commercial FPGA chip to realize the digital back-end because the power consumption of the receiver, in a full system implementation, will be dominated by the analog circuitry (explained in detail later in section 4.2.3). In the final system, the digital circuitry can easily be integrated with the analog receiver as a System on Chip (SoC).

Implementation of the digital back-end

The digital back-end of the receiver was designed in Verilog Hardware Description Language (VHDL) and realized with an FPGA for this proof-of-principle prototype system. It

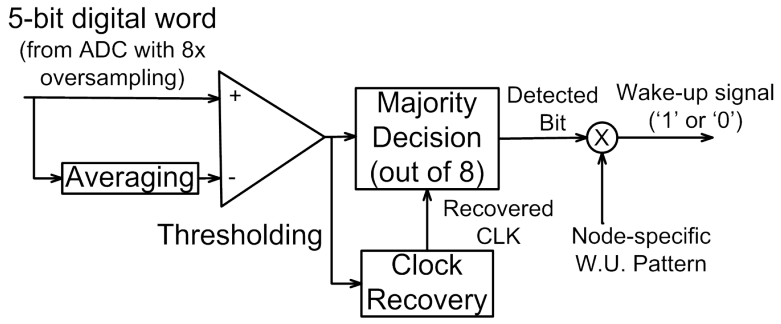

Figure 4.5: Digital backend implemented on a Cyclone II FPGA.

has the following functions (Fig. 4.5): thresholding function to get one bit samples ('1' or '0') from the 5-bit ADC output; a majority decision function to get digital bits from the sampled binary values; and a digital clock recovery circuit to recover the transmit clock from the binary samples. Based on this recovered clock, the receiver decides where to sample the received signal for optimal bit detection. The sampling clock of the ADC, which over-samples the data eight times, is derived from a crystal oscillator.

In this work, we have used early-late clock recovery (Fig. 4.6) to align the receiver clock with the baseband signal (transmitter) clock. First, the phase detector computes the phase difference between the extracted clock and the received baseband signal. It does this by computing the difference between the integrated values of the early (first four samples) and the late accumulators (last four samples) over the duration of one bit (eight samples). The phase difference is then averaged over 8k samples using a digital loop filter and is used to adjust the phase of the extracted clock such that it is in phase with the receiver baseband signal.

In the majority decision block, the samples of the received signal within one time period

of the extracted clock are digitally processed to decide on the value of the received bit (Fig. 4.5), a bit '1' is detected if more than 4 (out of 8) samples are '1'. Finally, the detected bits are compared with a wake-up pattern (unique to each of the three nodes) to determine the presence or absence of a wake-up signal.

The need for digital clock recovery can be mitigated by using self-clocked digital signals. But here we have not used these signals for primarily two reasons. First, the data rates achievable are lower compared to non-clocking digital signals. Second, for this design, the power consumption of digital clock recovery is anyway negligible compared to the analog circuitry and does not contribute significantly to the overall receiver power.

Estimate of the power consumption of a system-on-chip realization

The power expended at the receiver includes the power consumption of the analog receiver, the ADC, a clock generator and the digital back-end. The power consumption of the ultrasonic receiver IC, consisting of the analog receiver and the ADC, is 4.4 μW. Next, we estimate the power consumption of the clock generator and the digital back-end circuitry to estimate the overall power consumption of the receiver for a System on Chip (SoC) implementation.

We estimate the power consumption of the digital back-end based on the complexity of the VHDL implementation. The power consumption of a digital circuit is given by $\alpha C V_{DD}^2 f_{clk}$, where α is the activity factor, C is the total switched capacitance in the circuit, V_{DD} is the circuit supply voltage and f_{clk} is the switching frequency of the digital circuit. We

estimate the number of transistors that will be required for an ASIC implementation of the circuit and then apply the above formula to estimate circuit power consumption. The digital back-end occupies around 4000 combinational functions and 1000 logic registers on the cyclone II FPGA chip. This translates to 107k transistors for an ASIC implementation [49]. For a 65nm CMOS process, assuming minimum sized 2-input gates (Total Width=0.7 μm, Length=65 nm), an activity factor of unity and a clock frequency of 2 kHz (ADC sampling clock), the estimated power consumption of the digital back-end is 15 nW.

For a full system implementation, a clock generator is required; an ultra-low-power 32 kHz crystal oscillator (e.g. Kyoceras ST3215SB operates at 100 nW) may be used. Note that the power consumption estimated above already includes the power expended in the digital circuitry used to generate the clock signal from the crystal oscillator.

Thus, the overall power consumption at the receiver is estimated to be $4.4\ \mu W$ + 100nW + 15 nW = 4.55 μW. This estimated power is limited by the analog front-end IC which we have built and demonstrated to function at the low power. The power consumption of the digital back-end and the clock generator is negligible in comparison.

Form factor of the transmitter and receivers

Both the transmitter and the receivers are stand-alone modules built on separate PCBs. The transmitter PCB used for single TX-RX pair field measurements is shown in Fig. 4.7(a). It has the dimensions of 6.5 cm x 3.9 cm. The cylindrical transmit transducer has a diameter of 2.5 cm and a height of 1.2 cm.

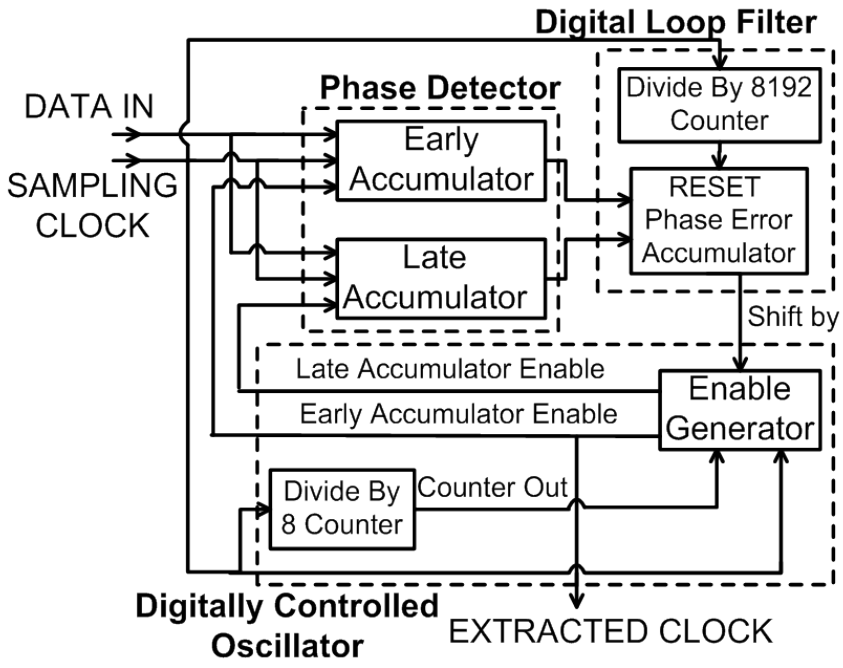

Figure 4.6: Block diagram of the early-late clock recovery implemented on the FPGA.

The receiver PCB used in this work is shown in Fig. 4.7(b). The dimensions of this PCB are 7.3 cm x 5.3 cm. In the full system implementation, both the analog receiver and the digital back-end will be on a system on chip (SoC), thereby eliminating the need for a separate FPGA chip. The receiver size will then be limited by the cylindrical receive transducer, which has a diameter of 1.5 cm and a height of 2.64 cm. Table 4.1 gives a list of the sizes of the receiver components. These dimensions are much smaller compared to the commercial wake-up receivers that use 150 kHz carriers [10] and need bulky magnetic coils that occupy volumes of around 50 cm^3.

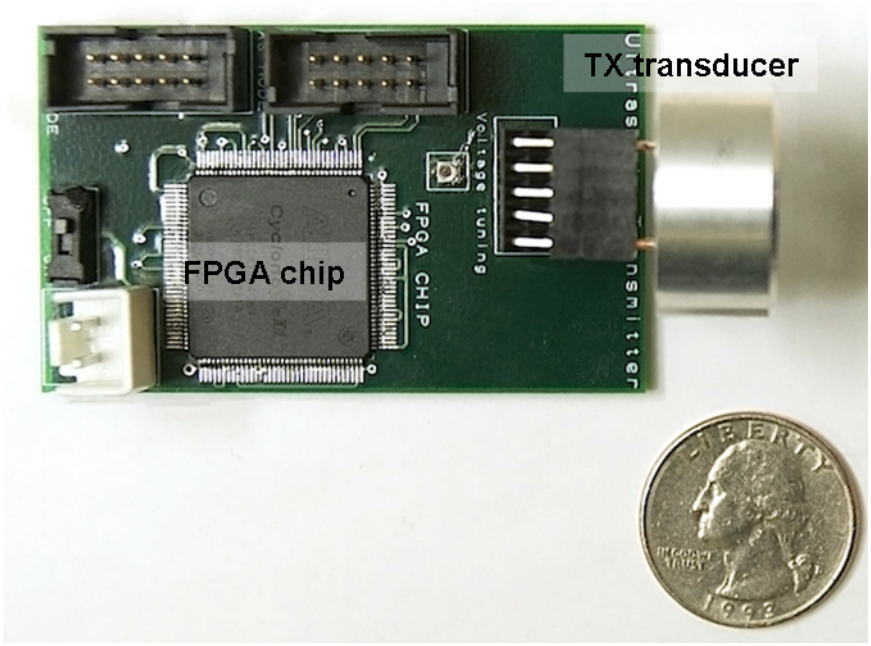

(a)

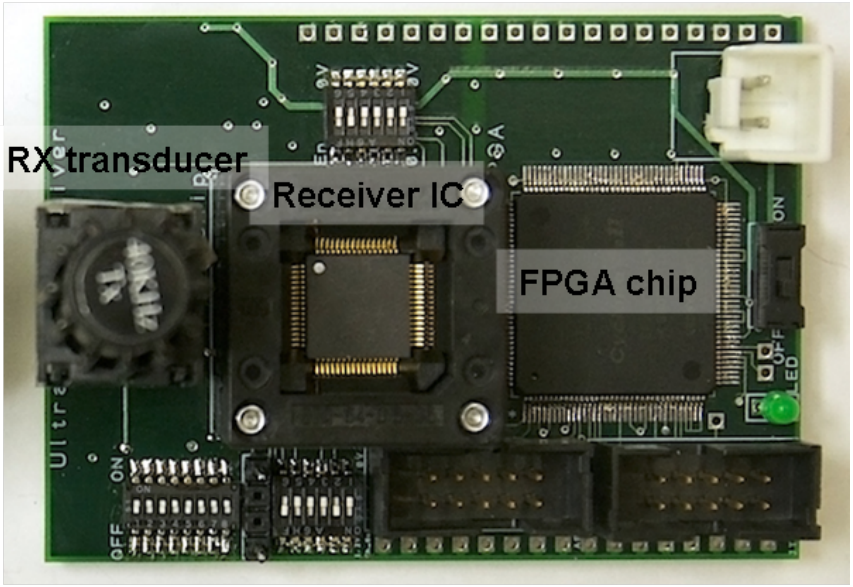

(b)

Figure 4.7: (a) The stand-alone transmitter PCB module used for single TX-RX pair field-measurements. (b) The stand-alone receiver PCB module with the custom designed ultrasonic receiver IC. The pictures are on the same scale.

4.3 Ultrasound Data Link and Network Measurements

To demonstrate ultrasonic wake-up, field measurements were done in two environments: a lecture hall and a car parking garage. In this section, we present ultrasonic network measurements that were done using three receivers and one transmitter. The implemented hardware can be seen as a sub-system of a bigger system which consists of a base station that houses ultrasonic transmitters and network nodes that house ultrasonic wake-up receivers. The wake-up network was set up in a lecture hall that measures 8 m by 11.5 m and can seat more than 70 people. At the time of the measurements, the chairs were present in the room and the rest of the furniture also was in its usual place.

As a precursor to the network measurements, Bit Error Rate vs. Distance measurements for a single TX-RX pair were done in a car parking garage (dimensions of 15 m by 30 m), since it allowed us to test over longer distances. At the time of the measurements, there were cars parked in the vicinity of the setup and the garage was operating normally.

4.3.1 Single Tx-Rx pair field-measurements in a car parking garage

Bit Error Rates were measured for different values of TX-RX distances by using a fixed transmitter excitation (Fig. 4.8). For a data rate of 250 bps, a TX excitation of 200 $mV_{p\text{-}p}$ is sufficient to achieve a distance of 8.6 m. However, to increase the distance range to 18 m, the TX excitation has to be increased to 10 $V_{p\text{-}p}$. This is due to the sharp drop in the pressure levels, with an exponent n of 4, for distances greater than 10 m, as shown in

Table 4.1: Sizes of the receiver components

Receiver Chip	10 mm x 10 mm (QFP package)
Inductor	6.6 mm x 4.5 mm (footprint)
Receive transducer	Height 26.4 mm Diameter 15 mm
Oscillator	5 mm x 3.7 mm (footprint)

Fig. 4.3 and discussed in section 4.2.2. Thus, for communication distances of more than 10m, ultrasound is a challenging communication medium for node-to-node wake-up and its application is limited to cases where the transmitter is powered from a large power source like an electrical outlet.

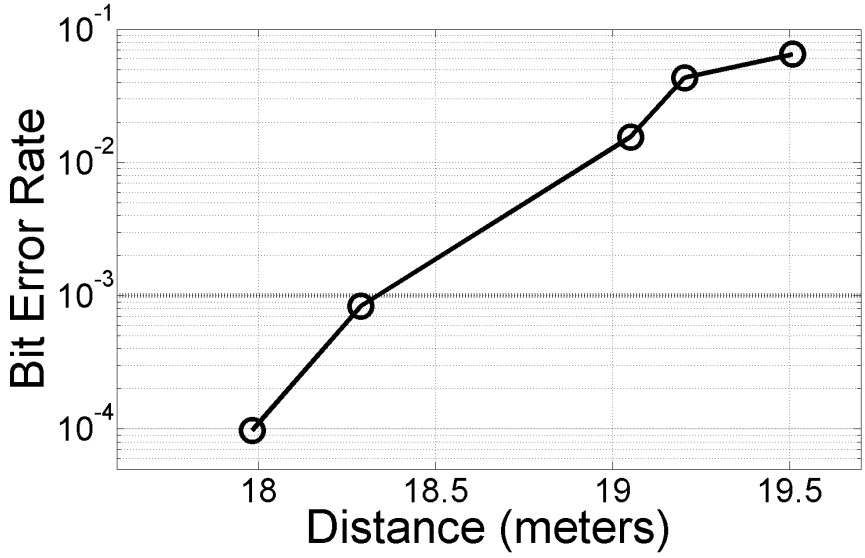

Figure 4.8: In-field Bit Error Rate measurements in the car garage for a single TX-RX pair with a TX excitation of $10V_{p\text{-}p}$. A distance of 18.3 m can be covered with a BER of $10^{-3.}$

4.3.2 Field-measurements in the lecture hall

Two sets of measurements were done in the lecture hall. In the first set, P_{MD} vs. BER measurements were done using a single TX-RX pair to substantiate the theory explained in section 4.1.3. In the second set, P_{MD} was measured for the three receivers of the ultrasonic wake-up network.

P_{MD} vs. Bit Error Rate (BER) Measurements

With a TX-RX distance of 4 m, P_{MD} was measured across BER for wake-up packets of lengths 15, 20 and 30 bits. Decision thresholds (x) are chosen from the simulations shown in figure 4.2(a) in order to achieve optimal values of $P_{FA} + P_{MD}$.

To estimate P_{MD}, the number of transmitted wake-up packets (at a rate of 1pkt/s) is compared against the number of packets detected at the receiver. For a good estimate, measurements are done over a larger number of transmitted packets for lower values of P_{MD}; 512 transmitted packets for P_{MD} less than 10 % and 256 packets otherwise.

Figure 4.9 shows the measured P_{MD} vs. BER values alongside the calculated curves from Fig. 4.2(b). A close match is observed between the calculations and the measurements, thereby substantiating the theory presented in section 4.1.3.

No false alarms were observed for either the 20-bit or the 30-bit wake-ups, while for the 15-bit wake-up, the maximum measured value of P_{FA} was only 1/128. These low P_{FA} values mean that the system's performance is being limited by P_{MD} and that the chosen

decision thresholds are conservative – P_{MD} can be decreased further by choosing a lower value of decision threshold, while still keeping P_{FA} below the targeted value of 10 %.

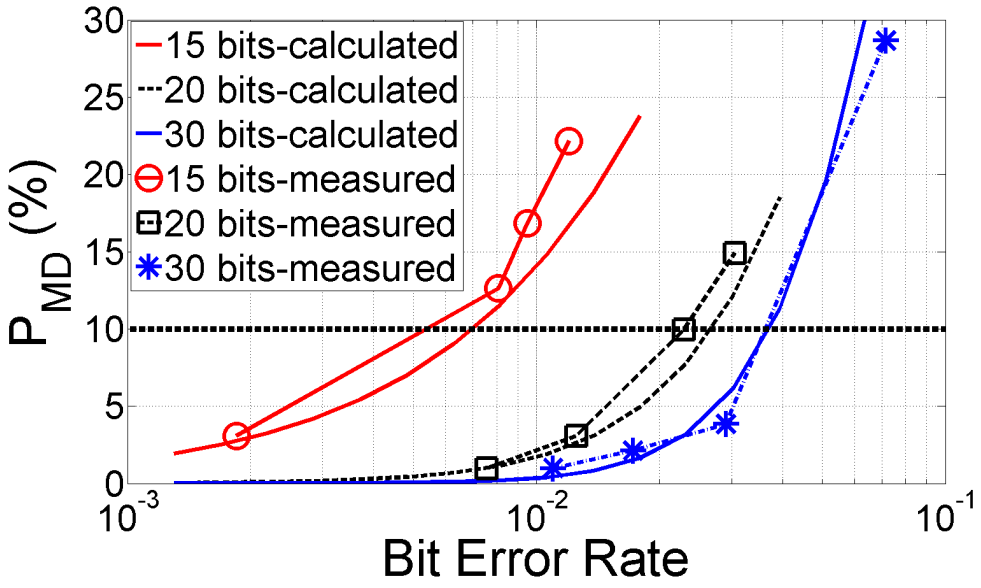

Figure 4.9: Measured P_{MD} vs. BER for different wake-up packet lengths. The measured curves match well with the calculated curves.

Ultrasound Wake-up Network

An ultrasound network, consisting of three receivers and one transmitter, was deployed in the lecture hall. To cover maximum room area, each receiver was kept at a distance of 4 m from the transmitter. At the transmitter, three transducers were used for omnidirectional transmission (Fig. 4.4).

To measure the minimum transmit power needed to achieve a P_{MD} of less than 10 %, transmit power is swept and P_{MD} is measured over 2,048 received wake-up packets at the

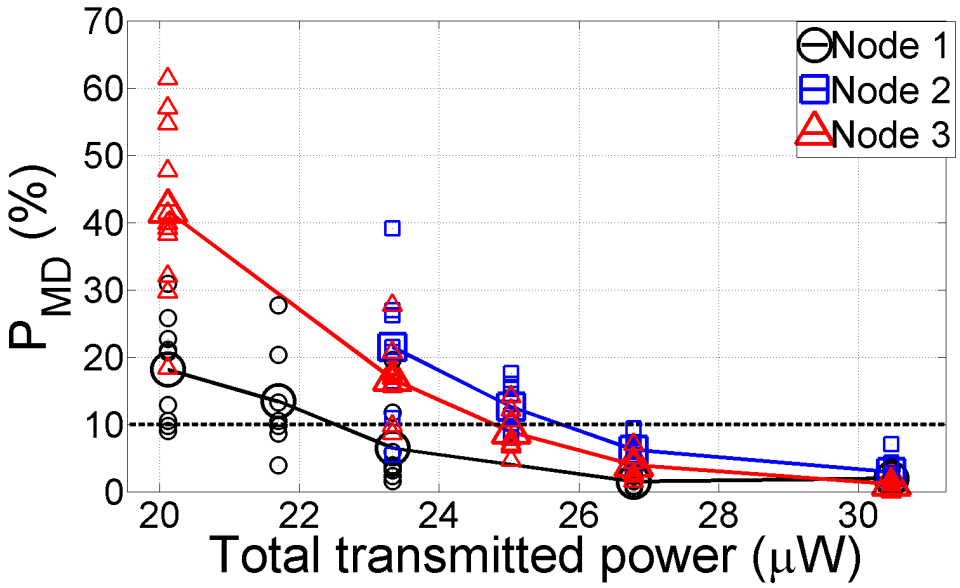

Figure 4.10: P_{MD} values are measured at the three receivers of the ultrasonic data network, as the transmit power is swept. For transmitted power of more than 27 μW, P_{MD} is less than 10 % at all the three receivers.

three receivers. A wake-up packet of length 20 bits is used with a decision threshold of 18 bits.

The measured values are shown by bigger symbols in Fig. 4.10. For a P_{MD} to be less than 10 % at receivers 1, 2 and 3, the transmit power must be more than 23 μW, 27 μW and 25 μW respectively; the difference in values is because of mismatch in the properties of the ultrasonic transducers at the three receiver setups. The power consumption of each receiver IC is 4.4 μW.

P_{MD} measurements are also done over smaller sets of 256 transmitted wake-up packets, shown by smaller symbols in the plot; the observed variation in the values is because of reflections. However, for measurements taken over a larger number of wake-up packets,

the effects of reflections average out; this can be seen from the monotonically decreasing nature of P_{MD} curve obtained by joining the measurement points corresponding to 2,048 received wake-up packets.

The above results were compared with theoretical estimates obtained by combining the characterization curves for the electrical and the mechanical parts of the communication system. Transmission characteristics of the TX-RX pair (Fig. 3.4), the measured received pressure levels at the three receivers, the Receiver IC's BER vs. input voltage curve (Fig. 3.16) and the P_{MD} vs. BER curve (Fig. 4.9), were all combined to predict the values of the transmit power needed to achieve the required P_{MD}. The measurement results matched closely with the predicted values.

4.4 Challenges in Ultrasound Data Communication

In this paragraph we discuss a number of remaining challenges of using ultrasound for data communications and wake-up beyond what we demonstrate in this paper and how they will be addressed in future work.

Communication Distance Range. Ultrasound-based systems proposed in the present literature can achieve a distance range of only a few meters. In comparison, the system presented in this paper achieves a much higher communication distance range of 18 m because of the high sensitivity of the custom designed ultrasonic receiver IC. The range can be further extended by using higher sensitivity receive transducers. Another way to

extend the communication distance range is by using multi-hop, which has already been used for ultrasound, but for the purpose of widening the angular coverage of the transducers [50], [51].

In indoor environments, the propagation of ultrasound is very similar to sound and is limited by physical obstacles like walls of the room. By coupling the ultrasound source into the solids, the propagation range of ultrasound can be extended. The losses in the solid objects depends on the absorption characteristics and are usually very low.

Directionality. In previous research, several methodologies have been used to achieve omnidirectional performance using ultrasonic transducers. In [52], an inverted cone-shaped ultrasonic reflector was used for omnidirectional transmission and reception. Reference [27] used six transducers arranged along a hexagon and in [28], four transmit and four receive transducers were used. In the cricket location support system [26], the transmit transducer was aligned at 45 degrees from the horizontal plane, facing the location that is to be covered.

The receive and the transmit transducers used in this research can tolerate misalignment without any significant reduction in the signal strength. In the horizontal plane, the receive transducer is omnidirectional and in the vertical plane it has a beam angle of +/-60 degrees for a signal strength degradation of 15 dB. The transmit transducer is hemispherical (180 degrees) in both the vertical and the horizontal planes, other than two small dead-bands (approx. 5 degrees wide, on each side of the 0 degree axis). This means that for a TX-RX distance of 4 m, the horizontal planes of the transmit and the receive transducers would have

to be vertically displaced by more than 1 m for the signal strength to drop by 50 % (6 dB) of the maximum value. For larger TX-RX distances, even larger vertical displacements can be tolerated. For the experimental setup presented in section 4.3.2, the horizontal planes of the transmit and the receive transducers were aligned.

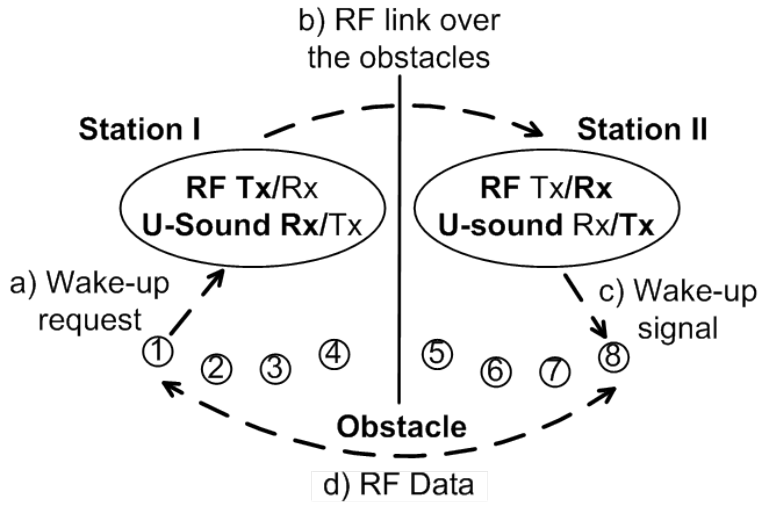

Figure 4.11: Ultrasound wake-up for nodes separated by a physical obstacle. RF is used for communication over the obstacles and low-power ultrasonic communication is used for node wake-up to enable nodes with long battery lifetimes.

Interference and Reverberations. Reverberations can cause multiple copies of the signal to arrive at the receiver. This causes inter-symbol interference which can degrade the receiver performance and result in bit errors. In [48], the author discusses the design of ultrasound-based indoor positioning systems and estimates the reverberation times of 50 ms to 200 ms for typical indoor environments. Bass [51] estimates the ultrasonic noise in industrial operations like cutting, grinding, drilling and spraying, can result in signifi-

cant ultrasonic noise. For other environments like homes, offices, and hospitals no data is available in open literature, but ultrasonic noise is expected to be significantly lower.

For the wake-up receiver IC presented in this thesis, the narrow input bandwidth (2 kHz) of the receiver limits the background noise entering the system. All the field measurements have been done in real-life environments which included typical interferers and reflectors. As discussed in section 4.3, some effects of reflections were observed in the form of fluctuations in the packet error rates.

Communication Data Rate. The data rates used in this work are low (at 250 bps), however for the targeted applications of environmental, HVAC or surveillance, these data rates suffice. But, the applications of this work can be further extended by increasing the communication data rates. This can be accomplished by using custom transducers designed for higher bandwidth than the commercially available transducers.

Latency. Unlike data packets, the length of the wake-up packets is small and thus the limited data rates achievable via ultrasound are not a primary concern. Moreover, using the continuous packet transmission scheme implemented in this paper (discussed in section 4.1.2), the wake-up packet needs to contain only the node address and is thus short in length (around 20 bits). It is noteworthy that the sensor networks envisioned to benefit from ultrasound wake-up are the ones that will be vigilant for long periods, but will be sleeping for most of the time. Battery life for such networks is important, but the long idle times mean that latency can be tolerated. Examples of such networks include surveillance,

monitoring and HVAC sensors; typical packet rates for these applications are only 1pkt/min or so.

Extension to Non-line-of-sight Situations. Ultrasound is being used in combination with RF as a part of the commercial Real Time Location Systems (RTLS) used in health-care [53], [54]. For such applications, the line-of-sight requirement of ultrasound is an asset because it offers containment and helps achieve high location accuracy. Wherever possible, ultrasound is desirable because of its superior tracking accuracy, while RF is used for location in environments where line-of-sight is not available. Similarly, the combined use of the two technologies can be extended to wake-up for wireless sensor nodes.

In sensor network environments where the line-of-sight requirement of ultrasound presents a challenge, local base stations (consisting of ultrasound and RF transceivers) may be used, one corresponding to each physical partition (Fig. 4.11). When a link has to be established between two nodes separated by an obstacle, the initiating node (node 1) sends the wake-up request to a local base station (Station I) using ultrasound. The request is then sent, using an RF signal, to the local base station (Station II) that corresponds to the node for which the wake-up is intended (node 8). The station II then sends the ultrasonic wake-up signal to the node which is to be woken up. Then, the RF-based main data link is established between the two nodes. Thus, the RF channel is used for main data communication and for communication between the base stations, while the ultrasound channel is used for local wake-up. By using this methodology, the benefits of both modes of communication, radio and ultrasound, are exploited. The battery life of the sensor nodes is extended because

of the low-power wake-up that is facilitated by using ultrasound and the system is able to communicate in non-line-of-sight mode because of RF.

4.5 Summary

In this chapter, an ultrasound-based wake-up receiver was in-field tested by setting up an ultrasonic data network, consisting of three receivers and one transmitter, in a lecture hall. More than 90% of the transmitted wake-up packets, at 1 pkt/s, could be detected at each of the three receivers for a transmit power of $27\mu W$ and with a receiver power consumption of 4.4μW.

The data rates used in this work are low (at 250bps), however for many applications like environmental, HVAC or surveillance, where typical packet rates are 1pkt/minute or so, these data rates suffice. But, the applications of this work can be further extended by increasing the communication data rates. This can be accomplished by using custom designed transducers with higher bandwidth than the commercially available transducers, as we discuss in the next chapter.

Chapter 5

Ultrasonic Transducer Design

In the ultrasonic communication systems presented in chapters 3 and 4, communication data rates of only 250 bps could be achieved because of the limited bandwidth of the transmit transducer [41]. Most of the commercially available ultrasonic transducers are built for ranging; in comparison, the performance requirements for the data communication application targeted here are very different. In this chapter, we present electromechanical simulations, done with a computer model of the transducer, to understand the design trade-offs involved in increasing the transmit transducer bandwidth. We also propose transducer dimensions to achieve bandwidths of more than 1 kHz.

5.1 Electromechanical Parameters of Piezoelectric Materials

Piezoelectric materials have the property of converting electrical energy into mechanical energy and vice-versa, and are widely used in ultrasonic transducers. The transducer can operate in transmit or receive mode. In the transmit mode, an electrical voltage is applied across the piezoelectric and it transmits pressure in the surrounding medium. On the other hand, in the receive mode, the mechanical force applied to the material and an electrical voltage is developed across it.

Consider the piezoelectric cube in Fig. 5.1. The three axes of the piezoelectric material are shown alongside the figure. A transducer operates in different modes depending on the directions of the mechanical motion and the applied electric field. For example, in the transverse mode (Fig. 5.1), the applied force (or motion) is along the length of the film and the induced voltage (or the applied electrical voltage) is across the thickness of the film. The corresponding piezoelectric constant is denoted by d_{31}; the first subscript is for the direction of applied electric field and second for the direction of motion. Similarly, the piezoelectric constant for the thickness mode is denoted by d_{33}, as both the applied electric field and the motion are along the film thickness. The transducers used in this work operate in transverse mode.

The equations relating the electrical and mechanical parameters of the piezoelectric material in the transverse mode are given below [43]:

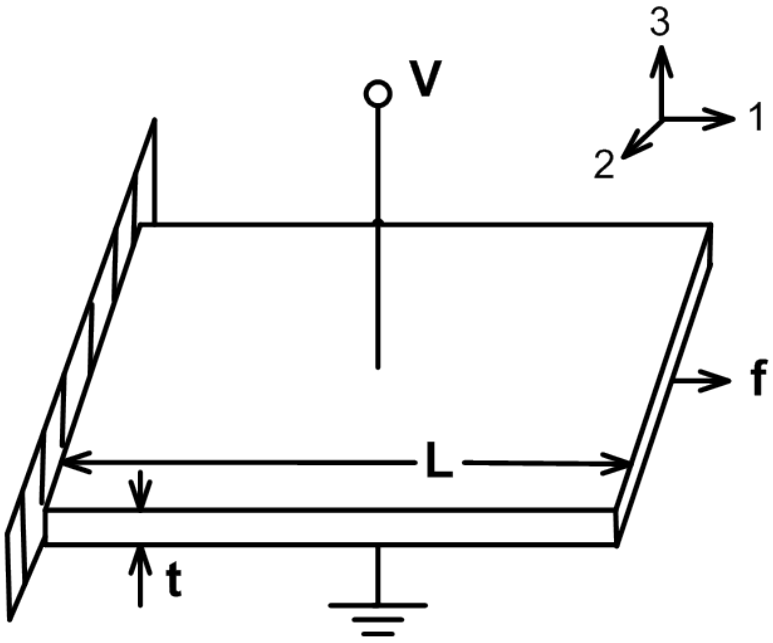

Figure 5.1: A piezoelectric film in transverse mode (d_{31}).

$$D = \epsilon^X E_3 + d_{31} X_1 \tag{5.1}$$

$$x_1 = d_{31} E + \frac{1}{c^E} X_1 \tag{5.2}$$

where D is the electric displacement, E(=V/t) is the electric field, x_1(=$\Delta L/L$) is the strain along the length of the material and X_1(=f/area) is the stress developed because of force applied in direction 1. ϵ^X is the permittivity of the film measured with material under constant stress, d_{31} is the piezoelectric constant and c^E is the stiffness of the material under constant electric field.

As can be observed from these equations, the mechanical properties of the piezoelectric materials depend on the electrical conditions and vice-versa. For example, the ratio of the

values of the permittivity when the material is clamped along its length to when it is free, is given by:

$$\frac{\epsilon_{clamped}(x_1 = 0)}{\epsilon_{free}(X_1 = 0)} = 1 - {k_5}^2 \tag{5.3}$$

where:

$${k_5}^2 = \frac{{d_{31}}^2 c^E}{\epsilon^X} \tag{5.4}$$

Similarly, the ratio for stiffness constant is:

$$\frac{c(E = 0)}{c(D = 0)} = 1 - {k_5}^2 \tag{5.5}$$

${k_5}^2$ is the electromechanical constant and is the ratio of applied electrical energy(mechanical) converted into mechanical(electrical) energy and has a values of 0.02 and 0.11 for two of the most commonly used piezoelectric materials, PVDF (Polyvinylidene fluoride) and PZT (Lead zirconate titanate).

Other than the conversion efficiency, there are many other criteria that have to be considered while deciding on which transducer material to use [43]:

• **Power-to-volume ratio.** It is desirable for a piezoelectric material to have a large power-to-volume ratio. Despite its lower conversion efficiency, PVDF can achieve higher power density compared to PZT owing to its ability to withstand higher electric field.

• **Acoustic impedance.** For the piezoelectric material to transfer energy efficiently to the medium, it is desirable to use a piezoelectric whose impedance is close to that of

the medium. For example, air and water have acoustic impedances of 400 Rayls and 1.5 MRayls, which are both closer to the impedance of the PVDF (4 MRayls) than that of the PZT (33 MRayls). Thus, for operation in air and water, all other factors being equal, PVDF would be a better choice.

• **Operating temperatures.** PZT can operate at much higher temperatures compared to PVDF, which can work only for applications with temperatures below 70^{o}C

• **Construction methods.** The choice of the material also depends on the physical properties. For example, PZT ceramic is better suited than PVDF for many high efficiency structures like the unimorph transducers, which will be discussed in detail later in this chapter. This is because the PZT ceramic can be easily mechanically coupled to metals like aluminum, as required in an unimorph transducer.

Table 5.1 summarizes the above factors.

Table 5.1: PZT vs. PVDF

	PZT	**PVDF**
Electromechanical Coupling factor (${k_{31}}^2$)	0.11	0.02
Max. operating electric field	0.3V/μm	30V/μm
Acoustic match with air (400 Rayls)	33 MRayls	4 MRayls
Temperature	Higher	70^{o}C

5.2 Receive Transducer Electromechanical Model

An ultrasonic transducer consisting of a piezoelectric PVDF film wrapped around a hollow plastic cylinder has been used at the receiver (Fig. 5.2) [42]. The transducer operates

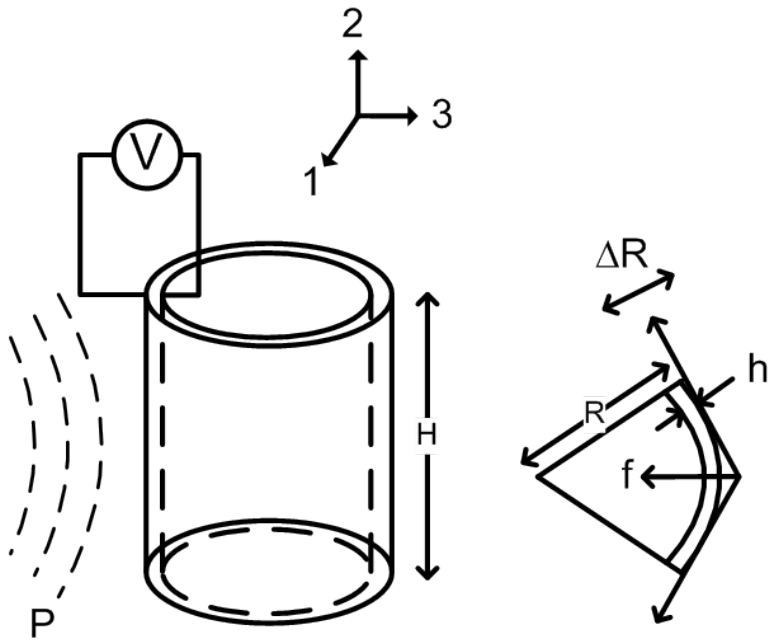

Figure 5.2: Cylindrical PVDF film transducer used at the receiver.

in the breathing mode; the pressure waves incident on the material cause the length of the piezoelectric material to change, the radius of the cylinder expands and contracts, and an electrical signal is developed because of the piezoelectricity of the PVDF. Under the condition of open-circuit at the receiver, D=0 and the equation 5.1 reduces to:

$$E = -\frac{d_{31}}{\epsilon^X} X_1 \tag{5.6}$$

Combining the above equation with equation 5.2, we get:

$$X_1 = x_1 \frac{c^E}{1 - {k_5}^2} \tag{5.7}$$

The stress (X_1) developed results in accleration of the material film:

$$2\pi RH(P) - 2\pi Ht(X_1) = -M\frac{\partial^2 R}{\partial^2 t} \tag{5.8}$$

where R and H are the radius and height of the cylinder, and P is the incident pressure.

Combining the above two equations, substituting $-\Delta R/R$ for x_1, and expressing the mass of the film in terms of material density (ρ) and film dimensions, we derive:

$$\rho(2\pi RHt)\frac{\partial^2 R}{\partial^2 t} = 2\pi Ht(\frac{-\Delta R}{R})\frac{c^E}{1-{k_5}^2} - 2\pi RH(P) \tag{5.9}$$

$$\frac{\partial^2 R}{\partial^2 t} + \frac{\Delta R}{R^2}\frac{c^E}{\rho(1-{k_5}^2)} = -\frac{P}{\rho t} \tag{5.10}$$

Thus, the resonant frequency (f_r) of the transducer, under the condition of electrical open, may be expressed as [55]:

$$f_r = \frac{1}{2\pi R}\sqrt{\frac{c^E}{\rho(1-{k_5}^2)}} \tag{5.11}$$

This is the frequency at which the receive transducer, if excited mechanically, will give out maximum electrical signal.

5.2.1 Effect of the Matching Circuit on the Receive Transducer Characteristics

The stiffness of the piezoelectric material when electrically open is $\frac{c^E}{1-{k_5}^2}$, while the stiffness when electrically short is c^E; combining this information with the expression for resonant frequency under the condition of open circuit (5.11), we can interpret that the resonant frequency when the transducer terminals are shorted is given by $\frac{1}{2\pi R}\sqrt{\frac{c^E}{\rho}}$. Thus, for a PVDF film (${k_5}^2$=.02), the difference between the two termination conditions is only 1%. Therefore, in the design of the front-end for the best possible receiver performance (presented in section 3.1.4), the effect of the matching circuit on transducer's characteristics has been ignored.

5.3 Transmit Transducer Design

A piezoelectric unimorph transducer, consisting of circular piezoceramic (PZT) and aluminum plates, has been used at the transmitter because of its high transmit efficiency [41] (Fig.5.3). The voltage applied across the PZT plate results in a change in its length; as a result, motion is induced in the composite plate because of difference in the piezoelectric constants (d_{31}) of the two materials.

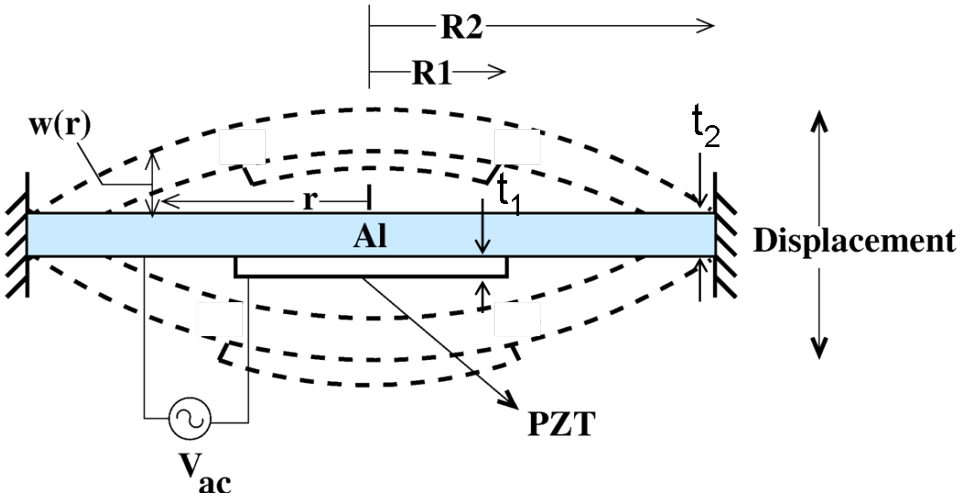

Figure 5.3: Transmit transducer consisting of the PZT piezoelectric film bonded to an Al disk.

5.3.1 Transmit Transducer Electromechanical Model

In most electromechanical system models, differential pressure and voltage are the effort variables, while current and volumetric flow rate are the flow variables. The linearized system equations are:

$$\begin{bmatrix} \Delta Vol. \\ q \end{bmatrix} = \begin{bmatrix} C_{AS} & d_A \\ d_A & C_{EF} \end{bmatrix} \begin{bmatrix} P \\ V_{ac} \end{bmatrix} \tag{5.12}$$

where $\Delta Vol.$ is the volume displaced by the composite plate, P is the differential pressure, V_{ac} is the voltage across the piezoelectric, q is the charge on the piezoelectric, C_{EF} is the electrical capacitance when P=0, C_{AS} is the acoustic compliance with two sides of the piezoelectric disk shorted and d_A is the effective piezoelectric coefficient of the transducer. Following are the expressions for these quantities:

$$\Delta Vol. = \int_0^{R2} 2\pi r w(r) dr \tag{5.13}$$

$$C_{EF} = \frac{\epsilon_r \epsilon_o \pi {R_1}^2}{t_1} \tag{5.14}$$

$$C_{AS} = \left. \frac{\Delta Vol.}{P} \right|_{V_{ac}=0} \tag{5.15}$$

$$d_A = \left. \frac{\Delta Vol.}{V_{ac}} \right|_{P=0} \tag{5.16}$$

For sinusoidal voltage excitation, the matrix in equation 5.12 reduces to:

$$\begin{bmatrix} Q \\ i \end{bmatrix} = \begin{bmatrix} j\omega C_{AS} & j\omega d_A \\ j\omega d_A & j\omega C_{EF} \end{bmatrix} \begin{bmatrix} P \\ V_{ac} \end{bmatrix} \tag{5.17}$$

where i is the current and Q is the rate of change of the volume swept by the transducer plate. Based on the above matrix, we draw an equivalent circuit (Fig. 5.5) to model the electroacoustic behavior of the system. On the left hand side of the circuit are the electrical variables – current and voltage, and on the right hand side are the mechanical variables – pressure and rate of change of volume swept by the transducer. The transformer ratio, ϕ, gives the transduction coefficient:

$$\phi = -\frac{d_A}{C_{AS}} \tag{5.18}$$

To include the inertial effects of the two disks, we add M_{AS} to the transducer model in

equation 5.12:

$$M_{AS} = \int_0^{R2} \rho_A(r) 2\pi r dr (\frac{w(r)}{\Delta Vol.})^2 \tag{5.19}$$

5.3.2 Analogous Electrical and Mechanical Systems

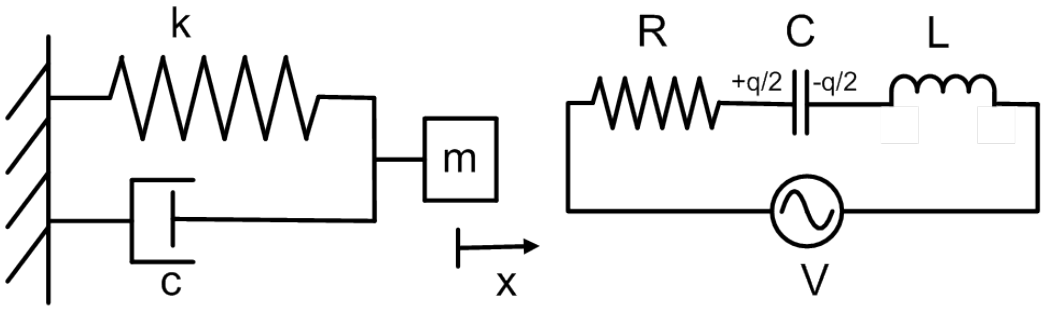

Figure 5.4: (a) A typical spring-mass system, and (b) an LCR electrical circuit.

Before presenting a detailed description of the transmit transducer equivalent circuit, we analogize mechanical systems to the more widely understood electrical systems. For this purpose, consider the typical spring-mass system (Fig. 5.4(a)) that can be modeled with the generic second order differential equation:

$$m\frac{d^2x}{dt^2} + c\frac{dx}{dt} + kx = F \tag{5.20}$$

where the term m models inertial effects, k is the spring coefficient or elastic constant and c is the damping coefficient; for Rayleigh damping, as used in this work, c is directly

proportional to material stiffness.

$$c = \beta_{dK} k \tag{5.21}$$

This mechanical system is analogous to the series LCR circuit (Fig. 5.4(b)), which can be represented by the second-order equation:

$$L\frac{d^2q}{dt^2} + R\frac{dq}{dt} + \frac{\mathrm{q}}{\mathrm{C}} = V \tag{5.22}$$

Table 5.2 lists the analogies between electrical system and mechanical systems.

Table 5.2: Analogies between electrical and mechanical systems

Mechanical	**Electrical**	**Equation(s)**
Force(F)	Voltage(V)	F=m$\frac{d^2x}{dt^2}$, V=L$\frac{d^2q}{dt^2}$
Mass(M)	Inductor(L)	
Velocity	Current(i)	
Strain(x)	Charge(q)	x=$\frac{F}{k}$, q=CV
Stiffness constant(k)	Capacitance(C)	k $\equiv \frac{1}{C}$
Damping Coefficient(c)	Resistance(R)	

5.3.3 Equivalent Circuit

From the equivalent circuit for the transmit transducer (Fig. 5.5), we can see that for a transducer operating in the transmit mode, the current going into the transducer for a voltage excitation, V_{ac}, at the resonance frequency is:

$$i = \frac{d_A}{C_{AS}} Q + j\omega C_{EF} V_{ac} (1 - \frac{{d_A}^2}{C_{AS} C_{EF}}) \tag{5.23}$$

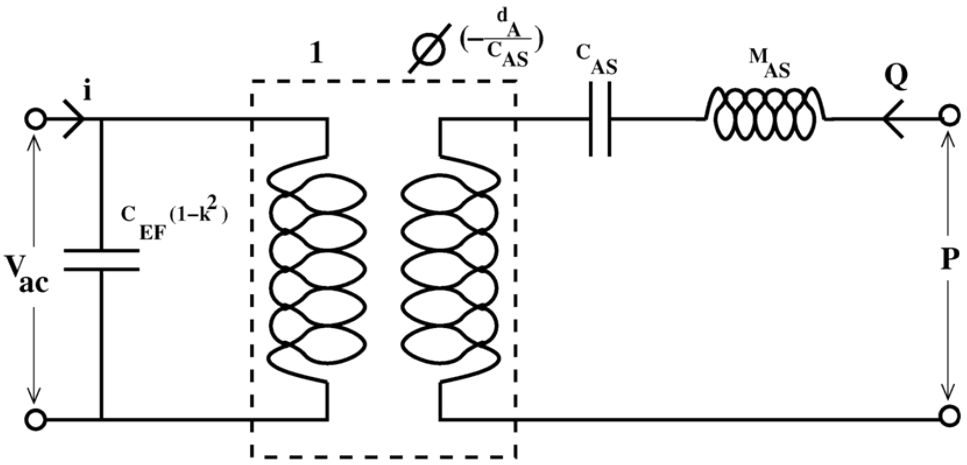

Figure 5.5: Equivalent circuit of the transducer including the inertial effects (M_{AS}) of the materials.

The imaginary part of the current is from the capacitance of the piezoelectric disk, while the real part is from the conversion of electrical energy into mechanical energy.

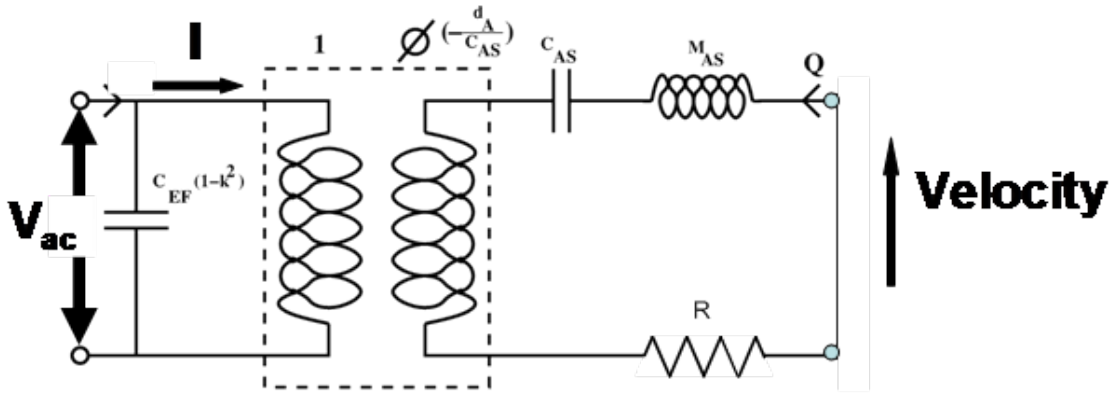

Figure 5.6: The velocity of the disk (at r=0) and the real current going in were simulated at the resonant frequency.

In an electrical circuit with two impedances in series, one of which is much larger than the other, the current through the circuit will not change appreciably if the smaller impedance is ignored. Similarly, if the transducer is placed inside a medium whose acoustic

impedance is much lower than the acoustic impedance of the transducer material, the load impedance offered by the medium can be ignored. In the transmit transducer used here, the acoustic impedances of PZT and aluminum are 33 MRayls and 8.2 MRayls; in comparison, the acoustic impedance of air is only 400 Rayls. Hence, we can treat the transducer as a resonator, neglecting the effect of surrounding medium on its mechanical behavior.

Thus, while calculating the flow variables, i and Q, we neglect the load impedance because of the air:

$$Q = V_{ac}\frac{1}{R}\frac{d_A}{C_{AS}} \tag{5.24}$$

$$i_{real} = V_{ac}\frac{1}{R}(\frac{d_A}{C_{AS}})^2 \tag{5.25}$$

Thus, the transmit efficiency is given by:

$$\eta = \frac{PQ}{V_{ac}i} = \frac{Z_{air}Q^2}{V_{ac}i} \propto \frac{velocity^2{}_{r=0}}{i} \tag{5.26}$$

5.3.4 Simulations

For transducer design, electromechanical simulations were done using COMSOL software; this consists of choosing the piezoelectric material and transducer disks' dimensions for the best possible figure-of-merit. The physical and the electrical parameters of the piezoelectric material from the material vendor [56] were used. Rayleigh damping was used to model the losses in the piezoelectric disk and the aluminum disk.

Choice of material properties:

Piezoelectric Constant (d_{31})

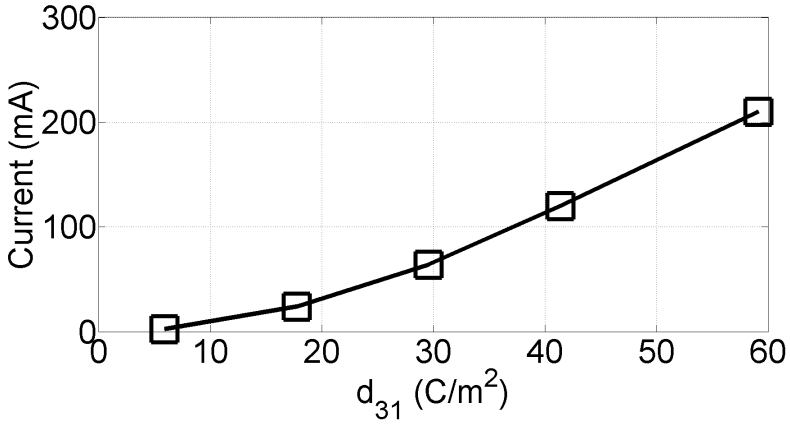

(a)

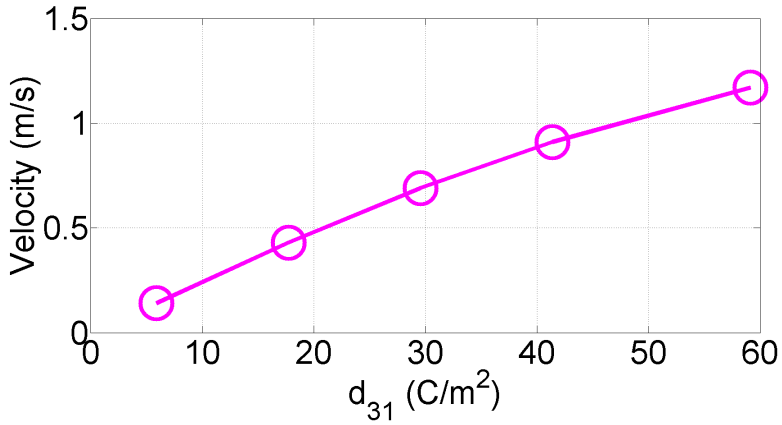

(b)

Figure 5.7: Effect of material's piezoelectric constant (d_{31}) on (a) Real part of current going into the transducer. (b) Velocity at the center of the disk (r=0).

Figure 5.7 shows the simulated i_{real} and disk velocity with the piezoelectric constant, d_{31}; both the quantities increase with d_{31} because of increase in the transducer's effective piezoelectric coefficient, d_A (Fig. 5.5). The results match well with equations 5.24 and

5.25; the current is proportional to d_{31}, while the disk velocity varies as d_{31}^2. Thus, from a design perspective, using a piezoelectric material with a high d_{31} helps increase the transmit pressure level. However, the accompanying increase in i_{real} means that the electromechanical conversion efficiency ($\eta = velocity^2/i_{real}$) of the transducer remains constant.

Piezoelectric Material's Density (ρ)

Figure 5.8 shows the simulated disk velocity and current with the density of the piezoelectric material. As such, there is no simple first-order relationship between the density, and the current or the velocity; both the quantities half for an eight-times increase in the density (Fig. 5.8).

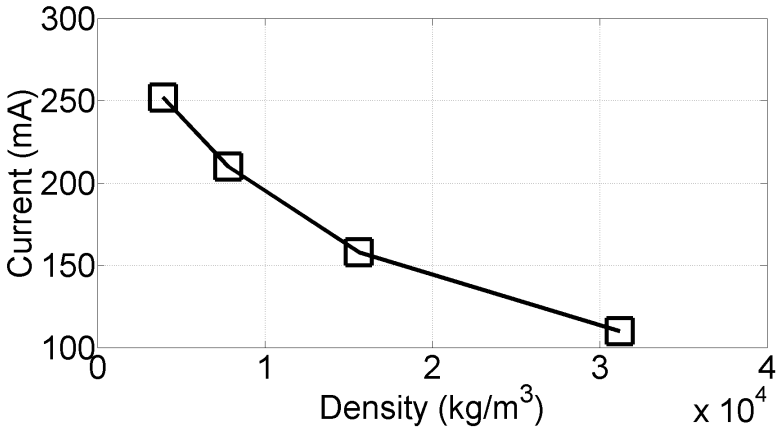

(a)

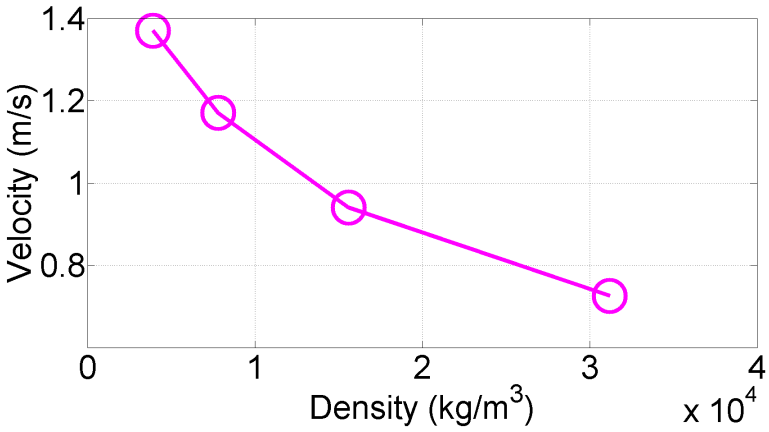

(b)

Figure 5.8: Effect of piezoelectric material density (ρ_p) on (a) Real part of current going into the transducer. (b) Velocity at the center of the disk (r=0).

Piezoelectric Material's Stiffness ($c_E{}^{11}$)

With increase in $c_{11}{}^{E}$, the stiffness of the piezoelectric material increases. This corresponds to a decrease in C_{AS} (Fig. 5.5). However, the dominant effect of increase in stiffness is more damping which results in an increase in R in the equivalent circuit. More losses in the material result in lowering in the electromechanical conversion efficiency (5.10). However, a key benefit of increased stiffness is larger transducer bandwidth, which is because of decreased resonance quality factor ($\propto \frac{1}{R}$). Thus, the choice of material stiffness entails a trade-off between transducer bandwidth and electromechanical conversion efficiency.

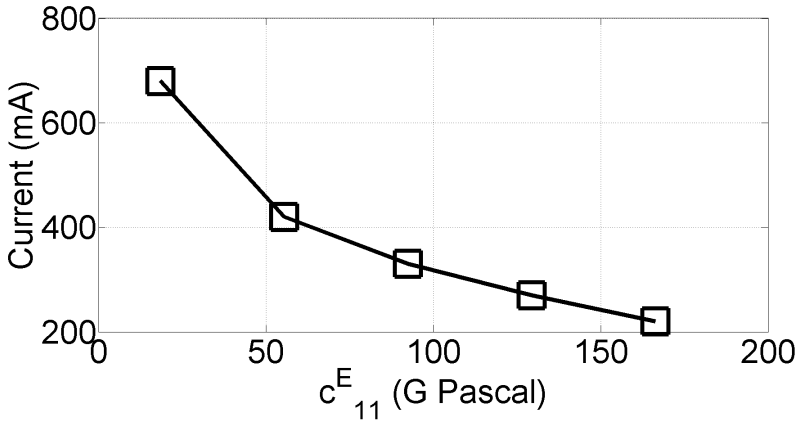

(a)

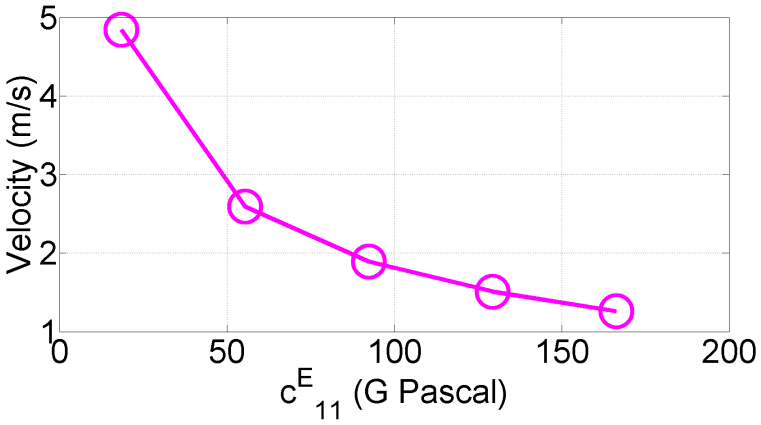

(b)

Figure 5.9: Effect of piezoelectric material's elastic constant ($c^E{}_{11}$) on (a) Real part of current going into the transducer. (b) Velocity at the center of the disk (r=0).

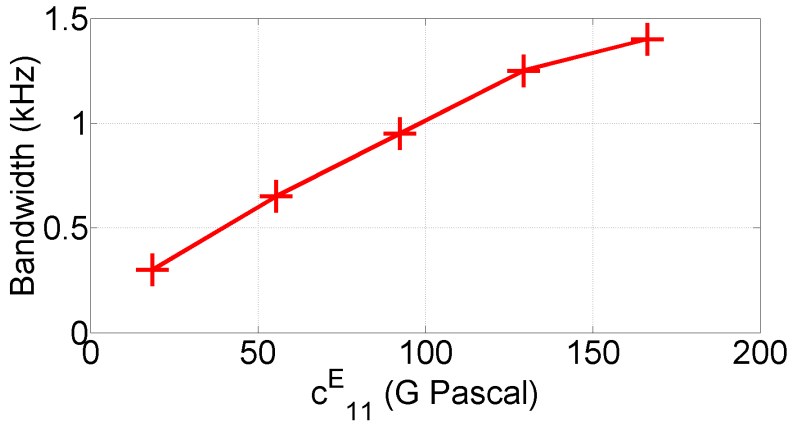

(a)

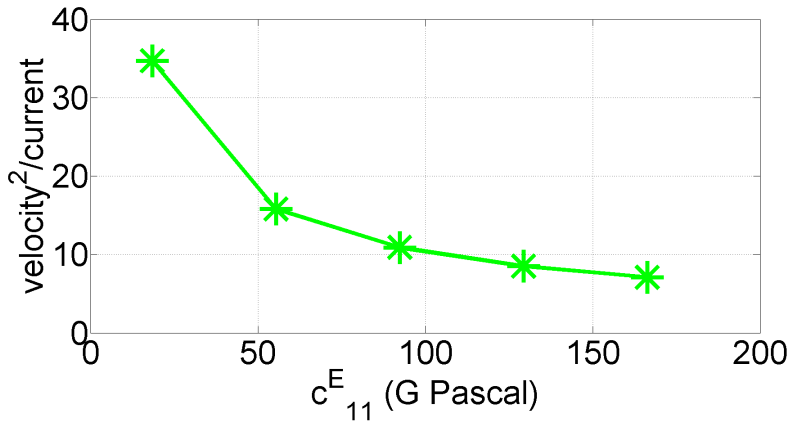

(b)

Figure 5.10: Effect of piezoelectric material's elastic constant ($c^E{}_{11}$) on (a) Bandwidth of the pressure out from the transducer. (b) A measure of the transmit efficiency in terms of velocity^2/current.

Damping Constant (β_{dK})

With an increase in the damping constant, the R in the equivalent circuit increases, and as expected from equations 5.25 and 5.24, both the current and the disk velocity decrease (Fig. 5.11). Also, efficiency is lowered and the transducer bandwidth (Fig. 5.12) is increased because of lowered resonant Q. Thus, like stiffness (${c_E}^{11}$), the choice of damping coefficient also involves a trade-off between transducer bandwidth and electromechanical conversion efficiency.

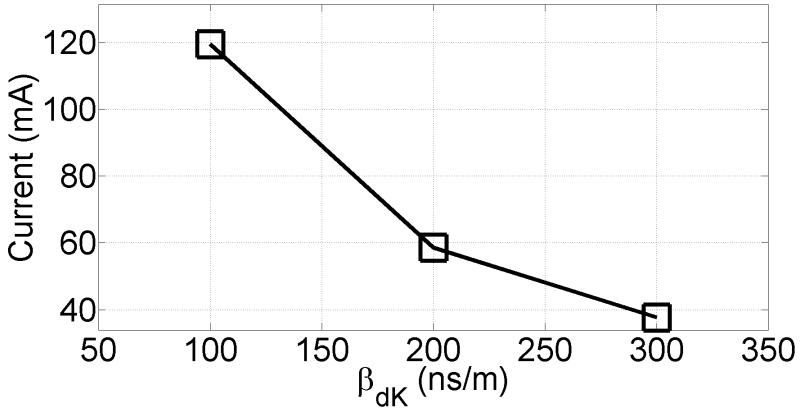

(a)

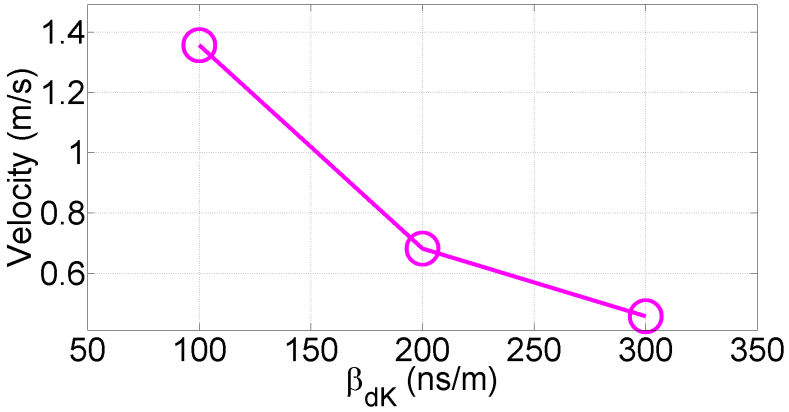

(b)

Figure 5.11: Effect of piezoelectric material's damping constant (β_{dK}) on (a) Real part of current going into the transducer. (b) Velocity at the center of the disk (r=0).

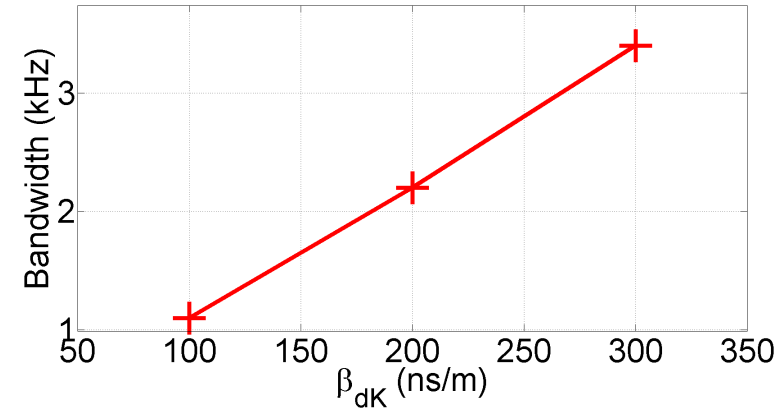

(a)

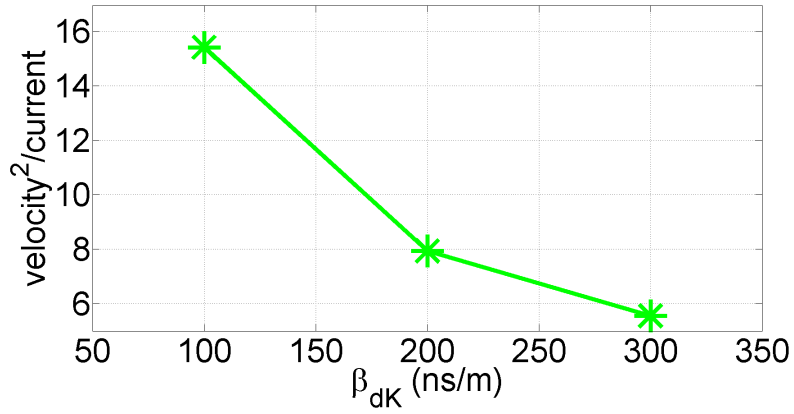

(b)

Figure 5.12: Effect of piezoelectric material's damping constant (β_{dK}) on (a) Bandwidth of the pressure out from the transducer. (b) A measure of the transmit efficiency in terms of velocity^2/current.

Choice of Transducer Physical Dimensions

Radius of the aluminum Disk (R_2)

With an increase in the radius of the aluminum disk, the acoustic compliance (C_{As}) decreases and the inertial mass (M_{AS}) increases. Both these factors result in a decrease in the resonant frequency (Table 5.3) of the transducer.

For the Rayleigh model used in this analysis, losses are directly proportional to stiffness (equation 5.21); therefore, the conversion efficiency, η, increases with radius.

Table 5.3: Effect of aluminum radius (R2) on transducer design parameters

Al radius	**Resonance frequency**	**BW**	**velocity^2/current (SI)**
8.3 mm	150.7 kHz	2.2 kHz	2.42
12.45 mm	71.6 kHz	1.6 kHz	6.5
18.7 mm	32.2 kHz	0.25kHz	16.3

Thickness of the aluminum Disk (t_2)

With an increase in the thickness of the disk, the stiffness of the structure increases. Therefore, the acoustic compliance (C_{AS}) decreases, which results in an increase in the resonant frequency (Table 5.4).

The conversion efficiency, η, decreases with thickness because of increase in stiffness.

Table 5.4: Effect of aluminum thickness (t2) on transducer design parameters

Al thickness	**Resonance frequency**	**BW**	**velocity^2/current (SI)**
0.31 mm	37.8 kHz	0.7 kHz	19
0.61 mm	71.6 kHz	1.6 kHz	6.5
1.22 mm	136.7 kHz	3.2 kHz	2.3

Ratio of Disk Radius ($\frac{R_1}{R_2}$)

Both current (i_{real}) and the velocity (Q) achieve maxima for certain values of $\frac{R_1}{R_2}$ (Fig. 5.13). Intuitively, this may be explained as follows: for very low values of R_1, the piezoelectric disk is not able to create enough stress in the structure, which results in relatively low values of displacement and velocity. While for higher values of R_1 ($\simeq R_2$), the stress needed in the outer portion of aluminum for displacement to occur is relatively large owing to the small segment length ($R_2 - R_1$). An optimum R_1/R_2 exists between these two extremes.

With an increase in the radius ratio, the stiffness of the structure increases; the resultant increase in the losses results in a reduction in conversion efficiency and an increase in the bandwidth (Fig. 5.14).

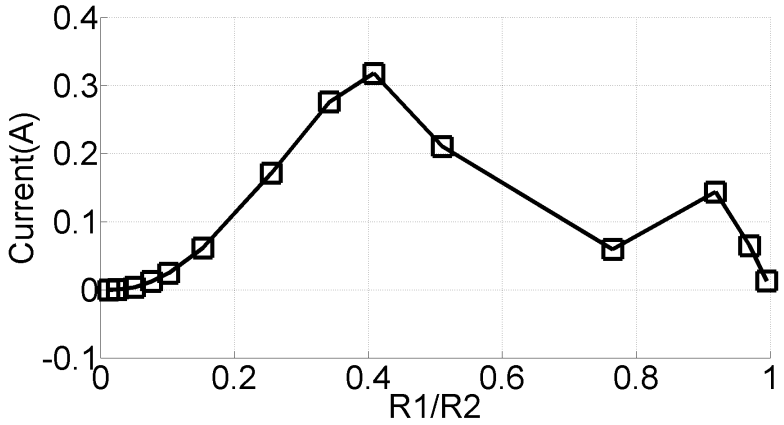

(a)

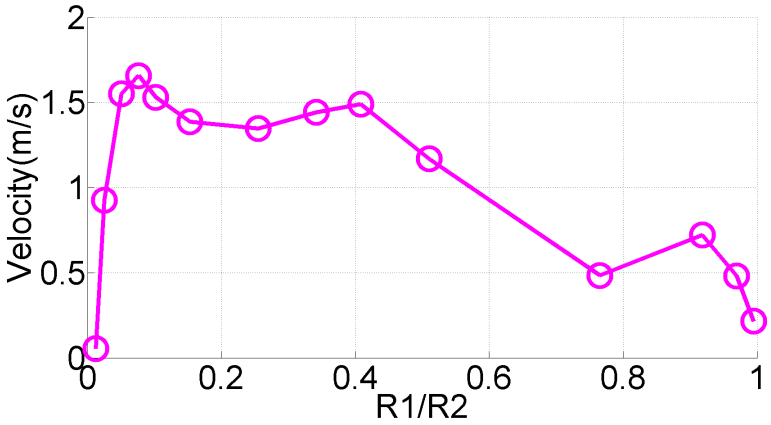

(b)

Figure 5.13: Effect of radius ratios of the piezoelectric material and aluminum(R1/R2) on (a) Real part of current going into the transducer. (b) Velocity at the disk center (r=0).

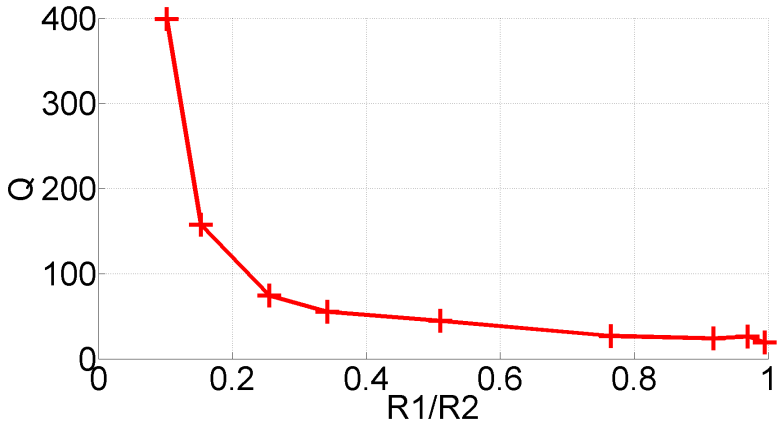

(a)

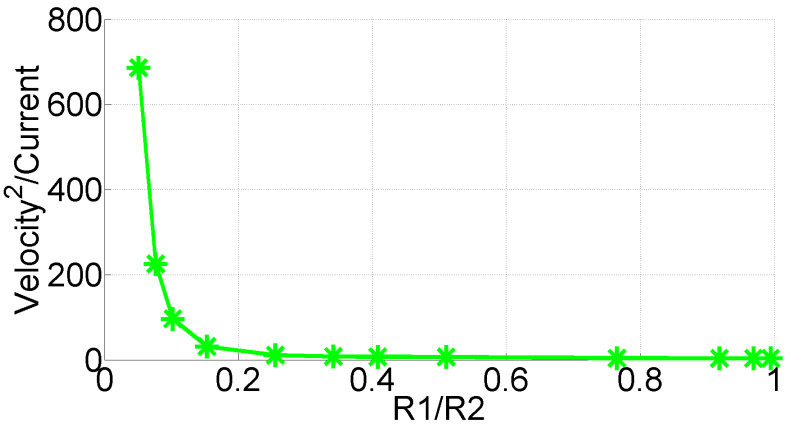

(b)

Figure 5.14: Effect of radius ratios of the piezoelectric material and aluminum(R1/R2) on (a) Quality factor of the pressure out from the transducer. (b) A measure of the transmit efficiency in terms of velocity^2/current.

Thickness of the Piezoelectric Disk (t_1)

The dominant effect of increase in the piezo disk thickness is decrease in the effective dielectric constant, d_A, because lesser electric field is developed for similar voltage across the piezoelectric material ($E = \frac{V}{t_1}$). As a result, both the current (i_{real}) and Q decrease with t_1 (Fig. 5.15). In theory, a $\frac{R_1}{R_2}$ type optimum exists for current (and velocity) vs. $\frac{t_1}{t_2}$ also. However, for the transmit transducer in this work, the optimum values of t_1 are too low for any practical purpose and only the decreasing part of the curve is relevant from a design perspective.

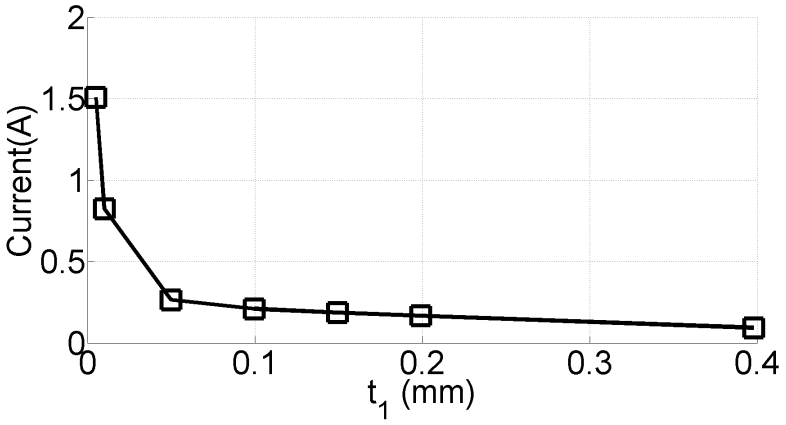

(a)

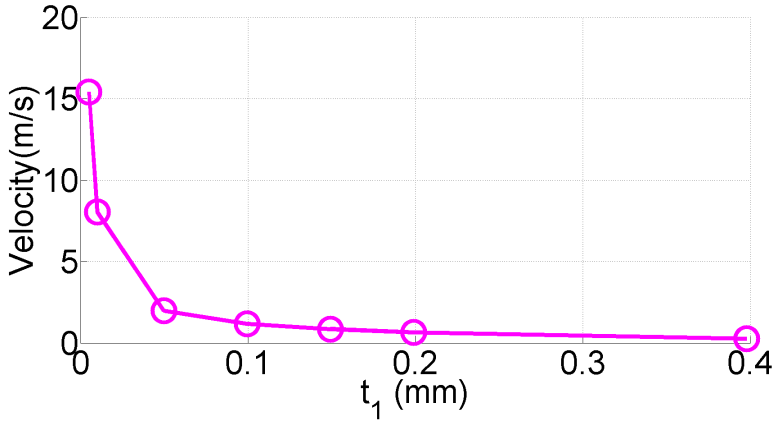

(b)

Figure 5.15: Effect of piezoelectric material's thickness (t_1) on (a) Real part of current going into the transducer. (b) Velocity at the disk center (r=0).

5.3.5 Design of the 40 kHz and the 80 kHz transducers

For the design of the 40 kHz and the 80 kHz transducers, based on the theory and the simulation results presented above, we follow the following design methodology:

• Since the main goal of the design is to increase the bandwidth of the transducer, PSI-5H4E type of PZT [56] is used because of its low quality factor (mechanical Q = 32).

• We choose the minimum available thicknesses for the PZT and the aluminum disks i.e. 0.13 mm and 0.3 mm respectively; this design choice ensures maximum conversion efficiency for the transducers. The aluminum thickness is limited by the precision to which a typical machine shop (e.g. Columbia University's Machine Laboratory) can process the metal, while the minimum thickness of PZT is limited by the vendor specifications [56].

• As discussed in section 5.3.4, the resonance frequency is determined by the dimensions of the aluminum disk. For the aluminum disk of 0.3 mm thickness, the required radius for a resonant frequency of 40 kHz (80 kHz) is 11.85 mm (8.3 mm).

• Finally, the PZT radius is chosen taking into account the design trade-off between the bandwidth of the transducer and its conversion efficiency, as shown in Fig. 5.16 and Fig. 5.17.

To achieve a bandwidth of more than 1 kHz with the 40 kHz transducer, a R_1 of more than 9.5 mm must be used. To achieve a similar bandwidth with the 80 kHz transducer, R_1 must be greater than 1.6 mm.

5.4 Summary

This chapter discussed the receive and transmit transducers which have been used in chapters 3 and 4. The electromechanical parameters of the transducers have been explained and then simulation results have been presented for the design of transmit transducer, at 40 kHz and 80 kHz, to achieve a bandwidth of 1 kHz, which is four times larger compared to the commercially available transducers. The key design trade-off between the bandwidth and the transmit efficiency of the transmit transducer has also been discussed.

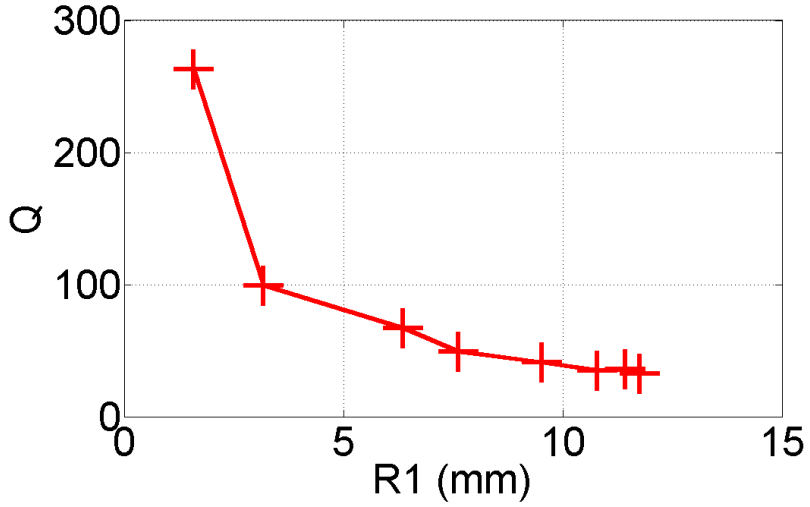

(a)

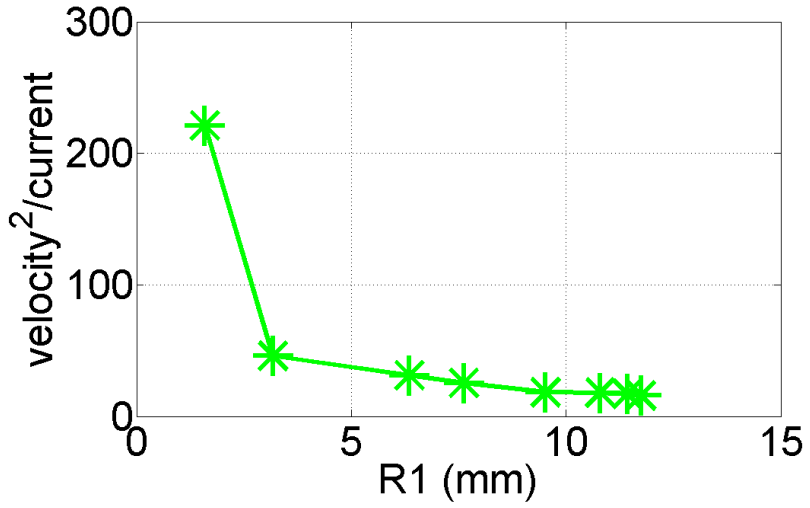

(b)

Figure 5.16: For the 40 kHz resonance frequency and t_1=0.13 mm, t_2=0.3 mm, and R_2= 11.85 mm, the effect of piezoelectric disk's radii (R_1) on (a) Quality factor, and (b) a measure of the transmit efficiency in terms of velocity^2/current.

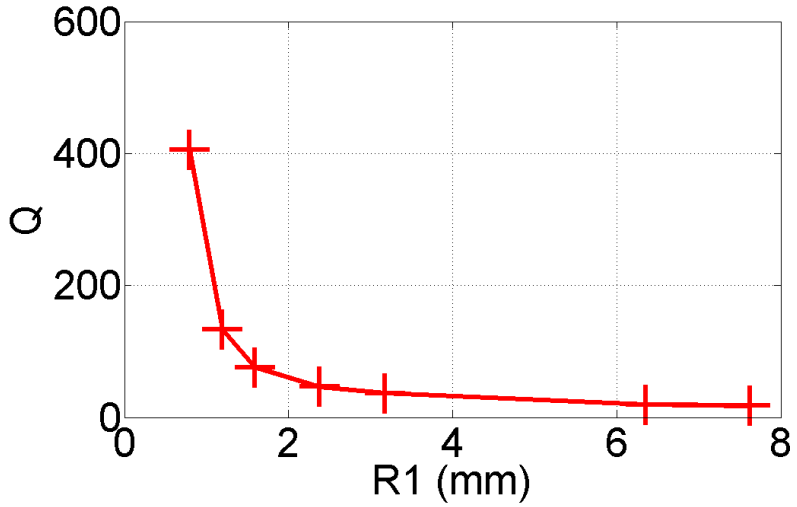

(a)

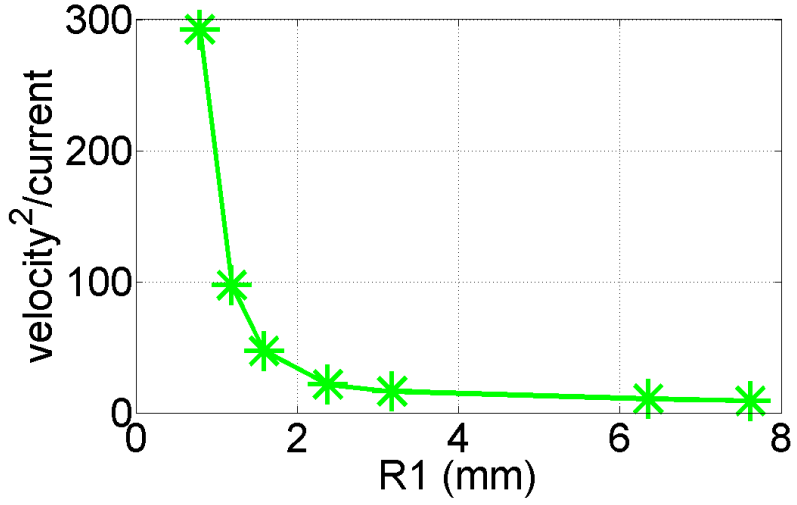

(b)

Figure 5.17: For the 80 kHz resonance frequency and t_1=0.13 mm, t_2=0.3 mm, and R_2=8.3 mm, effect of piezoelectric disk's radius (R_1) on (a) the quality factor, and (b) a measure of the transmit efficiency in terms of velocity^2/current.

Chapter 6

Conclusions and Future Work

6.1 Conclusions

In a power starved application like wireless sensor nodes, the main transceiver has to be duty-cycled to prolong node battery lifetime. Wake-up methodology is among the lowest power schemes to accomplish this, an always ON low power receiver called the wake-up receiver is used to turns ON the main receiver when needed. In this thesis, we demonstrate ultra-low power wake-up by using through-air wireless ultrasound; more than an order of magnitude reduction in receiver power consumption, compared to conventionally used radio frequencies, could be achieved. At the heart of the system is a custom-designed ultra-low power ultrasonic analog receiver IC, which consumes only $4.4\mu W$; for the proof-of-concept, the digital back-end circuitry is implemented on a FPGA and is estimated to contribute negligibly to the overall receiver power consumption. An ultrasound data net-

work consisting of three receivers and one transmitter was set up in a lecture hall, for a transmit power of $27\mu W$ more than 90% of the wake-up packets, at 1pkt/s, are detected at each of the three receivers. All the system blocks, receiver IC, ultrasound communication channel and Tx-Rx transducer pair, were individually characterized in different environments to understand the interaction between the electrical and mechanical domains. Also discussed, in the thesis, is the transducer design for increasing the communication data rate and for extending the communication distance range.

6.2 Future Work Directions

6.2.1 Ultrasonic Wake-up

Wake-up receiver design improvements. The design of the wake-up receiver circuit can be improved to reduce the power consumption even further and also to reduce the chip area. In this design we had used op-amp based resistive feedback amplifiers. These op-amps must be designed for sufficient gain at the operating frequency, which means that their unity-gain bandwidth must be several times, typically 10x, the operating frequency. In comparison, open-loop amplifiers can offer lower power consumption and should be investigated as a part of future work. Further, the chip area can be reduced by using transistor-based resistors instead of large poly resistors.

Since the focus of this research was on testing the feasibility of through-air wireless ul-

trasound for the application of wake-up, the design of a relatively simple energy-detection OOK receiver was sufficient. In future, different modulation schemes may be studied to understand the effect of the choice of modulation on the performance of through-air wireless ultrasound system [57].

Omnidirectional transmit and receive transducers. For the applications targeted in this thesis, there are primarily two candidate transducers: PVDF film based cylindrical transducer and metal-piezoelectric unimorph. In the research done so far, we have used PVDF film transducers at the receiver because they are capable of omni-directional reception, while at the transmitter, unimorph transducers have been used because of their high electro-mechanical conversion efficiency. A combination of unimorphs was used for wide directional coverage. However, this comes at the cost of a large form factor at the transmitter. Thus, this implementation is only suitable for a case where a central base station (transmitter) wakes up ultrasonic receivers in a network. As a part of future work, unimorph omnidirectional receive and transmit transducers may be made. This leverages the high conversion efficiency of the unimorphs and makes the transducer form factors suited to wireless sensor application. Commercially available ultrasonic transducers are mostly used for ranging applications and are hence designed for directional transmission and reception. Thus, to extend the usage of ultrasound to a new application like data communication, custom designing the transducers (as discussed in brief in chapter 5) can be an interesting work for future research.

Increasing the carrier frequency. Using a higher communication frequency than the

currently used 40kHz carrier will help increase the communication data rate. Further, using higher carrier frequencies helps keep the communication outside the audible band of common pets like dogs and cats (45kHz and 65kHz respectively). However, at higher frequencies ultrasound suffers more through-air absorption and transducer sensitivity is also poorer because of smaller dimensions. Pressure-distance measurements can help understand how through-air attenuation changes at different ultrasonic carrier frequencies. These measurements together with the transducer sensitivity simulations can be used to choose an optimum communication frequency.

Custom designed transducers for higher bandwidth. The communication system in this thesis uses commercially available transducers. These transducers are designed for ranging applications and have very low bandwidth. A communication data rate of only 250bps could be achieved because of the narrow bandwidth of the unimorph transducer used at the transmitter. A computer model of the unimorph transducer was simulated using the COMSOL multiphysics software. As explained in section 5.3.5, the bandwidth of the transducer can be increased by choosing transducer dimensions appropriately. However, this increase comes at the cost of lower electro-mechanical efficiency, thus necessitating careful design decisions. As a future work, more extensive simulations may be done and, the transducers fabricated and tested for performance.

Investigating the effect of background noise and reverberations on system performance. In the field measurements done so far, some effects of reflections on system performance have been observed. In the car garage measurements (section 4.2.2), it was

observed that pressure fluctuations are more prominent at larger Tx-Rx distances. The amplitude of the received pressure changed by as much as 5x for a distance of 18 meters. Similarly, for the ultrasound data network measurements in the lecture hall, it was observed that $P_{detection}$ changed over time because of reflections (Fig. 6.1) and possibly noise also.

Relative to RF-based communication, through-air ultrasound data communication is a new area. While, modeling the ultrasonic channel was beyond the scope of this thesis research, heuristic approach may be used to understand the effect of reflections and background noise on the wireless ultrasound data; extensive in-field measurements can be carried out in different environments and over reasonably long durations of time.

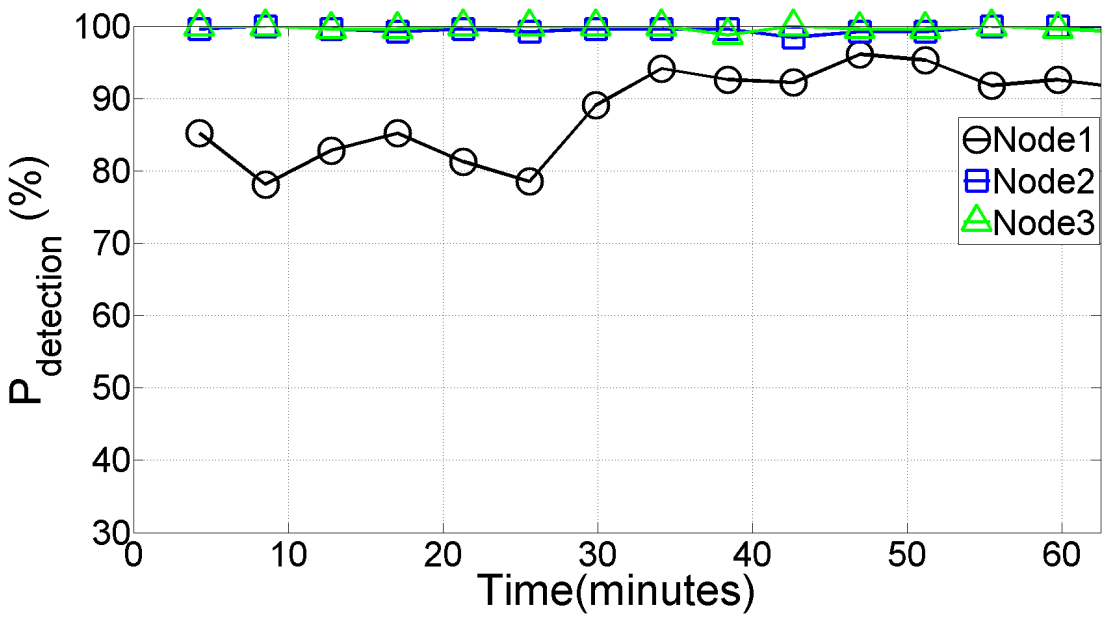

Figure 6.1: Measurements to show change in $P_{detection}$ values (at receiver node1) over time, due to reflections.

6.2.2 Other Possible Applications

Development of CMOS-assisted organic platform Organic electronics has major advantages in the realization of sensing and energy-harvesting components. CMOS electronics offers low-power signal processing and tremendous ability for integration. Silicon chips can be bonded to organic substrates to exploit the unique benefits of both these technologies. This synergistic platform can be a significant step towards the realization of low-cost and ultra-low power autonomous sensor nodes.

CMOS-compatible transmitter circuitry The unimorph PZT-based transducer, used at the transmitter, can withstand an excitation of more than 10 $V_{p\text{-}p}$; this is much higher than the voltages that modern CMOS technologies can withstand. Thus, to achieve maximum possible communication distance range, special circuit techniques and chip stacking techniques have to be explored.

Localization applications The microphones and the transducers portable devices like smart phones and laptops can work for frequencies beyond the audible band. The speed of ultrasound is relatively low compared to the conventionally used radio waves, which means that phase information can easily used to locate the position of one device relative to another. The device-to-device communication can be also be used for transmitting device information, for transmitting environmental data and for synchronizing clocks.

Recording ambient sound Microphones assisted with low-power electronics can be

used to record ambient noise or ultrasound signals for detecting leaks, component failure and seismic activity.

Chapter 7

Appendix

For a detailed noise analysis of the receiver, a mathematical model of the receiver was made in verilog to reduce the circuit simulation time. Pnoise simulations were done to observe the variation in the signal-to-noise ratio at the receiver output with the front-end gain and the LNA current; optimum design points were chosen based on this analysis. In this appendix, we describe the mathematical model and the parameters used for each stage of the receiver.

7.1 Mathematical model of the carrier-band amplifiers

All the transistors in the receiver circuit operate in weak inversion; therefore, the following equation has been used to model current:

$$\mathrm{I} = \mathrm{I_s exp}(\frac{\mathrm{V_{GS}}}{\zeta\ \mathrm{kT/q}}) \tag{7.1}$$

For the two branches of a differential amplifier, the current is then given by:

$$\mathrm{I_o^+} = \frac{\mathrm{I_{tail\ current}}}{1 + exp(\frac{v_{in}}{\zeta kT/q})} \tag{7.2}$$

$$\mathrm{I_o^-} = \frac{\mathrm{I_{tail\ current}}}{1 + exp(\frac{-v_{in}}{\zeta kT/q})} \tag{7.3}$$

where ζ is the subthreshold slope factor, $I_{tailcurrent}$ is the tail current of the differential amplifier, and v_{in} is the input ac signal.

A pole (p_1) has also been included in the code to model the amplifier output pole arising from the combination of amplifier small-signal output resistance and the input capacitance of the succeeding-stage amplifier. To model the transistor thermal noise, the current source with a noise spectral density of – $\bar{i_n}^2 = 4KT\gamma I$ – has been used.

Using the transistor model, each stage is simulated individually to extract the model parameters, which are then included in the mathematical model written in verilog. Below we include tables with value of parameters for each stage of the carrier-band.

7.1.1 LNA

The model parameters for the LNA in Fig. 7.1 are shown in Table 7.1.

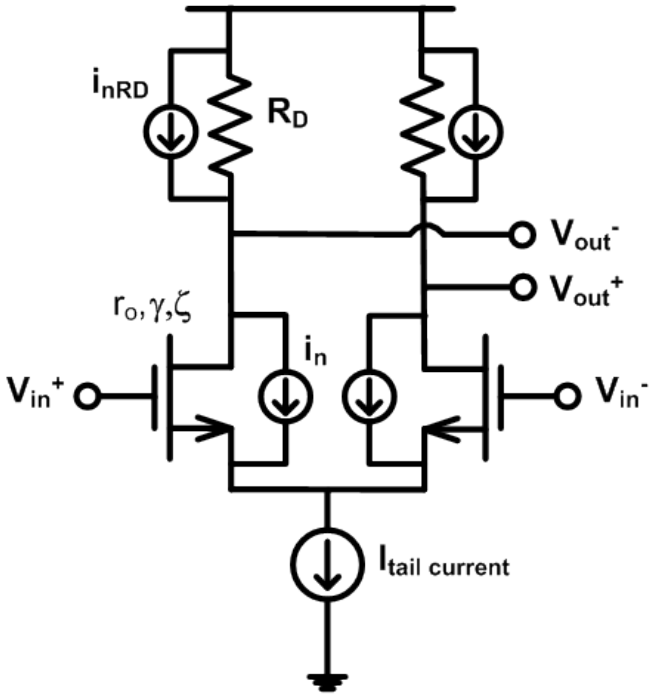

Figure 7.1: LNA schematic with the parameters used for circuit modeling.

Table 7.1: LNA verilog parameters

Parameter	**Value**
r_o	700kΩ
R_D	258 kΩ
ζ	1.25
γ	0.9
p_1	1.55 MHz

7.1.2 Second-stage amplifier

The model parameters for the second-stage amplifier in Fig.7.2 are shown in Table 7.2. The relatively low value of the buffer output pole is because of its low current consumption of only 40 nA.

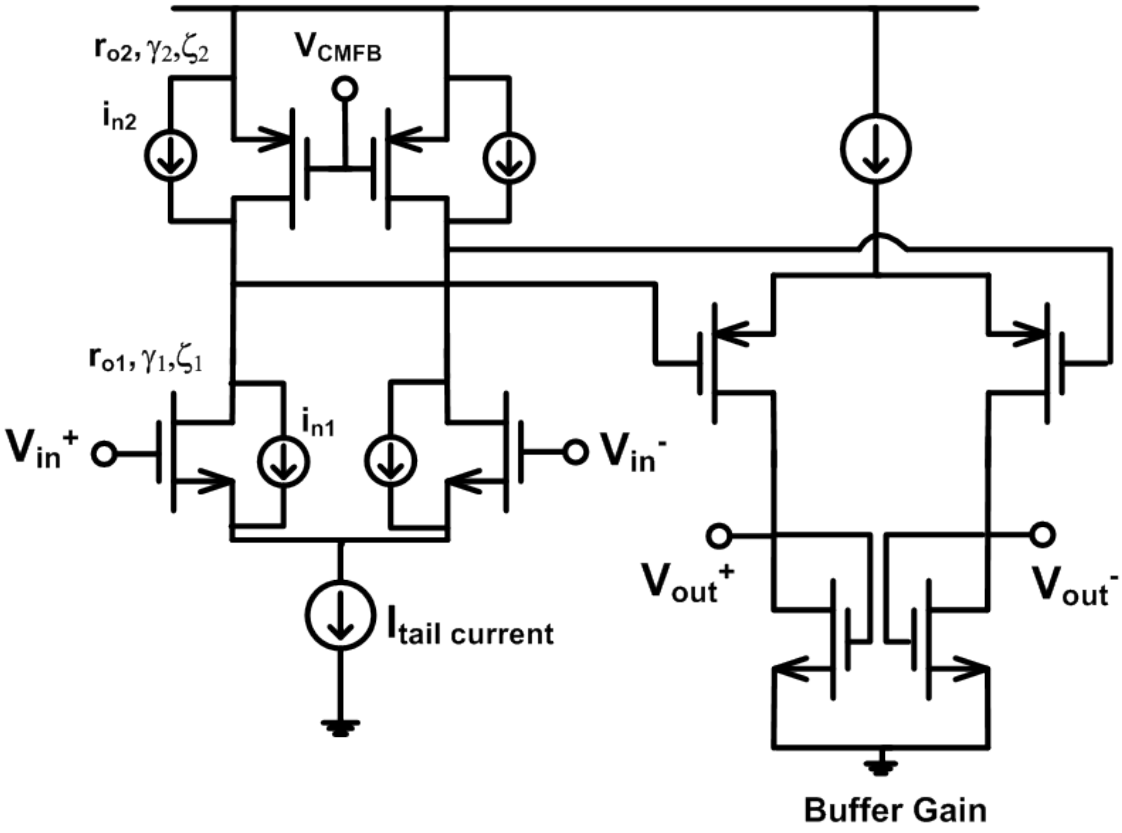

Figure 7.2: Second-stage carrier-band amplifier schematic with the parameters used for circuit modeling.

Table 7.2: Second-stage amplifier verilog parameters

Parameter	**Value**
r_{o1}	6.95 MΩ
r_{o2}	25.7 MΩ
$I_{tail\ current}$	125.7nA
Buffer gain	0.66
ζ_1	1.2
γ_1	0.8
ζ_2	1.25
γ_2	0.8
p_1(amplifier)	1.55 MHz
p_2(buffer)	292 kHz

7.1.3 Variable-gain amplifiers

The model parameters for the variable-gain amplifiers (Fig.7.3) are shown in Table 7.3 and Table 7.4. Even though both the stages are designed identically, the small difference in the operating parameters is because of slightly different bias voltages.

Table 7.3: Variable-gain amplifier, VGA1 verilog parameters

Parameter	**Value**
r_{o1}	7.82M Ω
$r_{o2} \parallel r_{o3} \parallel r_{o4}$	28.26 MΩ
$I_{parallelbranches}$	58 nA
$I_{tailcurrent}$	139 nA
$\zeta_{1,2,3,4}$	1.24
$\gamma_{1,2,3,4}$	1
p_1	239 kHz
Extra attenuation	0.975

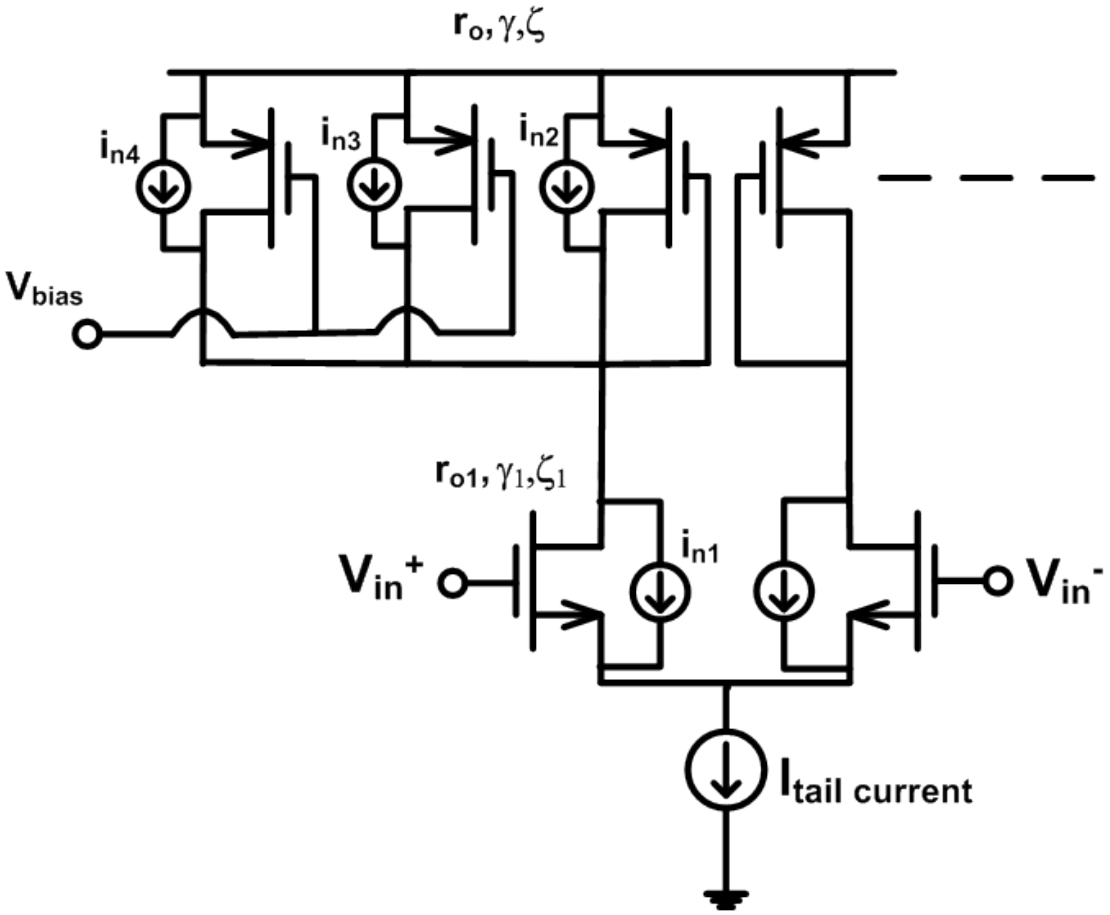

Figure 7.3: Variable-gain amplifier schematic with the parameters used for circuit modeling.

Table 7.4: Variable-gain amplifier, VGA2 verilog parameters

Parameter	**Value**
r_{o1}	5.9 MΩ
$r_{o2} \parallel r_{o3} \parallel r_{o4}$	28.65 MΩ
$I_{parallelbranches}$	58 nA
$I_{tailcurrent}$	139 nA
$\zeta_{1,2,3,4}$	1.24
$\gamma_{1,2,3,4}$	1
p_1	241 kHz
Extra attenuation	.72

7.1.4 Last-stage carrier-band amplifier

Same topology as shown in the Fig. 7.2 has been used in the last-stage of the carrier-band. The verilog parameters are shown in Table 7.5.

Table 7.5: Last-stage carrier-band amplifier verilog parameters

Parameter	**Value**
r_{o1}	31.15 M Ω
r_{o2}	127.6 MΩ
$I_{tailcurrent}$	24.09 nA
ζ_1	1.18
γ_1	1
ζ_2	1.23
γ_2	1
p_1	200 kHz

7.2 Verification of the carrier-band amplifier models

The verilog model matches well with the transistor model of the circuit as shown by the small-signal ac simulations in Fig. 7.4 and by the small-signal noise simulations in Fig. 7.5. Note that because the mathematical model ignores the effect of flicker noise, the noise from the mathematical model is slightly lower than that from the transistor model. However, this difference is only for frequencies that are outside the 40 kHz band-of-interest, and hence, this does not cause any significant inaccuracy for the purpose of this analysis.

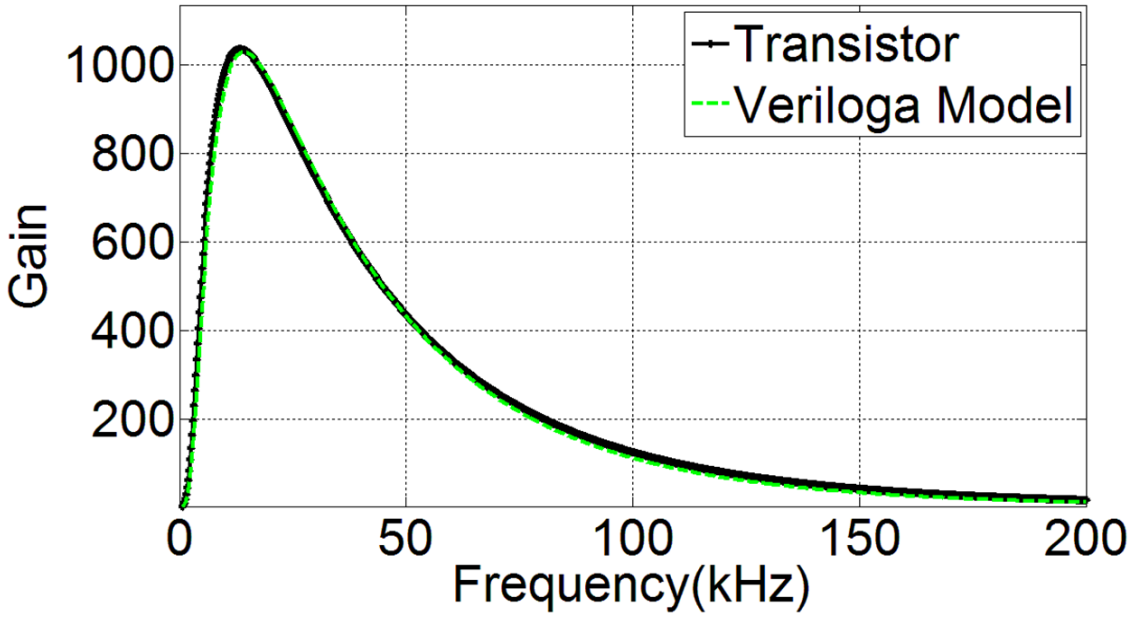

Figure 7.4: Simulated carrier-band gain vs. frequency with both the verilog model and the transistor simulations.

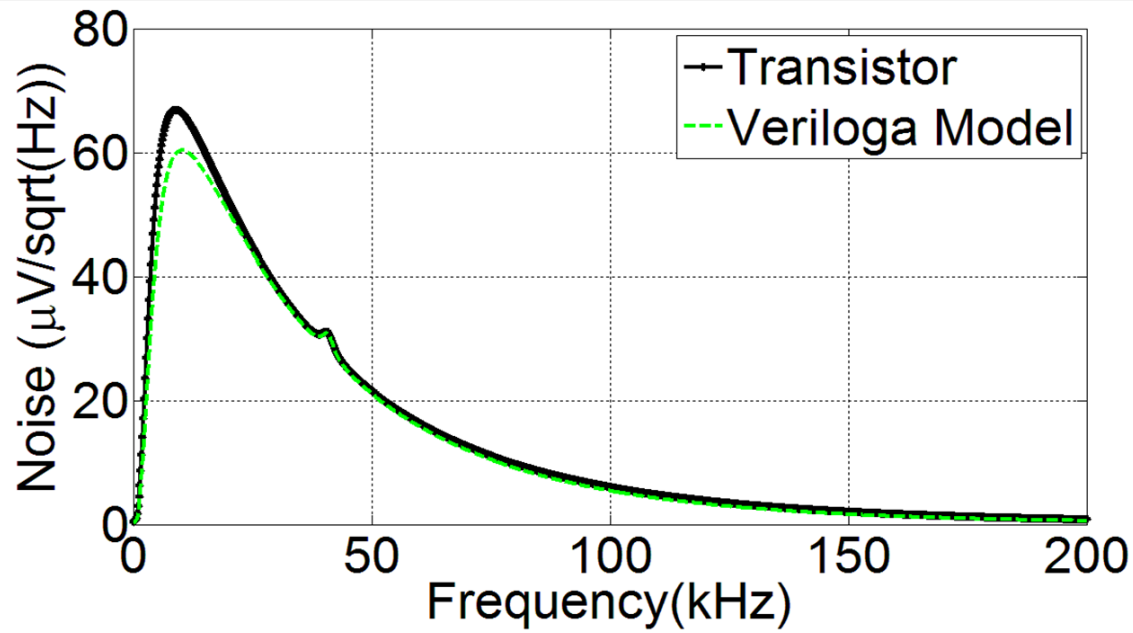

Figure 7.5: Simulated carrier-band noise vs. frequency with both the verilog model and the transistor simulations.

7.3 Gilbert-cell modeling

The current through the two differential branches of the gilbert-cell mixer in Fig. 7.6 is given by:

$$i_{out,BB}{}^{+} = I_S \frac{exp\left(\frac{v_{LO}{}^{+}}{2\zeta kT/q}\right) exp\left(\frac{v_{RF}{}^{+}}{2\zeta kT/q}\right) - exp\left(\frac{v_{LO}{}^{-}}{2\zeta kT/q}\right) exp\left(\frac{v_{RF}{}^{-}}{2\zeta kT/q}\right)}{exp\left(\frac{v_{LO}{}^{+}}{2\zeta kT/q}\right) + exp\left(\frac{v_{LO}{}^{-}}{2\zeta kT/q}\right)} \tag{7.4}$$

$$i_{out,BB}{}^{-} = I_S \frac{exp\left(\frac{v_{LO}{}^{+}}{2\zeta kT/q}\right) exp\left(\frac{v_{RF}{}^{-}}{2\zeta kT/q}\right) - exp\left(\frac{v_{LO}{}^{-}}{2\zeta kT/q}\right) exp\left(\frac{v_{RF}{}^{+}}{2\zeta kT/q}\right)}{exp\left(\frac{v_{LO}{}^{+}}{2\zeta kT/q}\right) + exp\left(\frac{v_{LO}{}^{-}}{2\zeta kT/q}\right)} \tag{7.5}$$

$$i_{out,BB} = i_{out,BB}{}^{+} - i_{out,BB}{}^{-} \tag{7.6}$$

$$\implies i_{out,BB} = I_{BIAS,mix} \frac{\left(exp\left(\frac{v_{in,mix}}{2nkT/q}\right) - exp\left(\frac{-v_{in,mix}}{2nkT/q}\right)\right)^2}{exp\left(\frac{v_{in,mix}}{2nkT/q}\right) + exp\left(\frac{-v_{in,mix}}{2nkT/q}\right)} \tag{7.7}$$

For the typical case of mixer transistors operating in saturation, the two halves of the mixer are symmetric. However, note that for the self-mixer used in this research transistors operate in weak inversion and the two halves of the mixer are not symmetric. Table 7.6 shows the gilbert-cell parameters used in the verilog model.

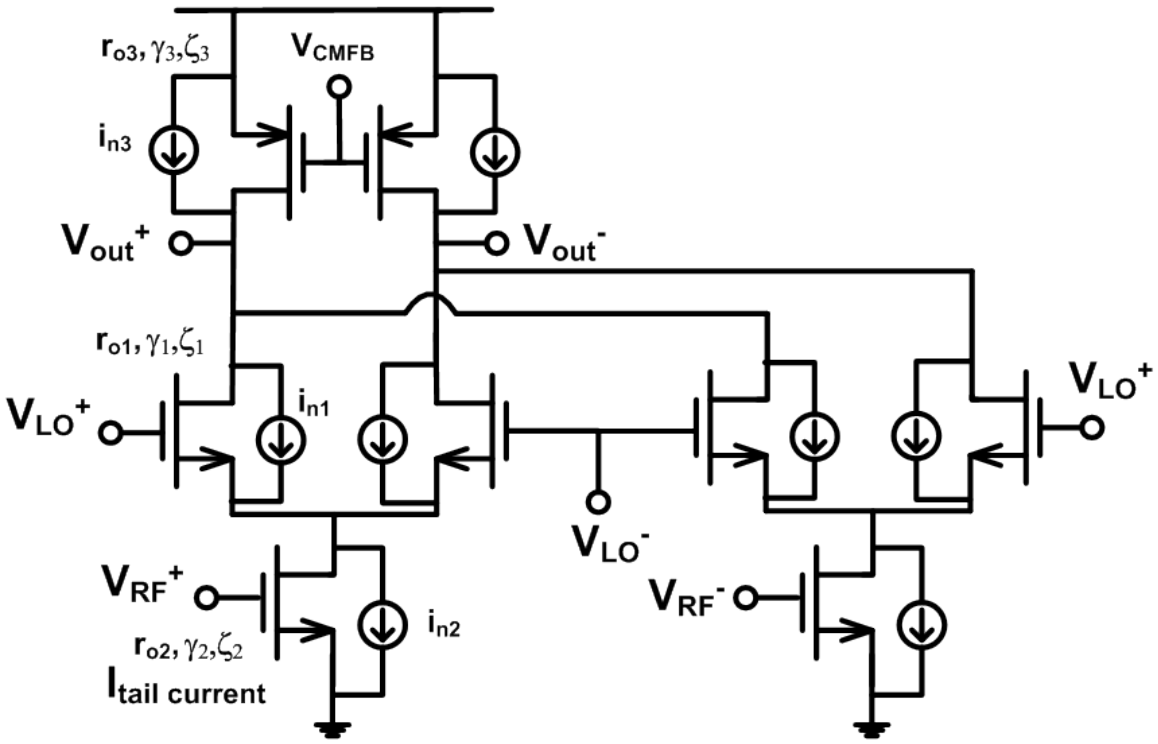

Figure 7.6: Gilbert-cell with the model parameters.

Table 7.6: Gilbert-cell based self-mixer parameters

$I_{tailcurrent}$	29 nA
ζ_1	1.29
$\gamma_{1,2}$	1
ζ_2	1.27
$K_{1,2,3}$ (flicker noise power @ 1 Hz)	1.38e^{-23}

7.4 Modeling of the op-amps in the baseband

The two-stage op-amp shown in Fig. 7.7 is used in the each of the three stages of the baseband amplifiers. The verilog model for the first-stage of the op-amp is same as used for the differential amplifier in section 7.1, given by equations 7.2 and 7.3. For the second stage we have used the equation, $v_{out,opamp} = (r_{03} \parallel r_{04})(\frac{I_{second_stage}}{\zeta v_{th}})v_{out,firststage}$. In the design, the unity gain bandwidth of the op-amp is around 35 kHz and the location of the second pole is beyond 60 kHz; relative to the frequency of interest (1 kHz), the second pole is at a very high frequency and hence the op-amp can be modeled as a single pole system without a significant loss in the accuracy.

A simplified model has been assumed to model 1/f flicker noise by using a noise spectral density of — ${i_n}^2 = K/f^n$.

Table 7.7, 7.8 and 7.9 show the parameters used for the three op-amps. Despite the same transistor sizes and biasing currents for the three stages, the derived model parameters are different because of different loading from the feedback resistors.

7.5 Verification of the carrier-band amplifier models

The simulated noise of the baseband amplifiers from the verilog model matches well with the transistor simulations (Fig. 7.8). The small difference between the two for frequencies below 100 Hz is because of the simple flicker noise model used in the verilog code; the model uses a flicker noise exponent of 1, when actually n increases as the frequency is

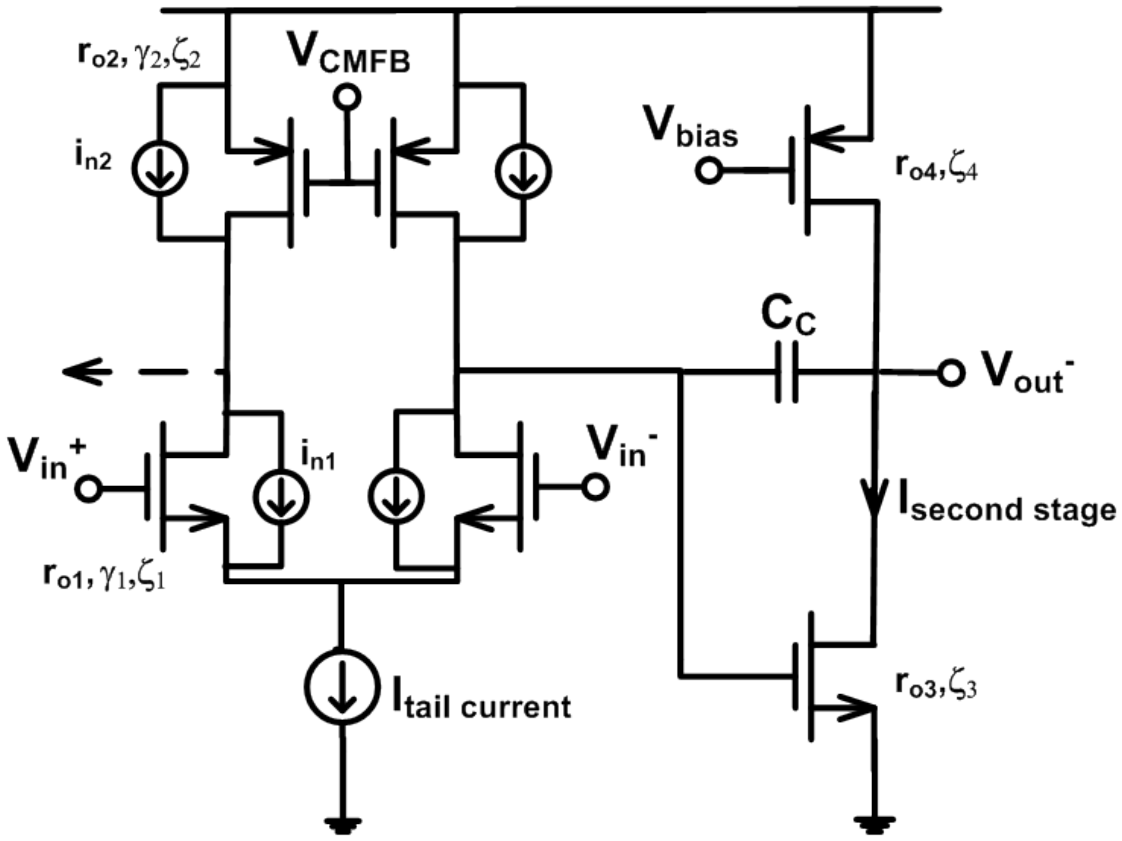

Figure 7.7: Schematic of the op-amp with the verilog model parameters.

Table 7.7: Op-amp used in the Transimpedance amplifier

Parameter	**Value**
r_{o1}	8.9 M Ω
r_{o2}	66.9 MΩ
r_{o3}	92.6 MΩ
r_{o4}	36.45 MΩ
$I_{tailcurrent}$	58.6 nA
$I_{secondstage}$	41.4 nA
ζ_1	1.2
ζ_2	1.3
ζ_3	1.4
$\gamma_{1,2,3}$	1.16
R_{load}	0.56 MΩ
p_1	3 kHz
K_1 (flicker noise power NMOS @ 1 Hz)	$2.38e^{-24}$
K_2 (flicker noise power PMOS @ 1 Hz)	$1e^{-22}$

Table 7.8: Parameters of the op-amp, used in the second-stage baseband amplifier, when loaded

Parameter	**Value**
r_{o1}	20.86 M Ω
r_{o2}	42.8 MΩ
r_{o3}	65.3 MΩ
r_{o4}	20.86 MΩ
$I_{tailcurrent}$	58 nA
$I_{secondstage}$	76 nA
ζ_1	1.2
ζ_2	1.3
ζ_3	1.46
$\gamma_{1,2,3}$	1.14
R_{load}	0.49 MΩ
p_1	1.5 kHz
K_1 (flicker noise power NMOS @ 1 Hz)	2.38e^{-24}
K_2 (flicker noise power PMOS @ 1 Hz)	0.7e^{-22}

Table 7.9: Parameters of the op-amp, used in the last stage of the baseband amplifier, when loaded

Parameter	**Value**
r_{o1}	44.15 M Ω
r_{o2}	70 MΩ
r_{o3}	50.3 MΩ
r_{o4}	43 MΩ
$I_{tailcurrent}$	54.8 nA
$I_{secondstage}$	60.7 nA
ζ_1	1.2
ζ_2	1.3
ζ_3	1.43
$\gamma_{1,2,3}$	1.14
R_{load}	4.4 MΩ
p_1	174 kHz
K_1 (flicker noise power NMOS @ 1 Hz)	2.38e^{-24}
K_2 (flicker noise power PMOS @ 1 Hz)	0.4e^{-22}

decreased. However, this difference does not significantly affect the overall receiver noise because the majority of the noise is contributed by the front-end.

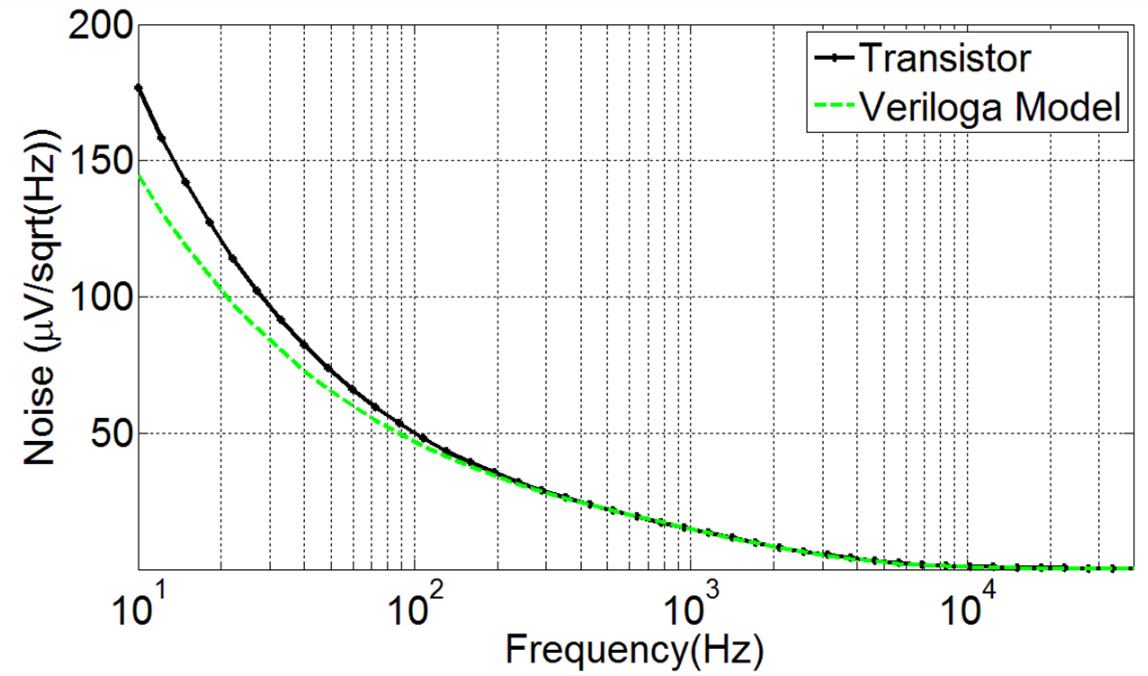

Figure 7.8: Pnoise simulations of the base-band amplifiers with both the verilog model and the transistor simulations.

7.6 Full receiver simulations

To simulate the signal-to-noise ratio at the receiver output, a 125 Hz square-wave modulated OOK signal of amplitude 37 μV_{rms} is applied at the receiver input. The integrated noise at the receiver output is simulated for a bandwidth of 1 kHz.

Figure 7.9 shows the change in the receiver SNR_{out} with LNA current using the verilog model. For LNA current below about 2μA, the SNR changes appreciably, however for

higher values the SNR becomes constant; this is because at higher values of LNA current, the noise at the receiver output is dominated by other circuit blocks and even an increase in the LNA current does not significantly changes the SNR.

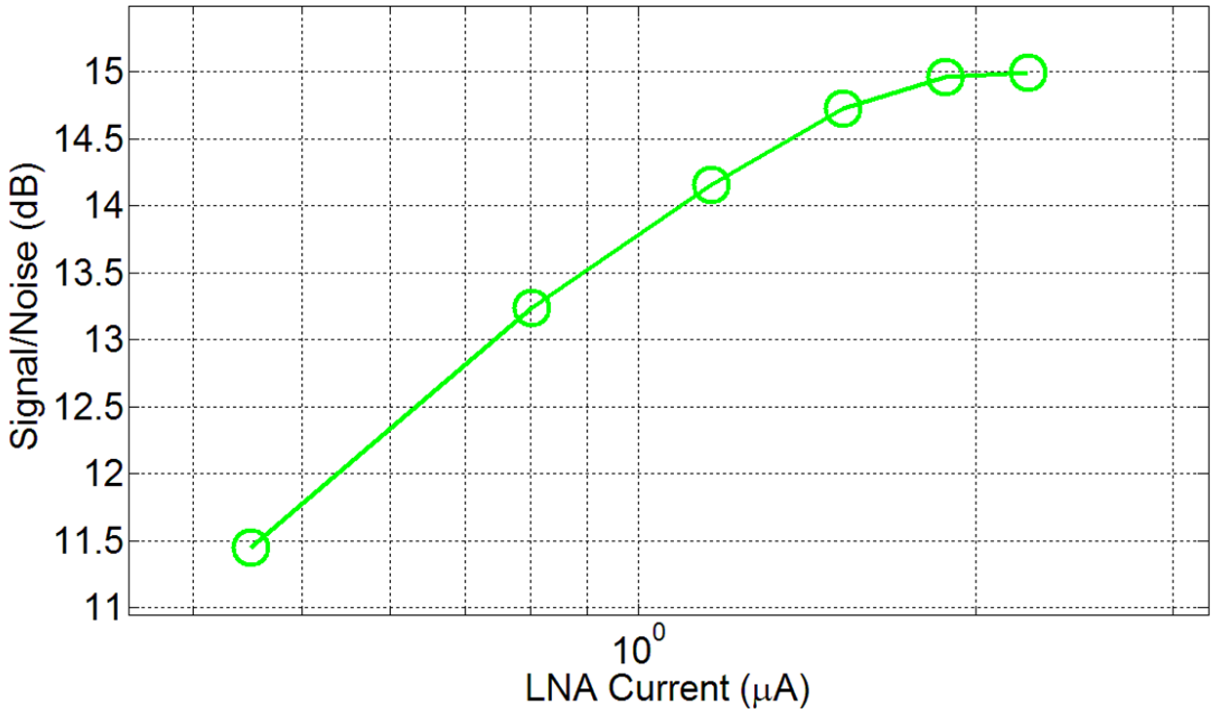

Figure 7.9: Simulation results for the SNR at receiver output vs. LNA current consumption.

Figure 7.10 shows the simulated SNR_{out} vs. the input voltage for OOK signals modulated with square waves of frequencies of 125 Hz, 250 Hz and 500 Hz. The verilog model was also used to estimate the front-end gain needed to achieve the targeted SNR; the results were presented in section 3.2.2 (Fig. 3.8).

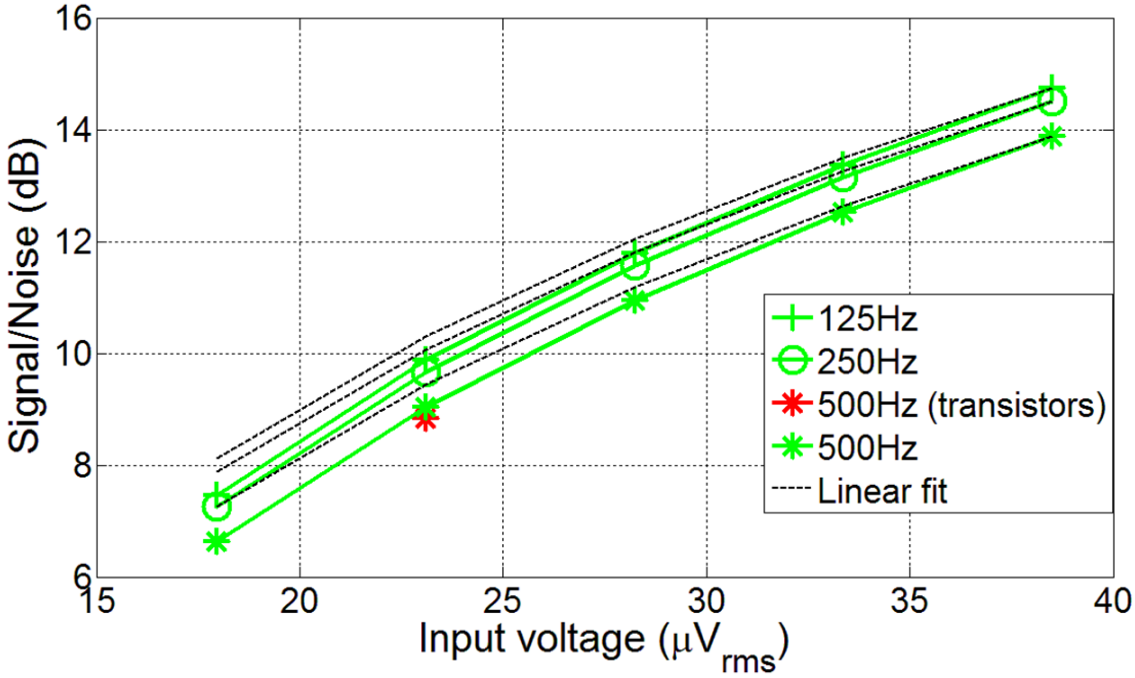

Figure 7.10: Simulation results for the SNR at receiver output vs. receiver input voltage.

Part I

Bibliography

Bibliography

[1] B. W. Cook, S. Lanzisera, and K. S. J. Pister, "SoC issues for RF smart dust," in *Proc. of the IEEE*, vol. 94, pp. 1177-1196, June 2006.

[2] J. Reason and J. M. Rabaey, "A Study of Energy Consumption and Reliability in a Multi-Hop Sensor Network," *in Proc. ACM SIGMOBILE Mobile Computing and Communications Review*, vol. 8 Ussue 1, pp. 84-97, Jan. 2004.

[3] C. Guo, L. C. Zhong, and J. M. Rabaey, "Low Power Distributed MAC for Ad Hoc Sensor Radio Networks," *in Proc. of IEEE GlobeCom 2001*, San Antonio, Nov. 2001.

[4] E.-Y. Lin, J. Rabaey, and A. Wolisz, "Power-efficient rendezvous schemes for dense wireless sensor networks," in *Proc. of IEEE Int. Conf. Communications*, vol. 7, pp. 3769-3776, Jun. 2004.

[5] L. Gu and J.A. Stankovic, "Radio-Triggered wake-up capability for sensor networks," *in Proc. IEEE Real-Time and Embedded Technology and Applications Symposium*, 2004.

[6] W. Ye, J. Heidemann, and D. Estrin, "An energy-efficient mac protocol for wireless sensor networks," *in Proc. International Annual Joint Conference of the IEEE Computer and Communications Societies (INFOCOM 2002)*, June 2002.

[7] T.V. Dam, K. Langendoen, "An adaptive energy-efficient MAC protocol for wireless sensor networks," *in Proc. of ACM Conf. on Embedded Networked Sensor Systems (SenSys)*, November 2003.

[8] J. Hill and D. Culler, "A Wireless Embedded Sensor Architecture for System-level Optimization," *Technical report, U.C. Berkeley*, 2001.

[9] Z. Chen, A. Khokar, "Self Organization and Energy Efficient TDMA MAC Protocol by Wake Up For Wireless Sensor Networks," *in Proc. IEEE International Conference on Sensors and Adhoc Communication and Networks (Secon)*, Oct. 2004.

[10] "AS 3930 Low frequency IC," `http://www.austriamicrosystems.com`.

[11] H Ishihara et al. "A 130μA wake-up receiver SoC in 0.13μm CMOS for reducing standby power of an electric appliance controlled by an infrared remote controller," in *IEEE Int. Solid-State Circuits Conf. Dig.*, pp. 226-228, Feb. 2011.

[12] N.M. Pletcher, S. Gambini, and J. Rabaey, "A 52μW wake-up receiver with -72dBm sensitivity using an uncertain-IF architecture," in *IEEE Int. Solid-State Circuits Conf. Dig.*, pp. 524-633, Feb. 2008.

[13] X. Huang, S. Rampu, X. Wang, G. Dolmans, and H. de Groot, "A 2.4GHz/915MHz 51μW wake-up receiver with offset and noise suppression," in *IEEE Int. Solid-State Circuits Conf. Dig.*, pp. 222-223, Feb. 2010.

[14] D. Goldberg, A. Andreou, P. Julian, P. Pouliquen, L. Riddle, and R. Rosasco, "A wake-up detector for an acoustic surveillance sensor network: algorithm and vlsi implementation," in *Intl. Sym. on Information Processing in Sensor Networks*, 2004.

[15] P-tag datasheet, `http://www.sonitor.com/downloads/files/SonitorP-Tag`.

[16] C. R. Hill, J. C. Bamber, and G. R. ter Haar, *Physical Principles of Medical Ultrasonics.* Wiley, 2002.

[17] S. Bower, K. Schuchter, and S. Campbell, "Doppler ultrasound screening as part of routine antenatal scanning: prediction of pre-eclampsia and intrauterine growth retardation," BJOG: An International Journal of Obstetrics and Gynaecology, vol. 100, no. 11, pp. 989-994, 1993.

[18] S. Sheen, H. Chien, and A. Raptis, "Ultrasonic techniques for detecting helium leaks," Sensors & Actuators: B. Chemical, vol. 71, no. 3, pp. 197-202, 2000.

[19] K. Wong, "Instrumentation and health monitoring of cable-supported bridges," Structural Control and Health Monitoring, vol. 11, no. 2, pp. 91-124, 2004.

[20] M. Stojanovic,"Recent advances in high-speed underwater acoustic communications," IEEE Journal of Oceanic Engineering, vol. 21, no. 2, pp. 125-136, 1996.

[21] C. Lopes and P. Aguiar, "Acoustic Modems for Ubiquitous Computing," IEEE Pervasive Computing, pp. 62-71, 2003.

[22] V. Gerasimov and W. Bender, "Things that talk: Using sound for device-to-device and device-to-human communication," IBM Systems Journal, vol. 39, no. 3, pp. 530-546, 2000.

[23] `http://sonicnotify.com/`.

[24] G. Saulnier, H. Scarton, A. Gavens, D. Shoudy, T. Murphy, M. Wetzel, S. Bard, S. Roa-Prada, and P. Das, "P1G-4 Through-Wall Communication of Low-Rate Digital Data Using Ultrasound," in Ultrasonics Symposium, 2006. IEEE, 2006, pp. 1385-1389.

[25] C. Kuratli and Q. Huang, "A fully integrated self-calibrating transmitter/receive IC for an ultrasound presence detector microsystem," *IEEE Journal of Solid-State Circuits*, vol. 33, no. 6, pp. 832-841, 1998.

[26] N. Priyantha, A. Chakraborty, H. Balakrishnan, "The cricket location-support system," *in Proc. ACM MobiCom00*, pp. 32-43, Aug. 2000.

[27] A. Savvides, C.-C. Han, and M. Srivastava, "Dynamic Fine-Grained Localization in Ad-Hoc Networks of Sensors," *in Proc. 7th ACM MobiCom*, pp. 166-79, July 2001.

[28] G. Oberholzer, P. Sommer, and R. Wattenhofer, "Demo Abstract : The SpiderBat Ultrasound Positioning System," *in Proc. of ACM Conf. on Embedded Networked Sensor Systems (SenSys)*, pp. 403-404, 2010.

[29] K. Yadav, I. Kymissis and P. Kinget, "A 4.4μW wake-up receiver using ultrasound data communication," in *VLSI Circuits Symp. Dig.*, pp. 212-213, June 15-17, 2011.

[30] A. Harter, A. Hopper, P. Steggles, A. Ward, and E. Wesbster, "The Anatomy of a Context-Aware Application," *In Proc. ACM/IEEE MOBICOM*, Aug. 1999.

[31] G. Borriello, A. Liu, T. Offer, C. Palistrant, and R. Sharp, "Walrus: wireless acoustic location with room-level resolution using ultrasound," *in Proc. of international conference on Mobile systems, applications, and services (Mobisys)*, pp. 191-203, 2005.

[32] A. Madhavapeddy, D. Scott, and R. Sharp , "Context-Aware Computing with Sound," *in Proc. Intl. Conference on Ubiquitous Computing*, Oct. 2003.

[33] V. Gerasimov and W. Bender, "Things that talk: Using sound for device-to-device and device-to-human communication," *IBM Systems Journal*, vol. 39, no. 3,4, pp. 530-546, 2000.

[34] M. O. Khan, A. Syed, W. Ye, J. Heidemann, and J. Wills, "Demo abstract: Bringing sensor networks underwater with low-power acoustic communications," *in Proc. of ACM Conf. on Embedded Networked Sensor Systems (SenSys)*, Nov. 2008.

[35] U.S. Food and Drug Administration, "Information for manufacturers seeking marketing clearance of diagnostic ultrasonic systems and transducers," `http://www.fda.gov`, issued on Sep. 9, 2008.

[36] HC-SR04 `www.micropik.com/PDF/HCSR04.pdf`.

[37] ARducopter https://store.diydrones.com/category_s/28.htm.

[38] M. Gorlatova, P. Kinget, I. Kymissis, D. Rubenstein, X. Wang, and G. Zussman, "Energy-Harvesting Active Networked Tags (EnHANTs) for Ubiquitous Object Networking," in *IEEE Wireless Communications*, vol. 17, no. 6, pp. 18-25, Dec. 2010.

[39] Occupation Safety and Health Administration, U.S. Department of Labor, "Occupational Safety and Health Standards 1910.95," http://www.osha.gov.

[40] American Conference of Governmental Industrial Hygienists, "Threshold Limit values for chemical substances and physical agents and biological exposure indices," http://www.acgih.org, 2002.

[41] 40kHz Transmit (40KT25) SensComp, Livonia, MI.

[42] 40kHz Receive (US40KR) and 40kHz Receive (US40KT) PVDF transducer, Measurement Specialities, Hampton, VA.

[43] Models and parameters of piezoelectric transducers in *The applications of Ferroelectric Polymers* edited by T.T. Wang, J. M. Herbert and A. M. Glass, Chapman and Hall, 1988.

[44] Z. Chang and W. M. C. Sansen, "Low-noise, low-distortion CMOS AM wide-band amplifiers matching a capacitive source," in *IEEE J. Solid-State Circuits*, vol. 25, no. 3, pp. 833-840, Jun. 1990.

[45] Microphone, Preamplifier (377C01,426B03). PCB Piezotronics, Depew, NY.

[46] Nathan Pletcher, *Ultra-Low Power Wake-Up Receivers for Wireless Sensor Networks*, Ph.D. dissertation, Dept. Elect. Eng, Univ. of California, Berkeley, CA, May 2008.

[47] Y. Zhang, L. Huang, G. Dolmans, and H. Groot, "An analytical model for Energy Efficiency Analysis of Different Wakeup Radio Schemes," *in Proc. of International Symposium on Personal, Indoor and Mobile Radio Communication.*, Sept. 2009.

[48] S. Holm, "Airborne ultrasound data communications: The core of an indoor positioning system," *in Proc. IEEE International Ultrasonics Symposium*, vol. 3, pp. 1801-1804, Sep. 2005.

[49] I. Kuon and J. Rose, "Measuring the gap between FPGAs and ASICs," *in Proc. ACM/SIGDA 10th Int. Symp. Field-Programmable Gate Arrays*, pp. 21-30, 2006.

[50] K. Whitehouse, C. Karlof, A. Woo, F. Jiang and D. Culler, "The Effects of Ranging Noise on Multihop Localization: An Empirical Study," *in Proc. of International Symposium on Information Processing in Sensor Networks (IPSN)*, April 2005.

[51] H. E. Bass and L. N. Bolen, "Ultrasonic background noise in industrial environments," *Journ. Acoust. Soc. Am.*, vol. 78, No. 6, pp. 2013-2016, Dec. 1985.

[52] L.L. Navarro-Serment, C. Paredis, and P. Khosla, "A beacon system for the localization of distributed robotic teams," *in Proc. International Conference on Field and Service Robots*, pp. 232237, 1999.

[53] T2 tags `http://www.aeroscout.com/t2-tag-family`.

[54] Tag `http://www.tempsys.net/fetch_overview.htm`.

[55] M. Toda, "Cylindrical PVDF film transmitters and receivers for air ultrasound," in *IEEE Trans. Ultrason. Ferroelectr. Freq. Control*, vol. 49, no. 5, pp. 626-634, 2002.

[56] PSI-5H4E, Lead Zirconate Titanate, Piezo Systems Inc., Woburn, MA. `http://www.piezo.com/prodmaterialprop.html`

[57] C. Li, D. Hutchins, and R. Green, "Short-range ultrasonic digital communications in air," in *IEEE Trans. on Ultrasonics, Ferroelectrics and Frequency Control*, vol. 55, no. 4, pp. 908-918, Apr. 2008.